HAW HAMBURG

Master thesis

Jan Philip Dittmann

Development of a finite element simulation methodology for the analysis of thick-walled hydrogen tanks

Fakultät Technik und Informatik
Department Fahrzeugtechnik und Flugzeugbau

Faculty of Engineering and Computer Science
Department of Automotive and Aeronautical Engineering

Jan Philip Dittmann

Development of a finite element simulation methodology for the analysis of thick-walled hydrogen tanks

Master thesis submitted for examination in Master´s degree

in the study course Master of Science Flugzeugbau
at the Department of Automotive and Aeronautical Engineering
at the Faculty of Engineering and Computer Science
at University of Applied Science Hamburg

in cooperation with:
German Aerospace Center
Institute of Structures and Design
Pfaffenwaldring 38-40
70569 Stuttgart

First supervisor: Prof. Dr. Markus Linke
Second supervisor: Mathieu Vinot

Submitted on: January 22nd 2025

Zusammenfassung

Jan Philip Dittmann

Thema der Masterthesis

Entwicklung einer Finite-Element Simulationsmethodik für die Berechnung von dickwandigen Wasserstofftanks

Stichworte

FE Simulation, Wasserstofftanks, LS-DYNA, Parameterstudie

Kurzzusammenfassung

Das Ziel dieser Thesis ist die Entwicklung einer Methodik für die Simulation von dickwandigen Wasserstofftanks. Die entwickelte Methodik soll die Faserarchitektur sowie das interlaminare Verhalten der Struktur bei inneren und äußeren Lasten abbilden können. Für die Auswahl einer Methodik werden Voruntersuchungen an einem simplifizierten Tankmodell sowie eine finale Untersuchung an einem realen Tankmodell unter verschiedenen Lastfällen durchgeführt. Aus den Untersuchungsergebnissen haben sich die Parameter für eine Simulationsmethodik ergeben. Die Methodik bildet die Faserarchitektur im Detail ab und ist im Rechenaufwand anpassbar. Die Anwendung der Methodik hat gezeigt, dass sinnvolle Ergebnisse erzielt werden.

Jan Philip Dittmann

Title of Thesis

Development of a finite element simulation methodology for the analysis of thick-walled hydrogen tanks

Keywords

FE Simulation, Hydrogen tanks, LS-DYNA, Parameter study

Abstract

The aim of this thesis is to develop a methodology for the simulation of thick-walled hydrogen tanks. The developed methodology should be able to simulate the fibre architecture as well as the inter-laminar behaviour of the structure under internal and external loads. For the selection of a methodology, preliminary investigations are carried out on a simplified tank model and a final investigation on a real tank model under various load cases. The parameters for a simulation methodology were derived from the test results. The methodology models the fibre architecture in detail and can be adapted in terms of computational effort. The application of the methodology has shown that meaningful results can be achieved.

Task

The objective of this work is the further development of a tool for the generation of models of tank structures, with a particular focus on the representation of internal pressure loads. The tool is then used to conduct numerical investigations regarding the level of detail, simulation accuracy and calculation effort with the finite element solver LS-DYNA. The objective is to create a precise numerical representation of the tank structure, its fibre architecture and the internal and external loads, with a view to developing a computationally efficient method for simulating an entire vehicle. Subsequently, simulations are conducted on the entire tank under different load types to assess the capabilities of the selected methodology.

The work is comprised of the following subtasks: The estimated time scale for each individual stage serves as a guideline for the scope of the work steps.

1. Review of the literature on the modelling of thick-walled hydrogen storage structures, with a particular focus on the internal pressure load (3 weeks)
2. Incorporation and further development of a tool for automated model generation of the tank structure (3 weeks)
3. Selection of a modelling method for simulations at the overall tank level (4 weeks)
4. Investigation and evaluation of the various methods for modelling the internal pressure load (10 weeks)
5. Conducting structural simulations under different types of load (4 weeks)

Acknowledgement

I would like to thank my DLR supervisor, Mathieu Vinot, whose expertise and support were instrumental in the completion of this thesis. His foresight in setting the task and planning the scope of the project enabled me to create a thesis of a high standard in terms of content in the given time, without nightly overtime or daily boredom in the office. His prompt support with questions and problems made it possible to stick to my work schedule, even when difficulties arose. The realisation of the thesis in this way would not have been possible without his support.

Contents

List of Figures

List of Tables

Abbreviations

2D	two dimensional.
3D	three dimensional.
Al	Aluminium.
ALE	Arbitrary-Lagrangian-Eulerian.
ASME	American Society of Mechanical Engineers.
CAD	Computer aided design.
CFD	Computational fluid dynamics.
CFRP	Carbon fibre reinforced plastic.
cl	Combined layers.
config	Configuration.
CPM	Corpuscular particle model.
CPU	Central processing unit.
CV	Control volume.
dof	Degrees of freedom.
el	Element.
elform	element formulation.
EU	European Union.
EV	Electric vehicle.
FE	Finite element.
FEM	Finite element method.
GFRP	Glass fibre reinforced plastic.
HDD	Hard disk drive.
ILM	Inter-layer model.
nel	Number of elements.
nip	Number of integration points.

RAM	Random access memory.
RE	Richardson Extrapolation.
rel	relative.
SPC	Single point constraint.
SSD	Solid state drive.
tshell	Thickshell.
UN	United Nations.
UP	Uniform pressure.

Symbols

C	Circumferential length of the tank.
E_{damp}	Energy dissipated by damping.
E_{hg}	Non-physical energy due to hourglassing of elements.
E_{int}	Elastic strain energy and work done in permanent deformation at the current time step of the simulation.
E^0_{int}	Elastic strain energy and work done in permanent deformation at the start of the simulation.
E_{kin}	Total kinetic energy of the system at the current time step of the simulation.
E^0_{kin}	Total kinetic energy of the system at the start of the simulation.
E_{rw}	Change in kinetic energy of slave nodes (elastic) as a result of interaction with the rigid wall (rigid).
E_{si}	Sum of master and slave contact energy and friction energy.
E_{total}	Sum of the energies.
W_{ext}	Work done by boundary conditions such as loads, displacements, velocities and accelerations.
a	Node acceleration.
d	Node displacement.
h	Average element edge length of all elements.
n	Index of time step.
r	Ratio of two average element edge lengths.
v	Node velocity.
x	Element edge length in axial and tangential direction.
x_rel	Element edge length relative to the circumference of the tank in axial and tangential direction.
α	Fibre angle.
ϵ	Difference of two simulation results with with different mesh densities.
ϕ	Arbitrary result of a simulation with a defined mesh density.

1 Introduction

At the UN Climate Change Conference in Paris in 2015, 197 countries decided to keep global warming below two degrees Celsius by 2100. The implementation of this decision was further specified by the EU in 2021. The goal is to become the first carbon-neutral continent by 2050. [1] Enormous efforts must be made to achieve this goal. The focus here is particularly on transportation, which accounts for a significant share of carbon emissions at over 10 % [2]. The last few years have shown that mobility, especially private transport, can also function without the direct emission of polluting gases with the help of electric drives. Two forms of energy supply have become established: Batteries, which store electrical energy directly, and fuel cells, which generate electrical energy from hydrogen and oxygen. When fuel cells are used, hydrogen is utilised as an indirect energy store. This hydrogen must be provided in the respective vehicle. This is usually done by storing it in tanks. According to the current state of the art, hydrogen tanks are therefore a relevant component for achieving climate targets.

While cars with electric drives (EVs) have a major advantage in terms of climate protection, more cars with combustion engines are still being sold [3]. The reluctance of buyers is mainly due to the limited range of EVs in combination with a limited refuelling and charging infrastructure. One way to accelerate the spread of EVs would therefore be to increase their range. This can be decisively influenced by three parameters: Hydrogen storage quantity, aerodynamic resistance and total mass of the means of transport. The tank has a direct influence on the storage quantity and the total mass. The aim is therefore a tank that contains as much hydrogen as possible and is not too heavy at the same time. In addition to these performance parameters, a tank must also meet other requirements. These include the size of the tank, which must correspond to the specified installation space, but also safety-related specifications, such as the crash and impact behaviour of the tank. Analytical and numerical calculation methods as well as experimental investigations are used to optimise the performance parameters while simultaneously complying with all requirements. Finite element (FE) simulations have become the most important method in recent years. They are not as limited in terms of geometries and materials as analytical methods and are also significantly more cost-effective than experimental tests. Simulations have proven to be the most suitable tool for designing hydrogen tanks and are therefore crucial for the development of electric cars with fuel cells.

The aim of this thesis is the precise numerical representation of the tank structure, its fibre architecture and the internal and external loads with regard to a computationally efficient application in a simulation of the entire vehicle. For this purpose, different combinations of modelling and simulation methods are compared and evaluated based on self-selected criteria in relation to the stated objective.

This thesis is based on the following information and data, which were obtained in advance. In a previous project, a tank geometry and a stacking sequence for a tank optimised for burst pressure were determined. At the end of the thesis, the modelling method obtained will be applied to this tank. The material data used is also available and does not need to be determined. The same applies to basic simulation parameters such as time step size, details of the result output or detailed settings of the solver. A Python tool is provided for generating the mesh of the models. This tool is written specifically for the creation of the mesh to match the tank geometry provided and is being further developed in this thesis.

2 State of the Art

2.1 Hydrogen Tanks

Hydrogen tanks can be divided into two categories. High-pressure tanks store the hydrogen in a gaseous state at high pressures. Cryogenic tanks store the hydrogen in a liquid state. In this state, the hydrogen can be stored at significantly lower pressures (usually up to 5 bar), but the hydrogen must be cooled to below -250°C so that it does not reach boiling point. High-pressure tanks are mostly used in ground transportation (cars, trains, etc.), where the mass of the tanks is less relevant and cooling the hydrogen is not worthwhile. The opposite is true for air transportation. In this case, the significantly lighter cryogenic tanks are usually used. Only high-pressure tanks are considered in this thesis, as only these require thick walls, which are examined. [4, 5]

High-pressure hydrogen tanks can be classified into five types. Figure 2.1 shows these types in detail and Table 2.1 lists further information for each type.

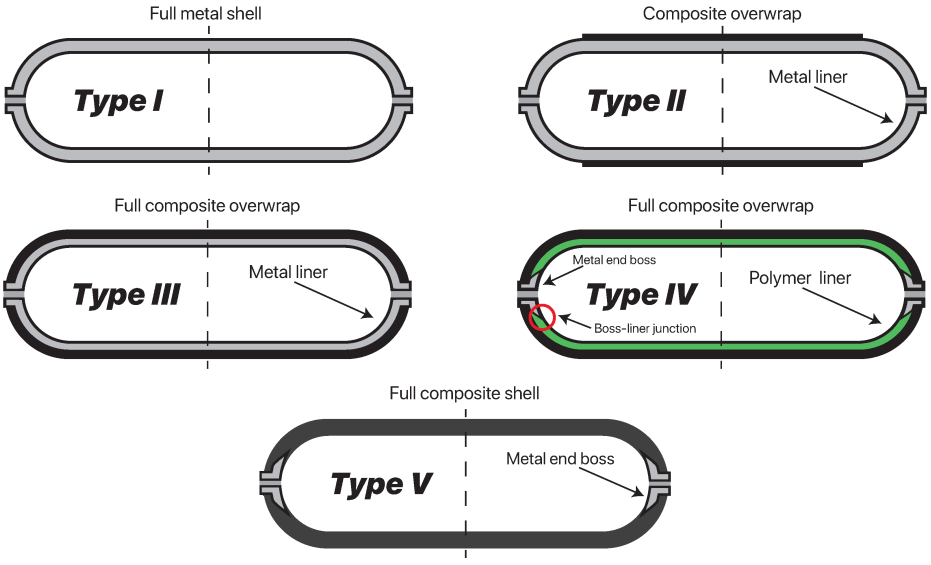

Figure 2.1: Classification of high pressure hydrogen tanks [4]

Table 2.1: Hydrogen tanks classification and main features (adapted from [4])

Type	Metal	Composite	Poly-mer	Max. Pressure (bar)	Applications	Structural Load
I	Steel/Al	-	-	Al: 175, Steel: 200	Submarine Applications	Metal body
II	Steel/Al liner	Filament windings around the cylinder part	-	Al/Glass: 263, Steel/Carbon fibre: 299	Stationary fuel cells and hydrogen technologies	Steel and composite (load is equally shared)
III	Al/Steel liner	Composite over-wrap (GFRP or CFRP)	-	Al/Glass: 305, Al/Aramid: 438, Al/Carbon: 700	Vehicles	Composite (95 %) and metal liner (5 %)
IV	-	Composite over-wrap (CFRP)	Polymer liner	350 (buses), 700	Vehicles	Composite
V	-	Composite	-	1000	Aerospace Applications	Composite

The existing tank design (geometry and layer structure) refers to a type IV tank, which is why all investigations in this thesis are carried out on this type of tank. The load-bearing structure of this tank type consists of several layers of CFRP and is designed for an internal pressure of up to 700 bar (70 MPa). The resin of the CFRP structure is not able to prevent the highly volatile hydrogen gas from leaking. For this reason, a polymer layer known as a liner is required in addition to the load-bearing structure to prevent the gas from permeating through the tank. [4]

The use of fibre composite material means that the structural properties of the tank can be precisely adapted to the load case. The fibre angles of the individual layers can be selected so that the majority fibres point in the main load direction. However, the limitations of the manufacturing process must be considered. In most cases, a fibre winding process is used for production, which is very efficient as it enables fast and cheap production and is easy to automate. However, fibre angles of 0° and 90° are not possible with standard methods. Slightly larger or smaller angles have to be used instead. It is also common to wind fibre layers in pairs. This means that each +α layer is followed by a -α layer, or vice versa. [6]

2.2 Finite Element Method

In the following sections, important details on FE simulations are presented for the understanding of this thesis. LS-DYNA is used as FE software. The information provided on FE simulations relates to the use of LS-DYNA and may differ in comparison to other programmes. LS-DYNA uses so-called keyword cards for the model generation. These cards consist of a keyword that defines what this card describes (e.g. *NODE) and the associated parameter values. For example, the parameter values node id and the x, y and z coordinates are defined in the node card.

2.2.1 Solver

Two main types of solvers are used for FEM simulations: explicit and implicit. These are terms for different time integration algorithms, which are used by the solver. The main difference is in the formulation of the equations for calculating the value of a quantity. By using an explicit formulation, the values at time step $n+1$ can be calculated directly, because the equation only uses values from time step n or previous. Equation 2.1 shows how an explicit formulation for the calculation of the value d could look like. What the individual variables d, v and a stand for is not relevant in this case.

$$d^{n+1} = f\left(d^n, v^n, a^n, d^{n-1}, \ldots\right) \tag{2.1}$$

For the implicit formulation values of time step n and $n+1$ are used to calculate the values at $n+1$.

$$d^{n+1} = f\left(v^{n+1}, a^{n+1}, d^n, v^n, \ldots\right) \tag{2.2}$$

Therefore, a direct calculation is not possible since the values of time step $n+1$ are not known. To solve these implicit equations a system of linear equations needs to be solved. [7]

The different formulations of the equations and the different methods of solving them give rise to several advantages and disadvantages which make the methods suitable for different types of problems. The explicit solvers capability to solve the equations for each time step directly results in very quick calculations of each time step. But on the other hand, it is only conditional stable, which means that the time step size is limited by element size and Courant condition. This makes explicit solvers well suited for highly dynamic or highly non-linear problems with a short duration time (<100 ms) such as impact or crash simulations. Implicit solvers invest a lot of computational effort into solving the systems of linear equations for each time step, but therefore are unconditionally stable, which means that they can use much larger time step sizes. This makes implicit solvers well suited for static, quasi-static or structural dynamic problems. Especially problems with longer duration times are no problem since the time step size can be adjusted accordingly. [8, 9, 10]

Both methods are to some degree capable to solve problems for which they are not so well suited. Explicit solvers can solve static problems, but the long duration of static problems make them less efficient than an implicit simulation. Implicit solvers can solve non-linear problems by linearisation in each time step, but the more non-linear the problem is, the smaller the time step size must be.

This results in many calculation expensive steps, which negates the greatest advantage of the implicit method. [8, 9, 10]

In addition to the possibility that the problem itself is non-linear, e.g. due to large deformations in a crash simulation, simple linear problems can also become non-linear. This is the case if non-linear materials are used, or the model contains contacts that often use non-linear relationships. In these cases, the calculation effort of implicit solvers massively increases, and the use of an explicit solver may be more appropriate.

To summarize, explicit solvers use many simple time steps and are therefore well suited for dynamic and non-linear problems. Implicit solvers use few complex time steps and are therefore well suited for static problems and problems over long periods of time. More details about the solvers and the underlying theory (especially for the implicit solver) can be found in the LS-DYNA Theory Manual [11]

2.2.2 Element Type

In LS-DYNA, two parts are required to define an element. On the one hand, the element type which describes the geometry of the element, e.g. an 8-node solid element (3D), or a 3-node shell element (2D) and an element formulation (elform). The elform describes how the element is calculated. In the case of solid elements, for example, elform 1 stands for a calculation with a single-point integration (reduced integration), while elform 2 describes a fully integrated element. [11]

Solid

Three types of elements are relevant for the simulation of tanks in this thesis: Solid elements (solids), shell elements (shells) and thick shell elements (tshells). Solids and shells are standard elements, which are part of every common FE software. The most common forms of solids are 8- or 16-noded hexahedrons or 4- or 10-noded tetrahedrons (see Figure 2.2) [8, 12]. Each node of the element has three degrees of freedom (dof), one displacement in each direction.

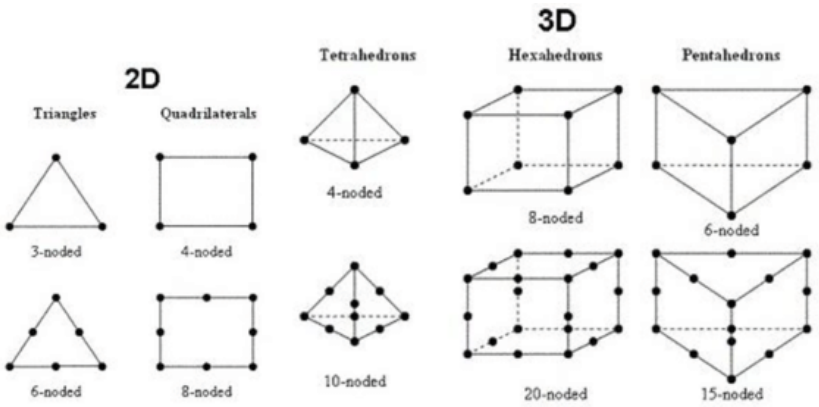

Figure 2.2: Common 2D and 3D element types [13]

LS-DYNA uses a reduced integration for their standard solid element (elform 1) to calculate the volume integral of the element. This formulation has only one integration point in the middle of the element (constant stress element) instead of a full 8-point integration (see Figure 2.3). This reduces the calculation time of the integration by more than factor 25 [11]. In return, disadvantages such as reduced accuracy and hourglassing have to be accepted (see section 2.2.5).

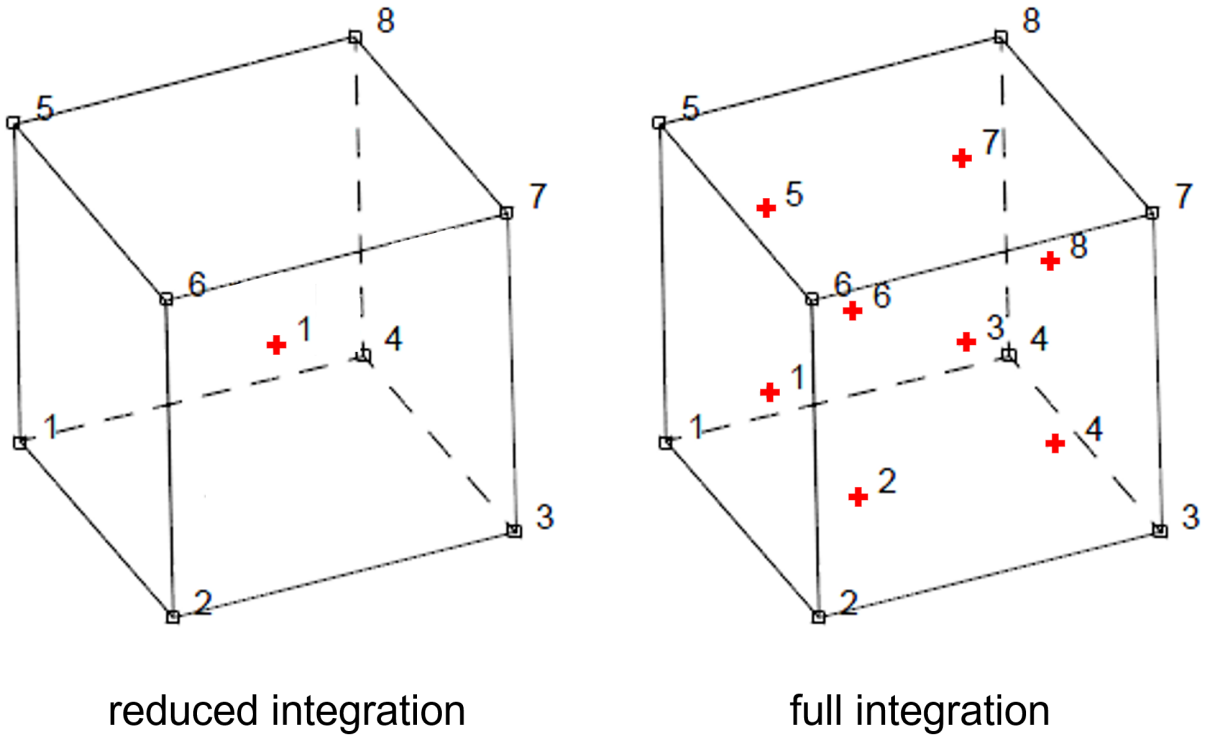

Figure 2.3: Integration points for reduced and full integration of a 8-noded hexahedral element (adapted from [14])

Shell

The most common forms of shells are 4- or 8-noded quadrilaterals or 3- or 6-noded triangulars (see Fig 2.2) [8, 12]. As with the solid elements, LS-DYNA offers a large selection of different element formulations for the shell elements. In this work, elform 16 is used for the shell elements. In this element formulation, selective reduced integration is used. This means that full integration (4 in-plane integration points as in Figure 2.4) is used for all calculations, except for the transverse shear. For the transverse shear, a single-point integration is used to prevent transverse shear locking. A reduced integration as with the solid element is not necessary, since models with shell elements require less computing time than comparable models with solid elements. [15]

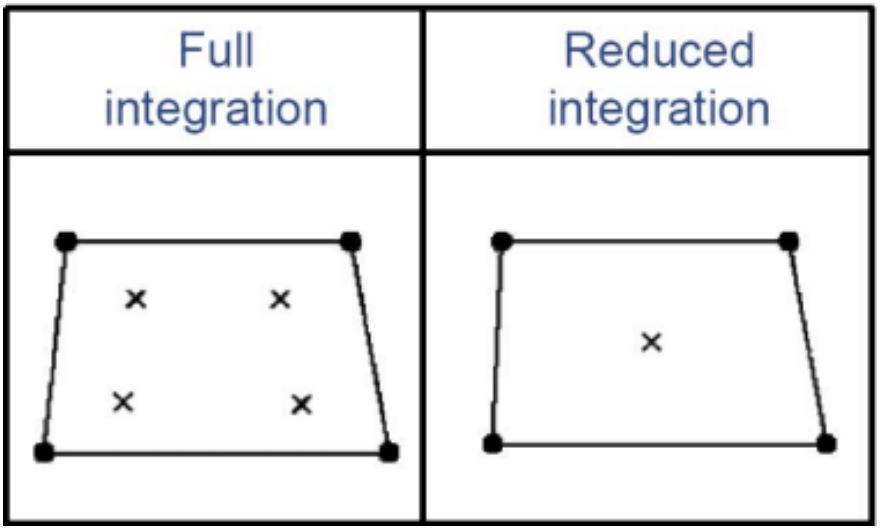

Figure 2.4: Integration points for reduced and full integration of a 4-noded quadrilateral element (adapted from [16])

The in-plane integration points are used to determine the displacements and stresses in the plane of the element. In order to determine additional values over the virtual thickness (z-axis) of the element, integration points are stacked in this direction [12]. Each stacked integration points creates a new plane in which stresses can be determined (Figure 2.5).

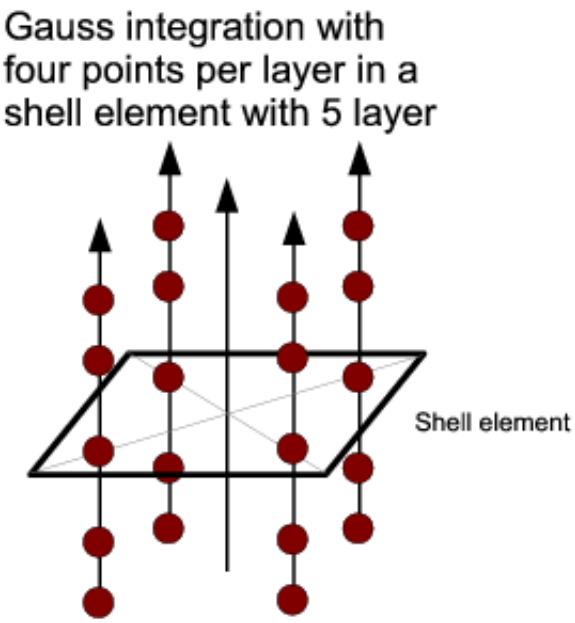

Figure 2.5: Vertical stacking of integration points (adapted from [17])

The number of layers of integration points is defined by the user. LS-DYNA allows each layer of integration points to be assigned its own material [8]. This makes it possible to model several different layers of a composite material in one element. In addition to the advantages mentioned, stacking integration points also has its limits. As the displacements are node values and not element values, only four node displacements can be output for four-node shell elements. The stresses are also limited. The stress perpendicular to the element plane (z-direction) cannot be determined and is always zero [12].

Thickshell

The third element type, the thickshell (tshell) elements, are less common than the other two types. Tshell elements form a hybrid or intermediate form of solid and shell elements. The geometry corresponds to a solid element with eight or 16 nodes (tetrahedrons are not possible) [8]. At the same time, the element formulation allows a stacking of integration points as with shell elements [11]. These two properties provide a decisive advantage in the simulation of thick-walled composite structures. In contrast to shell elements, it is possible to stack elements without contact conditions via common nodes. Therefore, structures which are too thick for one shell element can be simulated more accurately. At the same time, several layers of a composite can be modelled in one element via the stacked integration points. This allows to create a model with less elements in thickness direction than composite layers, which is especially useful for structures with lots of layers. Due to the arrangement of the integration points, a tshell element has a defined alignment like a shell element. The area between nodes one to four is the bottom, the area between nodes five to eight is the top and the other areas are on the side (Figure 2.6). This orientation must be considered when creating the model.

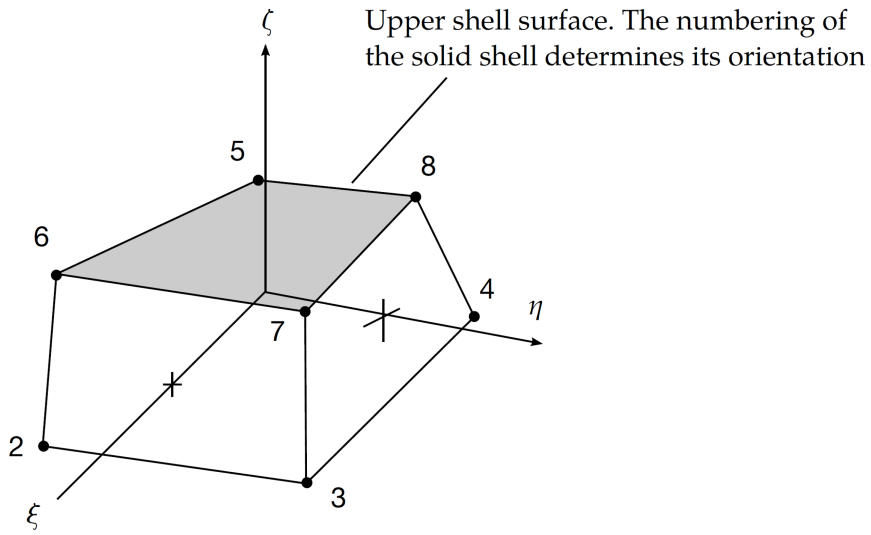

Figure 2.6: Orientation of tshell elements [11]

In this thesis elform 5 is used for tshell elements. This element formulation stands for reduced integration. In this case, this means an integration point is located in the middle of the element, as with the solid element and the integration points are positioned above and below this point in the thickness direction (similar to Figure 2.5). [11, 18] The 8-noded element makes it possible to calculate the stress in the vertical direction (z-direction) as with a solid element. Due to the reduced integration, the stress is constant across the element. The additional integration points cannot be used to determine multiple values of the z-stress along the vertical axis of the element.

2.2.3 Simulation of Gases

As software that is specifically used for crash simulations, LS-DYNA offers simple CFD solvers as well as finite element methods that have been explicitly developed for simulating airbags [19, 20, 21]. These are designed to simulate all relevant aspects of the gas in the airbag, the airbag itself and surrounding objects with which the airbag interacts in one simulation. Due to the similarity between an inflated airbag and a pressurised hydrogen tank, these methods can be used to model the internal pressure of a tank. LS-DYNA offers three basic calculation or modelling methods that are relevant for this thesis. These methods are the Control Volume Method (CV), the Arbitrary-Lagrangian-Eulerian Method (ALE) and the Corpuscular Particle Method (CPM) [8, 21]. All methods are explained in more detail in the following sections. Advantages and disadvantages are listed for each method. These are just a selection of all the advantages and disadvantages that are relevant for the application in this thesis. Further advantages and disadvantages may be relevant for other applications.

Control Volume Method

The control volume (CV) method, also referred to as the uniform pressure method (UP), is one of the oldest methods for simulating airbags. In this method, the gas is calculated as a finite volume without discretisation. Each thermodynamic variable, such as pressure or temperature, is assigned a scalar value that applies to the entire volume. The values of the variables are determined from the boundary conditions and basic thermodynamic equations. The equations used are listed and explained in the theory manual [11]. Due to the equations with scalar variables, the calculation time can be neglected in comparison to the calculation of the surrounding structure. The biggest weakness of the method is the inability to simulate local effects. As the properties always apply to the entire volume, no local values can be calculated. Additional models enable the modelling of certain local effects such as a pressure field caused by inflowing gas, but the possibilities are limited. Another disadvantage is the gas law used in this method. The CV method uses the ideal gas law. This simplified gas law is only a good approximation for hydrogen at low pressures (see Figure 2.7). A more accurate description of the gas behaviour with a real gas law is not possible with the CV method. [11, 21, 22]

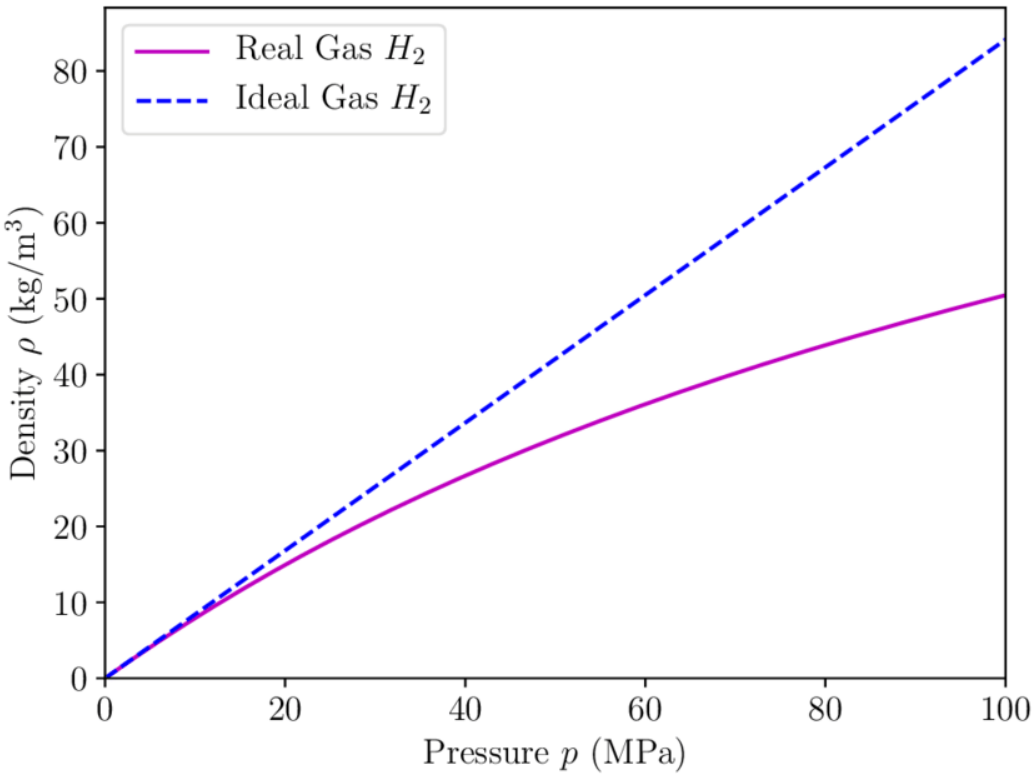

Figure 2.7: Comparison of results of the ideal gas equation and real gas equation for hydrogen gas [23]

Arbitrary-Lagrangian-Eulerian Method

With the Arbitrary-Lagrangian-Eulerian (ALE) method, as with CFD methods, the gas volume is discretised with elements (Figure 2.9) and the conservation equations are applied to the elements. As the volume within the airbag changes significantly during deployment, the mesh for calculating the gas must also follow this movement. The element distortion must be minimised during the simulation, otherwise the calculation quality of the elements will decrease. The solution to this problem is the ALE method. It combines the stationary formulation of Lagrange's equations with the moving formulation of Euler. This makes it possible to smooth the mesh between the simulation steps (see Figure 2.8). Detailed information on the implementation of the equations is provided in the theory manual [11].

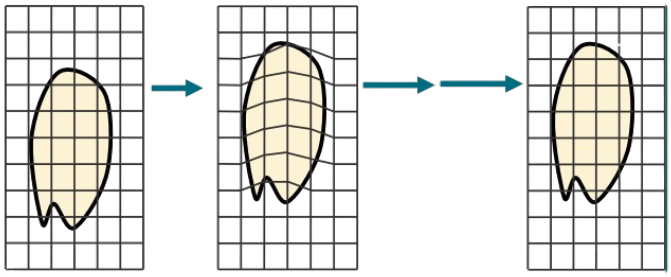

Figure 2.8: Mesh smoothing of ALE method [22]

The discretisation of the volume is both the biggest advantage, and the biggest disadvantage compared to the CV method. The ALE method allows different thermodynamic parameters for each element and can thus realistically map the gas behaviour. In addition, the mesh refinement can be used to control whether fast calculation times or more precise results are to be achieved. On the other hand, significantly more calculation points are used compared to the CV method, which results in a considerably longer calculation time. These long calculation times and the complex model creation (discretisation) mean that the ALE method is only used when other methods are not possible. [11, 21, 22]

Corpuscular Particle Method

The limitations of the CV method and the high computational effort of the ALE method have led to the development of new methods for the calculation of gases in closed volumes. The Corpuscular Particle Method (CPM) has been implemented in LS-DYNA for this purpose. It is intended to replace the ALE method. The CPM does not use the continuum approach of the CV method, nor the discretisation approach of the ALE and some other methods. Instead, the method is based on the kinetic molecular theory. This means that the molecules themselves are modelled and simulated. Since a volume of an airbag contains 10^{23} to 10^{24} molecules, a direct simulation of all molecules is not possible. For this reason, groups of molecules are combined into so-called particles (Figure 2.9). These particles have the same properties as molecules (e.g. mass, speed, spin, vibration, etc.).

Through the interaction of the particles with each other and with the environment, effects such as pressure on surrounding walls or temperature changes in the volume can be calculated. [21, 22]

The CPM offers several advantages. It adopts the more accurate representation of the gas behaviour of the ALE method and combines it with the simple mesh-free modelling of the gas volume of the CV method. In addition, the simulation is simple and robust due to the use of the equations of kinetic molecular theory. Similar to the ALE method, the computational effort and the precision of the results can be controlled with the CPM. The more particles are used in the simulation, the more precisely the behaviour of the gas is simulated. In this case, the control is even simpler, as only one number in the parameter card needs to be changed and no new mesh needs to be created. It is also possible to assign polynomial functions to gas model parameters like the heat capacity in the CPM to simulate real gases such as hydrogen. In addition to the many advantages, a few disadvantages must be considered. The calculation time is significantly longer compared to the CV method and the small number of particles compared to the number of molecules can lead to noise in the pressure values. The number of particles required depends on the size of the volume and the complexity of the gas behaviour. Therefore, the number of particles needed must be determined based on comparisons with experimental results or a parameter study. [21, 22]

Figure 2.9 shows a model for each method. On the left is the volume of the CV method in white, in the centre is the mesh of the ALE method (green) and on the right are the particles of the CPM (black).

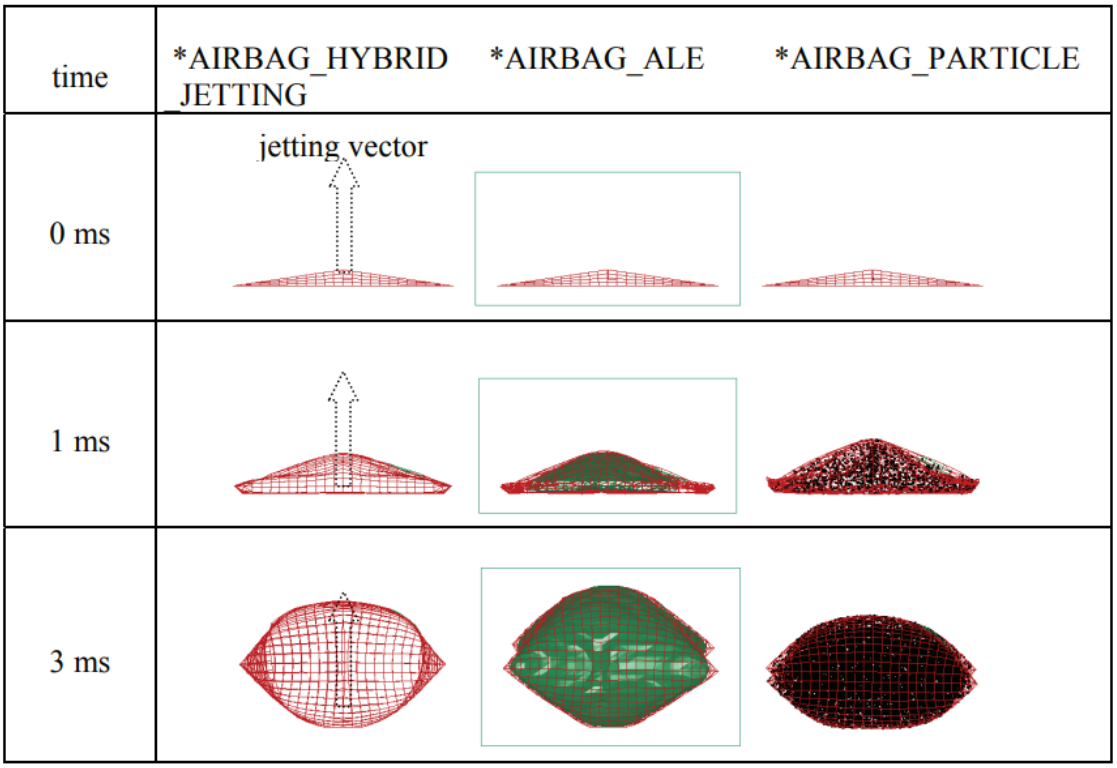

Figure 2.9: Comparison of CV, ALE and CPM using a simple airbag [21]

2.2.4 Inter-Layer Models

In the context of this work, inter-layer models are mathematical models for describing the material behaviour between the individual layers of a composite. Only fibre-reinforced plastics are used in this thesis. Therefore, the properties, advantages and disadvantages of the models are only related to the modelling of the resin between the fibre layers. LS-DYNA provides two common options for inter-layer models (ILM). The elements representing the fibre layers can be connected to each other via a contact (cohesive contacts), or via an additional element inserted between the main elements (cohesive elements).

Cohesive Contact

Tiebreak contacts are suitable for cohesive contacts. With tiebreak contacts, the contact partners (master and slave) are connected to each other until a failure criterion is exceeded (Figure 2.10). Once the criterion has been exceeded, the fixed connection is broken and, depending on the definition, replaced by a contact with or without friction [24]. This contact can only transmit compressive and if applicable frictional forces. Tiebreak contacts are based on the penalty method. A normal interface spring is placed between the nodes at the contact surface of the slave and the contact surface of the master and vis versa. The stiffness of this spring causes a force on nodes, which penetrate or separate from the contact surface. This force pushes or pulls the nodes back towards the contact surface. The deeper the penetration or separation, the stronger the force on the node. [11]

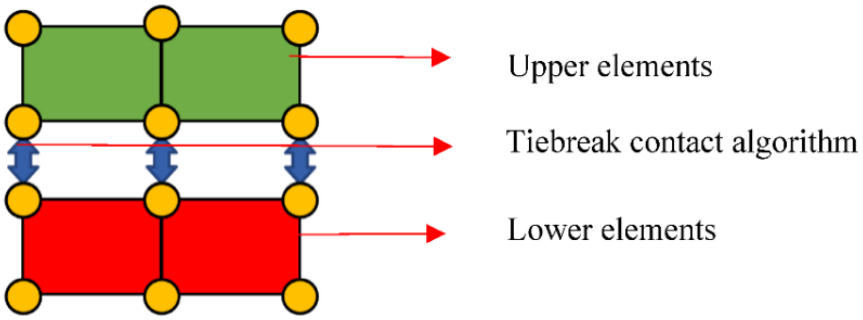

Figure 2.10: Node connection with tiebreak contact [25]

Cohesive Element

Cohesive elements are special elements that are inserted into the mesh to model a bond between two elements of different fibre layers (Figure 2.11). The shape of the elements does not differ from solid or tshell elements. The special properties are defined by the element formulation and the material definition. The mathematical model underlying cohesive elements combines the displacement of the top and bottom of the element with non-linear springs. Thus, in theory, the element is only two-dimensional. This mathematical two-dimensionality means that cohesive elements can be very small in the z-direction without the simulation becoming unstable. [26]

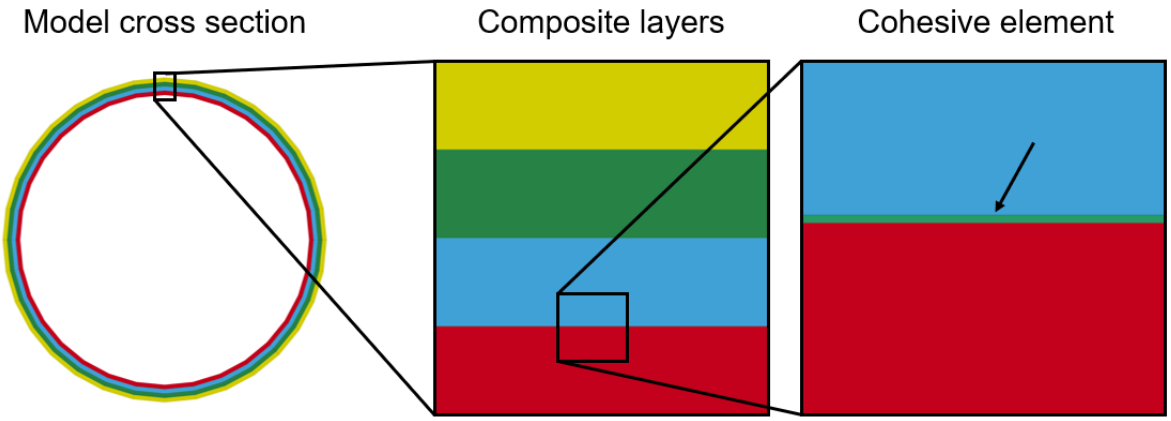

Figure 2.11: Application of cohesive elements

LS-DYNA offers a selection of different cohesive elements that differ in shape (pentahedron or hexahedron), suitability for adjacent element types (solid, shell or tshell) or failure models (bilinear or trilinear) [11]. In this work, only element formulation 19 and material models 138 and 240 are used. The failure model of material 138 is equivalent to the tiebreak contact. Both use a bilinear failure model (Fig. 2.12). In comparison, material 240 is more complex and uses a trilinear failure model (Fig. 2.13). This has the advantage that the real material behaviour can be modelled better. However, more material parameters must be known [27] or experimentally determined and the calculation effort for elements with this material is higher. Experiences in previous investigations have shown, that in some cases the trilinear material model can lead to a more stable calculation of the simulation.
Further details on the mathematical models of the cohesive elements can be found in the theory manual in chapter 5 [11].

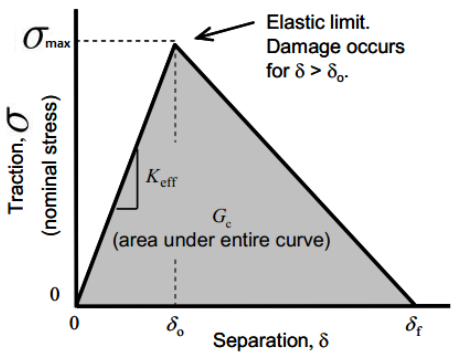

Figure 2.12: Bilinear failure model [28]

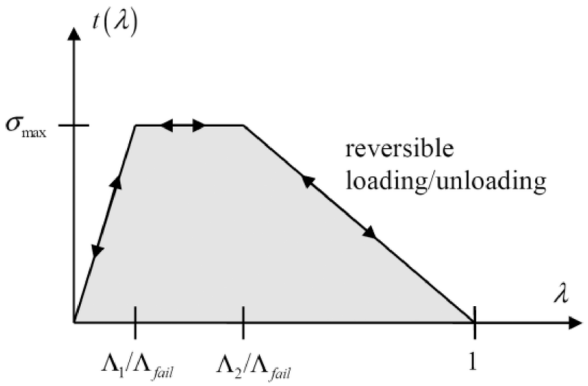

Figure 2.13: Trilinear failure model [29]

2.2.5 Energies

The energies calculated in a simulation can be used in two ways. On the one hand, they can be used directly if, for example, a deformation energy is sought in the event of an impact. On the other hand, energies can be used to evaluate the quality of a simulation. In LS-DYNA, the energies listed in Table 2.2 can be output after the simulation. It is possible to output the energies for the entire model or separately for each material.

Table 2.2: Description of energy symbols [11, 30, 31, 32, 33, 34, 35]

Symbol	Name	Description
E_{total}	Total energy	Sum of the energies
E_{kin}^{0}	Initial kinetic energy	Total kinetic energy of the system at the start of the simulation
E_{kin}	Current kinetic energy	Total kinetic energy of the system at the current time step of the simulation
E_{int}^{0}	Initial internal energy	Elastic strain energy and work done in permanent deformation at the start of the simulation
E_{int}	Current internal energy	Elastic strain energy and work done in permanent deformation at the current time step of the simulation
W_{ext}	External work	Work done by boundary conditions such as loads, displacements, velocities and accelerations
E_{si}	Sliding interface energy	Sum of master and slave contact energy and friction energy
E_{rw}	Rigid wall energy	Change in kinetic energy of slave nodes (elastic) as a result of interaction with the rigid wall (rigid)
E_{damp}	Damping energy	Energy dissipated by damping
E_{hg}	Hourglass energy	Non-physical energy due to hourglassing of elements (see below)

The sliding interface (CFRP) energy results from the energies of all contacts. It describes the sum of the contact energies of master and slave nodes, surfaces or parts. As energy is transferred from the master to the slave or vice versa in a contact, one side of the contact has a positive contact energy, while the other side has a negative contact energy. If the sum of both energies is formed, they cancel each other out and the sliding interface energy is zero. If a coefficient of friction is defined between the contact partners when defining the contact, a portion of the energy can, depending on the use case, dissipate via friction when the energy is transferred. The dissipated energy is included in the sliding interface energy with positive values. Therefore, a positive sliding interface energy is to be expected. A negative sliding interface energy indicates an improper simulation. A common reason for this are initial penetrations of the contact surfaces. [32]

Hourglass energy is an energy that arises through the effect of Hourglassing. Hourglassing is a nonphysical, zero-energy deformation that produce zero strain and no stress. The effect only occurs with the single-point integration of under-integrated solid, shell and tshell elements. Figure 2.14 shows how such a deformation could look like.

The hourglass energy describes the work which is done by the internal forces applied to resist hourglass modes. The hourglass energy is dissipative. This energy must not be too large, as it does not describe any physical processes and is purely numerical. As a guideline, the hourglass energy should not be more than 10 % of the internal energy. [35]

Three options are available to reduce or avoid hourglassing. The simplest option is to avoid under-integrated elements, as these are the only elements where hourglassing can occur. It should be kept in mind that higher-value elements are usually significantly more computationally intensive. If hourglassing cannot be ruled out, mesh refinement offers the possibility of reducing the effect, as smaller elements are less susceptible. In addition to these two options, LS-DYNA offers hourglass control algorithms. These introduce viscous damping or small elastic stiffness into the elements to counteract the deformation. Further details on these algorithms can be found in the theory manual. [11]

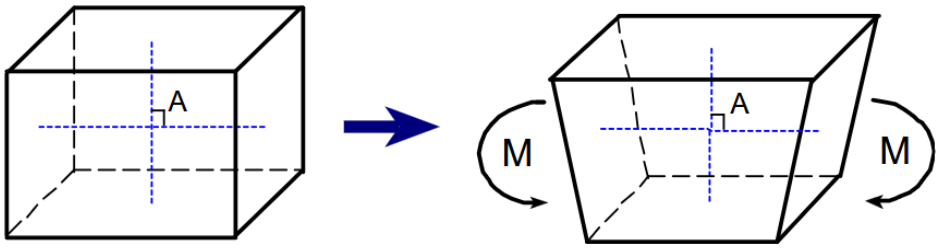

Figure 2.14: Hourglassing deformation [36]

The energies in Table 2.2 can be used to check simulation results in a first step without the need for a reference solution. For this purpose, the curves of individual energies can be compared with an expected result, or the ratios between energies can be compared with reference values. An example of this is the ratio between hourglass energy and internal energy. A third way to check the results is the balance of external work, internal energy and dissipated energy [30]. Equations 2.3 and 2.4 show how this energy balance would look like.

$$E_{total} = E^0_{kin} + E^0_{int} + W_{ext} \tag{2.3}$$

$$E_{total} = E_{kin} + E_{int} + E_{si} + E_{rw} + E_{damp} + E_{hg} \tag{2.4}$$

If this balance is met, this indicates a good quality simulation. However, if the total energy is greater than the initial and external energy, energy is artificially added to the system and if it is less, energy is artificially removed from the system. The reasons for an artificial injection of energy can be, among others, numerical instability or sudden penetrations through contact surfaces. Possible reasons for artificial energy absorption can be heavy hourglassing, or issues with rigid walls or overdetermined contact surfaces.

2.3 Richardson Extrapolation

The Richardson extrapolation (RE) is a numerical method that can be used to approximate the limit value of a sequence. This means that the accuracy of a calculated numerical solution can be increased using this method. In the context of discretization problems such as FEM or CFD, the RE can be used to estimate the discretization error. With the discretization error known the result of a value such as the stress or displacement can be extrapolated for an infinitely fine discretization. For the calculation of the discretization error values of multiple different discretizations must be known. In other words, from the result values of a discretization with a mesh size of h_1, h_2 and h_3, a result value for a mesh size of $h_0 = 0$ can be determined. Here, h is a parameter for the mesh size (e.g. average element edge length). [37, 38]

An adapted version of the RE is used in this thesis. It is mainly used in CFD and is part of the American Society of Mechanical Engineers (ASME) guidelines for the calculation of discretization errors [38]. Th application of this method for an FEM problem should be possible, as only the mesh size and the simulation results for these mesh sizes are relevant for this version. For the adapted method, results must be calculated for three differently finely discretized meshes (ϕ_1, ϕ_2, ϕ_3). It is recommended that the ratio of the mean element edge lengths of the different meshes $r_{21} = \frac{h_2}{h_1}$ and $r_{32} = \frac{h_3}{h_2}$ are not less than 1.3. To extrapolate the calculation results for an infinitely fine mesh ($h_0 = 0$), the order of the method has to be calculated using equation 2.5 and 2.6. Here, ϵ_{32} stands for the difference of the results $\phi_3 - \phi_2$ and ϵ_{32} for the difference $\phi_3 - \phi_2$.

$$p = \frac{ln(\frac{\epsilon_{32}}{\epsilon_{21}})}{ln(r_{21})} + q(p) \tag{2.5}$$

$$q(p) = ln\left(\frac{r_{21}^p - s}{r_{32}^p - s}\right) \tag{2.6}$$

If the mesh has been refined twice by the same value, e.g. the element edge length has been halved twice, the equations can be simplified further. In this case, $r_{21} = r_{32} = r$, resulting in $q(p) = ln(1) = 0$. Equation 2.5 can therefore be reduced to equation 2.7.

$$p = \frac{ln(\frac{\epsilon_{32}}{\epsilon_{21}})}{ln(r)} \tag{2.7}$$

The value of the result for an infinitely fine mesh can then be determined using equation 2.8.

$$\phi_{h=0} = \phi_1 + \frac{-\epsilon_{21}}{(r)^p - 1} \tag{2.8}$$

An example of the application of RE is the determination of the stress in an element. If the stresses from three simulations with different element sizes are known, equations 2.7 and 2.8 can be used to determine the stress for an infinitely fine mesh. Conversely, this value can then be used to determine the discretization error for the three initial values.

2.4 Literature Regarding Simulation of Hydrogen Tanks

This section provides a brief overview of the literature on the subject of analysing thick-walled hydrogen tanks. Most literature sources analyse the tanks with regard to burst pressure. The aim is usually to optimise the tank structure (layer structure or material), the manufacturing process or the modelling. The burst pressure is used as the optimisation target or constraint, where the burst pressure is to remain the same and the mass is to be reduced. [39, 40, 41]

Compared to this first group, significantly fewer sources are available on impact load cases for thick-walled hydrogen tanks. The research has revealed a doctoral thesis by Weerts [42], an article by Fang [25] and an article by Blanc-Vannet [43]. This small number of literature sources on this topic is confirmed by Weerts, who states that he has not found any sources on this topic. Of these three sources, Weerts' doctoral thesis is the most comprehensive. The aim of his work is to develop an FE model with which the damage to a high-pressure hydrogen tank can be simulated and statements can be made about the resilience of the tank after impact damage. His research is based on increasingly complex models and comparisons with experimental tests he has carried out himself. The results of his investigations and tests as well as material data and simulation settings are only available to a limited extent. As the work was part of an industrial project, no absolute values are given for the test results, only normalised values. For the FE model, tshell elements are used for the fibre composite layers and cohesive elements as ILM. The work does not include an investigation of different element types, inter-layer models or number of integration points.

Fang's article is based on Weerts' method. He uses the same FE model but replaces the cohesive elements with cohesive contacts. The aim of his work is to investigate the delamination of models with different stacking sequences after an impact load. As with Weerts, this article does not compare different modelling methods such as element types or similar.

In the third source (Blanc-Vannet), the effect of impact load cases on the failure cause in composite cylinders is investigated. The investigation was carried out experimentally and no simulations were performed. Cylinders from different manufacturers, different internal pressures and different impactors (mass and diameter) were used for the investigations. Compared to Weerts, Fang and this thesis, the impactors are significantly smaller, with diameters ranging from 5 mm to 100 mm. Blanc-Vannet uses a drop tower or a pneumatic launcher for the tests. This generates high-speed impacts, whereas Weerts and Fang carried out investigations in the quasi-static velocity range.

From this brief literature review only a few studies deal with the simulation of impact-loaded thick-walled hydrogen tanks. The studies that do exist select one modelling method and do not compare different methods.

3 Hard- and Software

Two different systems are used for the simulations, depending on the computing performance requirements. The preliminary investigations (basic investigation, burst pressure, gas model and inter-layer model) are simulated locally on the first system. The hardware of this computer is shown in Table 3.1.

Table 3.1: Hardware specifications (local)

Hardware	Specification
Processor (CPU)	Intel Core i7-6700, 4 Cores 8 Threads, 3.40 GHz
Memory (RAM)	8 GB, 2133 MHz
Main storage	SSD 239 GB
Data storage	HDD 932 GB

For the final investigation of the hydrogen tank, the calculation of the simulations is done by a workstation. The specifications of the workstation are shown in Table 3.2. Depending on the utilisation of the workstation by others and the required computing performance, one to four full nodes are used for the simulations.

Table 3.2: Hardware specifications (workstation)

Hardware	Specification
Total nodes	20
Cores per node	32
Processor (CPU)	2x 16 core AMD EPYC „MILAN“ 7313
Memory (RAM)	16x 64 GB DDR4 3200 MHz
Storage	500 GB Crucial P5 Plus SSD

The specifications for the CPU, RAM and storage refer to one node. Investigations relating to the computing time of the configurations examined are only carried out in the basic investigation and therefore only relate to the computing performance of the local system. Sample comparisons of more complex models from the investigation of the inter-layer models have shown that simulations can be calculated around ten times faster on one node of the workstation compared to the local system.

LS-DYNA was used for all FE simulations. Simulations on the local computer were carried out with version 14.1. As this version is not available on the workstation, version 14.0.1 was used for these simulations. No major changes from version 14.0.1 to version 14.1 affect the keywords used in this work [44]. Minor changes, e.g. to contact keywords, are not relevant for this work, as these changes are not expected to have a significant impact on the simulation results.

Python scripts are used for pre- and post-processing. The scripts are written or extended as part of this thesis. A detailed workflow describing the use of all files and scripts is shown in Appendix B. Python version 3.12 is used to execute the scripts. LS-PrePost Version 4.11 is used for the graphical representation of model geometry, mesh and simulation results (except diagrams).

4 Investigations

4.1 Overview

Five investigations are carried out in the following sections. The aim of these investigations is to compare different combinations of modelling and simulation variants and finally to find a combination that is most suitable for the simulation of hydrogen tanks. The five investigations are divided into four preliminary investigations and one final investigation. The preliminary investigations use simplified models to compare the variants regarding selected aspects. The analysed aspects and the used models are shown in Table 4.1. An interim result is presented after each investigation. The results are used to reduce the number of modelling and simulation parameters for the next investigation. This reduces the number of possible variants from one investigation to the next and enables detailed analysis of more complex models. After the preliminary tests, the entire tank is simulated in the final test. The remaining variants of the parameters from the preliminary tests are used for the simulation to find the best possible combination.

Table 4.1: Overview of Investigations

Name	Analysed Aspect	Relevant Simulations Results
Basic Investigation	General behaviour	Displacements, stresses and simulation time
Burst Pressure	Burst pressure	Burst pressure
Gas Simulation	Modeling internal pressure as gas	Stresses and simulation time
Impact Simulation	Impact and inter-laminar behaviour	Reaction force, energies, inter-laminar failure
Tank Simulation	Application of determined modelling method	Reaction force, energies, inter-laminar failure, simulation time

The values of the following parameters are varied for the investigations: Element type, integration points per element, element size, number of element over wall thickness, solver. Several defined values can be used for each parameter. A variant is created by selecting a value for each parameter. In the following, this variant is referred to as a configuration. Each configuration is unique and is assigned a number for identification.

When creating the configurations from the parameter values, all values of a parameter are combined with all values of all other parameters. However not all combinations are possible. One example of this are solid elements, where only one integration point is provided for each element. This means that a combination with values greater than one is not possible. These variants are skipped when creating the configurations. In addition, selected configurations have been omitted from the configurations that use the explicit solver. Due to the significantly longer simulation times compared to implicit configurations, the simulation of all possible variants is not feasible in this case.

4.2 Simulation Model

This section describes the simulation model for the preliminary investigations. This includes geometry, boundary conditions, material data and stacking sequence of the model.

4.2.1 Geometry and Mesh

The cylindrical part of the tank is examined as a simplified model for the preliminary investigations. The complete tank model is only used for the final investigation. Since the influence of the domes at both ends of the tank only affects the outer areas of the cylindrical part, the results of the simplified model can be transferred to the middle area of a tank. Figure 4.1 shows the simplified model of the tank. The image shows the mesh, as it is generated directly and not derived from a CAD geometry. The mesh density of the tank is only an example and may differ from configuration to configuration. The mesh is created so that the x-axis forms the axis of rotation of the cylinder. The y and z axes therefore point in a radial direction.

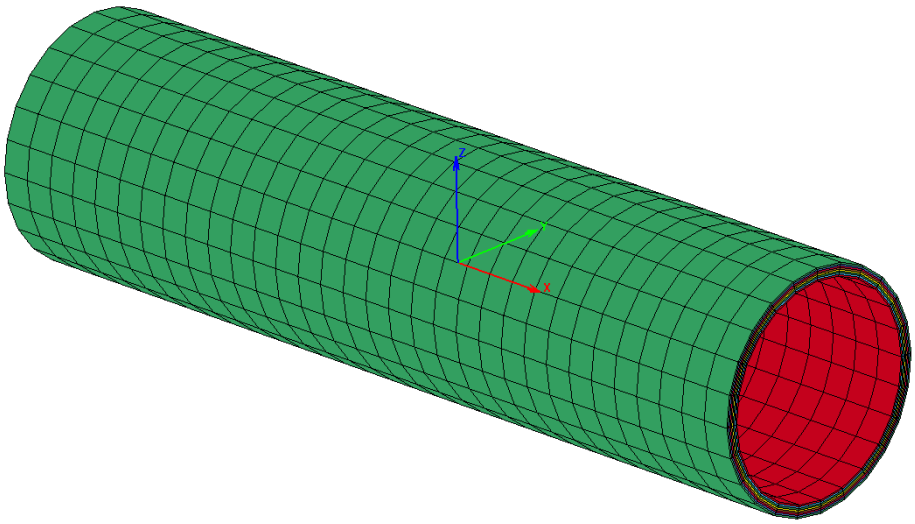

Figure 4.1: Model geometry for solid and tshell elements with example mesh and coordinate system (x: red, y: green, z: blue)

The image of the geometry (Figure 4.1) shows the mesh for a model with volume elements (solid and tshell). Since shell elements are 2D, this results in a surface model for these elements (see Figure 4.2). The shell model is created in such a way that the reference surface is equivalent to the inner surface of the solid model. An offset option is used for the simulation, which defines that all calculation points in the thickness direction of the shell element lie above this surface. This means that the created surface corresponds to the virtual lower surface of the shell element. This type of creation ensures that the volume models (solid and tshell) and the shell models all have the same inner surface. Therefore, the same pressure load can be applied to the surface of all models.

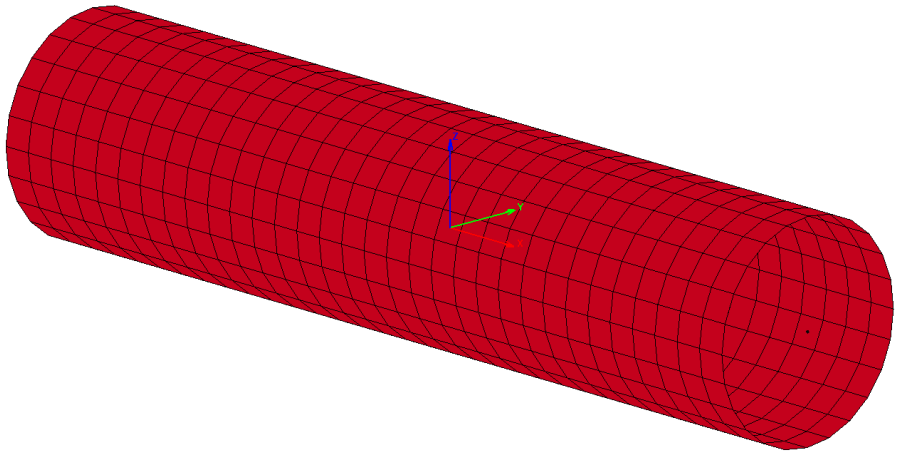

Figure 4.2: Model geometry for solid and tshell elements with example mesh and coordinate system

Table 4.2 shows the geometry parameters of the cylinder.

Table 4.2: Geometry Parameters

Parameter	Value	Unit
Inner radius	165	mm
Outer radius	185	mm
Length	1400	mm

A Python script is used to generate the mesh. This script receives mesh parameters such as element size, number of layers over the wall thickness, element type and number of integration points per element (for shell and tshell) as input from the user. In addition, the script uses information on the geometry (contour in x-direction of the inner surface) and thickness and fibre angle of the composite layers. This information is provided via csv files. From this input information, the script generates a text file from LS-DYNA keywords (keyword file), which contains all information for model creation. This file can be read directly by LS-DYNA. The script is designed to generate rotationally symmetric models. Generating other geometries requires major changes to the script.

4.2.2 Boundary Conditions

Two types of boundary conditions are required for the simulation (constraints and loads). Which loads are used and how large they are, depends on the investigation. Therefore, they are not described in detail here, but in the sections of the investigations. The boundary conditions are used to constrain the rigid body displacement in all three spatial directions. In addition, torsion of the tube around the axis of rotation is prevented. To influence a realistic deformation as little as possible, the boundary conditions are implemented as follows. The axial rigid body displacement is restricted via single point constraints (SPC) at the left end of the tube ($x = -700mm$). All nodes at this end can only be displaced in the y and z directions (Figure 4.3).

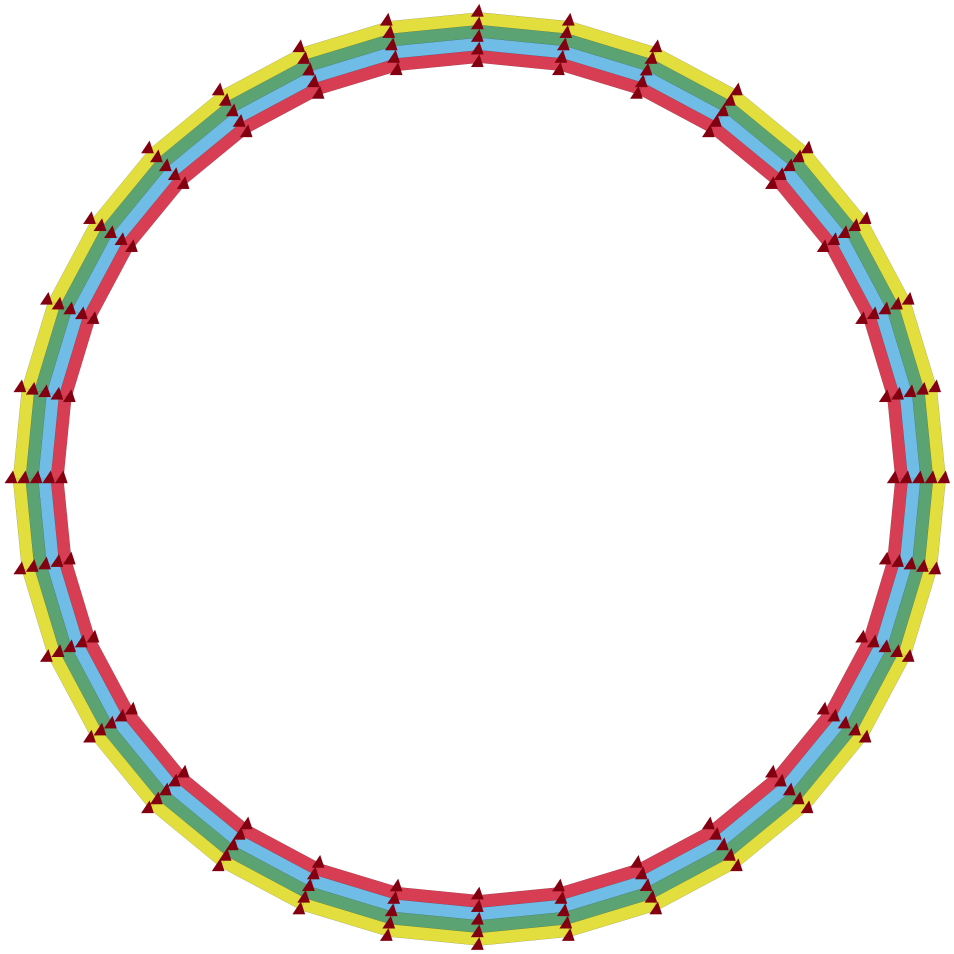

Figure 4.3: Single Point Constraints in x Direction (red markers)

To prevent the rigid body displacement in the y and z directions and the torsion, the nodal displacements at both tube ends are constrained in the tangential direction. Since dedicated cylindrical coordinate systems are not included in LS-DYNA, a direct implementation of tangential constraints is not possible. Instead, the respective displacements are constrained with SPCs at the positions where the tangential direction coincides with the y or z direction (Figure 4.4).

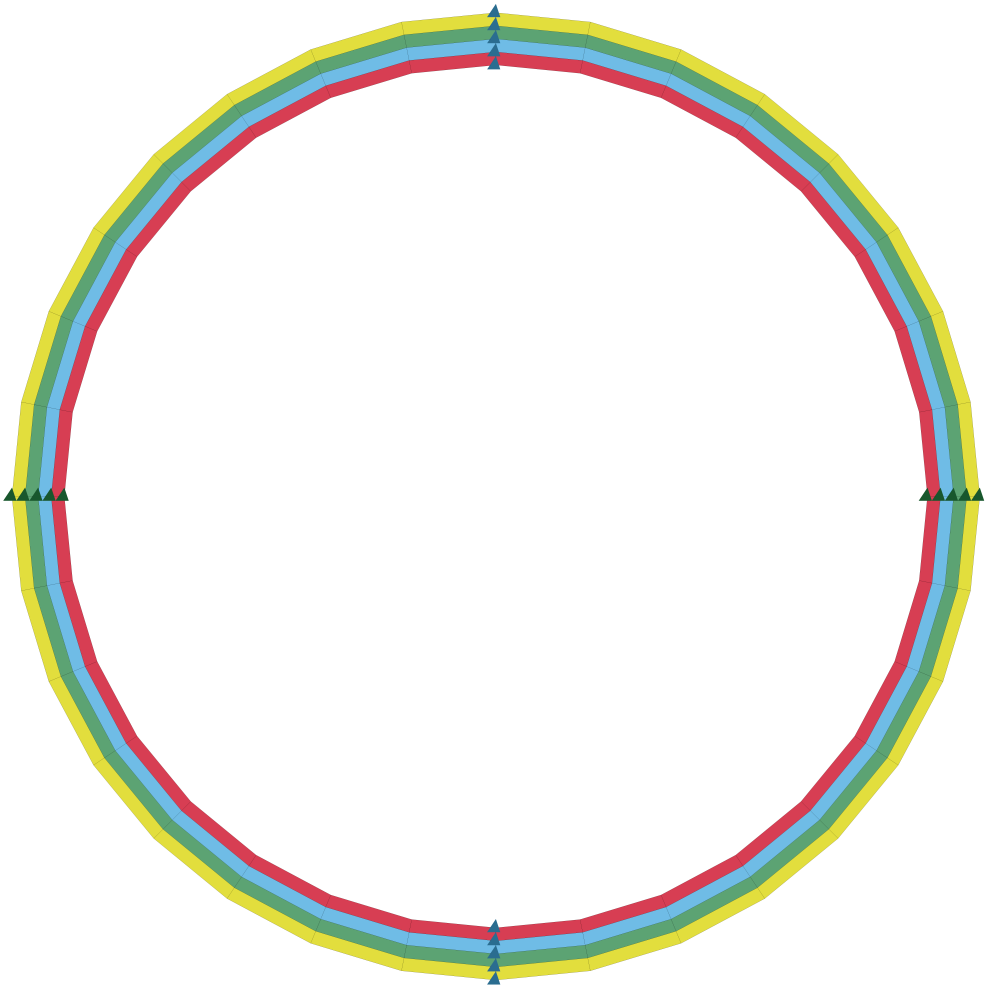

Figure 4.4: Single Point Constraints in y Direction (blue) and z Direction (green)

The figures are representative of all models with solid and tshell elements. For models with shell elements, the constraints are applied at the same locations with the difference that only one node in the radial direction is used.

4.2.3 Material Data and Layup

Carbon fibre reinforced plastic (CFRP) is used as the material for the tank. The material properties are shown in Table 4.3. As the selection of the material is not part of this work, a standard material from a previous project is used [45].

Table 4.3: Material Data

Parameter	Value	Unit
ρ	$1.95 \cdot 10^{-06}$	$\frac{kg}{mm^3}$
E_1	133	GPa
E_2	6.1	GPa
E_3	6.1	GPa
ν_{12}	0.033	1
ν_{13}	0.033	1
ν_{23}	0.2	1
G_{12}	4.1	GPa
G_{13}	4.1	GPa
G_{23}	4.1	GPa

A structure with eight layers is selected for the stacking sequence. This number allows sufficient flexibility to test different modelling of the structure and is also small enough to allow reasonably short simulation times for the investigations. Reasonable values were chosen for the angles of each layer. This was based on common distributions for tanks [45].The following layer structure from the inner to the outer surface has resulted for the tank [+87/-87/+10/-10/+87/-87/+25/-25] (Figure 4.5).

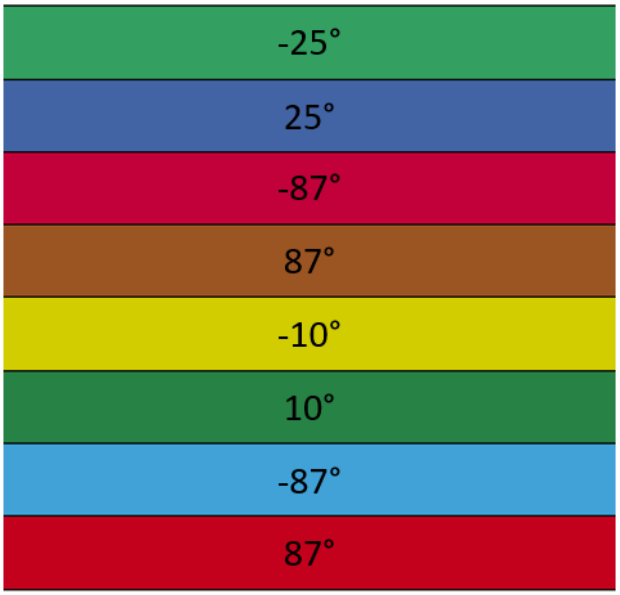

Figure 4.5: Stacking sequence

4.2.4 Simulation Result Location

The following result variables are analysed in the simulations: node displacement, element stress, simulation time, reaction force on impactor, model energies, model deformation and delamination. The nodal displacements and element stresses are evaluated in the centre of the model (see Figure 4.6). In the illustration, the evaluation nodes are marked with yellow markers and the elements to be evaluated are highlighted with thicker frames.

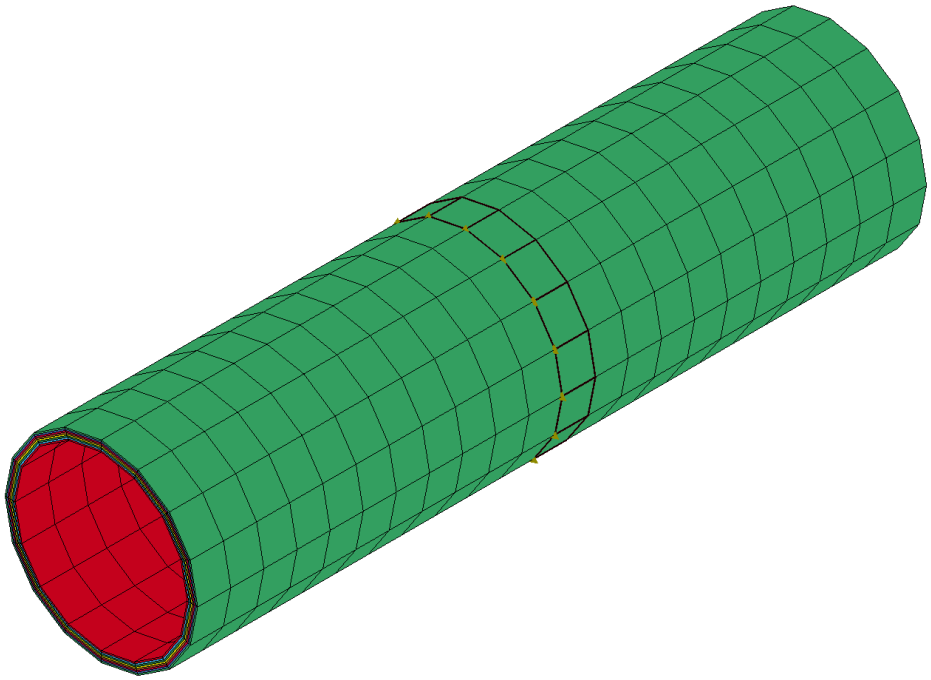

Figure 4.6: Result evaluation locations for nodal displacements and element stresses

The other simulation results are analysed for the entire model. An exception to this is the reaction force, as it only relates to the impactor.

4.3 Basic Investigation

In this study, the general behaviour of a wide range of variants of modelling and simulation parameters is to be investigated. For this reason, a simple geometric model with a simple load case is selected for this investigation. After the investigation, it should be possible to make a statement about the effect of the parameter values on the simulation results. Based on this statement, the number of parameters or parameter values is reduced for the next investigation.

4.3.1 Parameter Values

The values of the individual parameters are shown in the following table.

Table 4.4: Parameter Values of Basic Investigation

Element Type	Integration Points	Element Size (rel)	Number of Elements (thickness)	Solver
solid	1	1.5	1	implicit
shell	2	2.0	2	explicit
tshell	4	2.5	4	
	8	3.0	8	
	16	3.5	16	
	24	4.0	24	
		5.0		
		6.0		

The element size refers to the element edge length. To enable a good comparability with other models, the element size is specified as a relative value in relation to the circumference (C) of the tank. The following equation was used to convert the absolute value of the element size (x) into a relative value (x_{rel}).

$$x_{rel} = \frac{x}{C} \cdot 100 \tag{4.1}$$

Figure 4.7 shows the coarsest and the finest mesh (6.0 and 1.5) as an indication of how large the specified element sizes are.

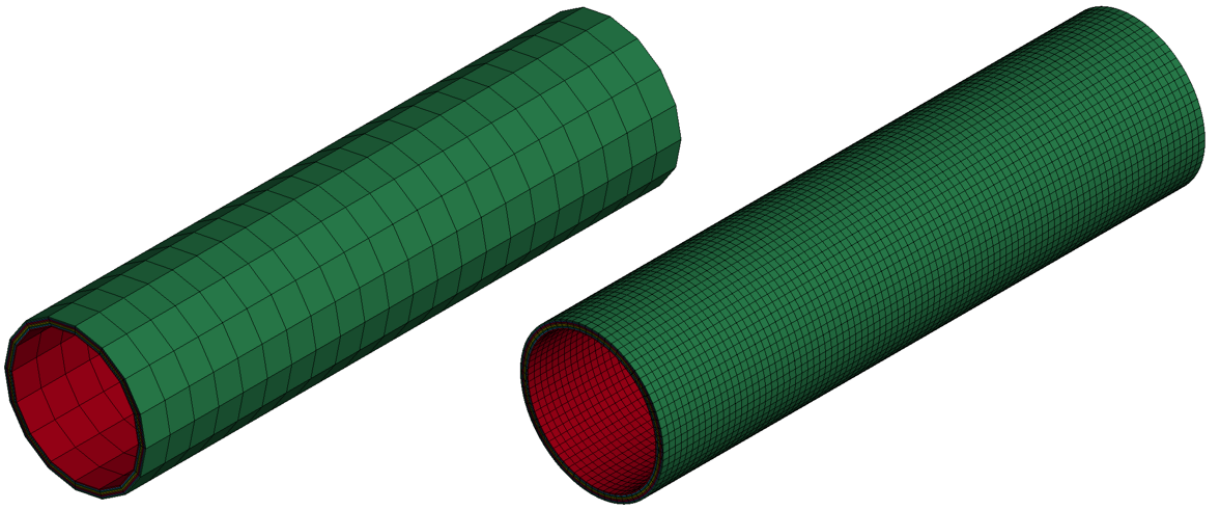

Figure 4.7: Element size comparison of coarse mesh (left) and fine mesh (right)

These values result in 528 possible configurations. Of these, all 264 implicit configurations are simulated. As no major deviations between implicit and explicit configurations are to be expected for this simple model, only a small sample of the explicit variants is simulated. The sample has a size of 36 configurations. This results in a total number of 300 configurations for this investigation. All configurations with the respective parameter values are shown in the table in Appendix A.

4.3.2 Simulation Results

Displacement

This section shows the displacement results from the simulations. As no reference value for the displacements is available, the values are only compared with each other. In the following diagrams, the values of all simulations are shown simultaneously. In this case, identification of individual configurations is not necessary as only a general overview is to be provided.

Figure 4.8 shows the distribution of the axial displacement of the nodes over the wall thickness. The configurations with solid or tshell elements are represented by the lines. The shell elements only have one node in the thickness direction and are therefore only shown as a point. The diagram shows that the values of the configurations with volume elements (solid and tshell) are close to each other (deviation <5 % over the entire curve), while the shell elements lead to significantly higher values. The approximately constant curves correspond to the expectation, as the load is constant across the thickness and the influence of the individual layers is low in this case.

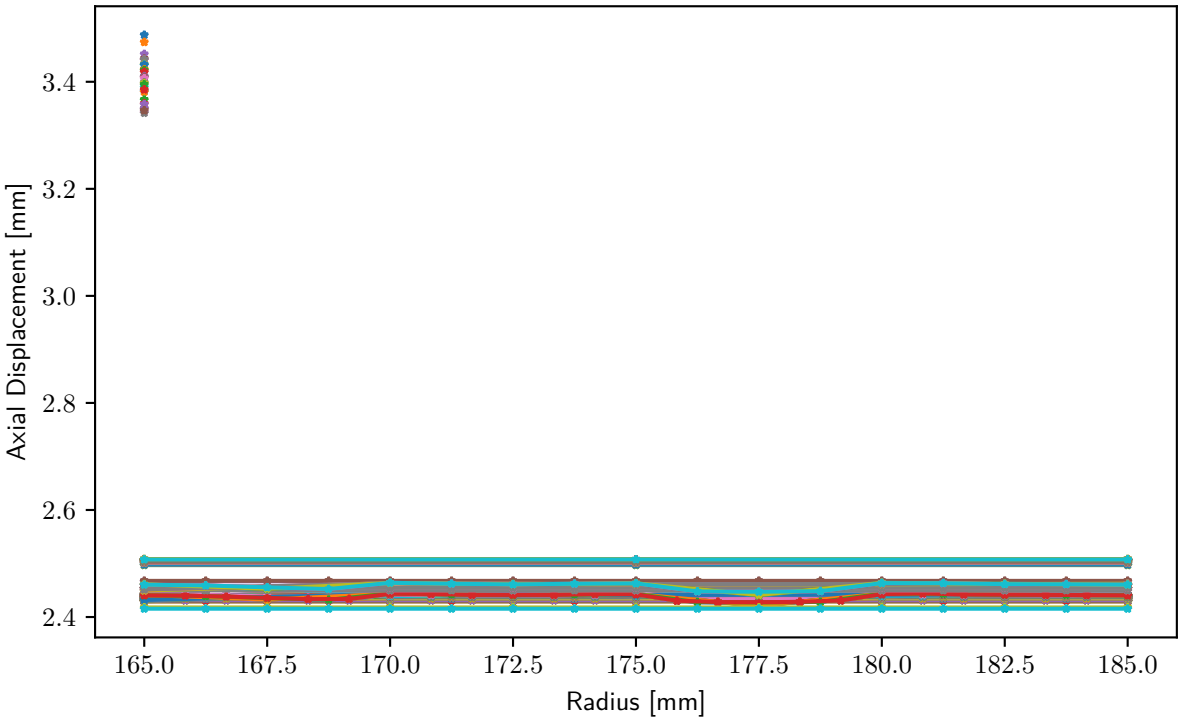

Figure 4.8: Axial displacement over the radius

Figure 4.9 shows the radial distribution of the displacements. As with the axial displacement, the values of the configurations with shell elements (points) deviate greatly from the curves. The majority of the curves are very close to each other, but in contrast to the axial displacement, curves with larger deviations can be seen in this case. The largest deviations are clearly recognizable, but with a deviation of <10 % from the main part of the curves, they are not excessively large. The identification of which parameter values lead to these deviations takes place during the evaluation of the stresses (cf. 4.14).

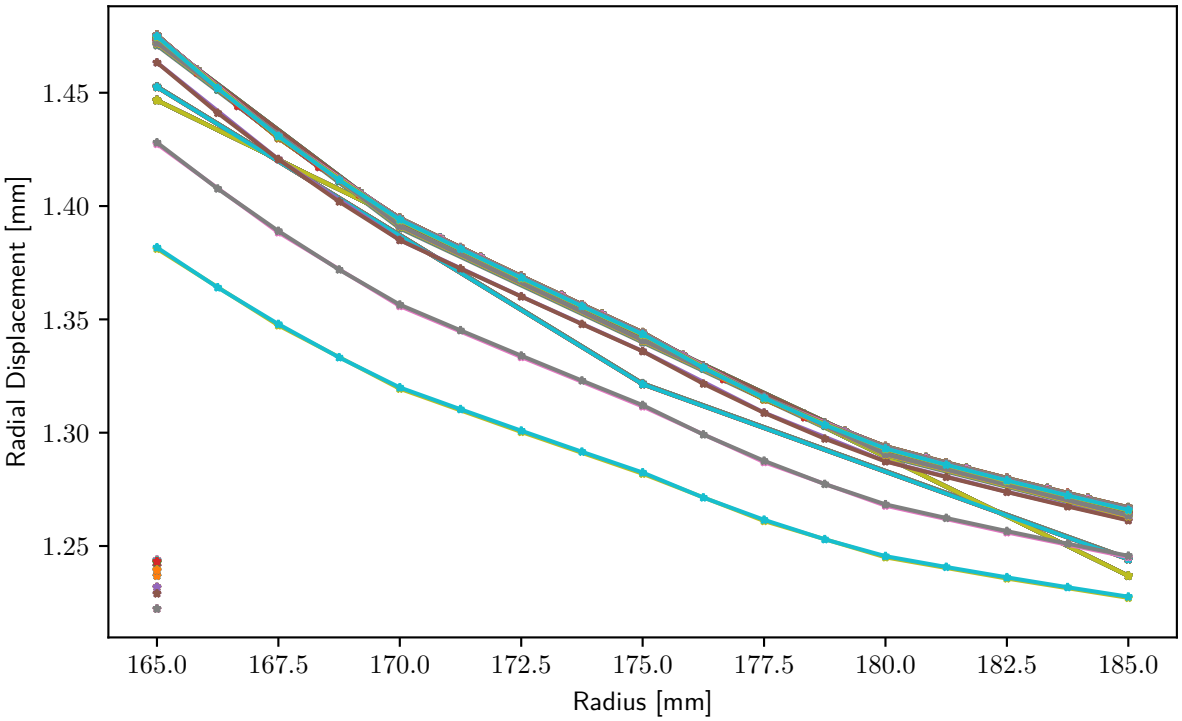

Figure 4.9: Radial displacement over the radius

The third diagram (Figure 4.10) shows the tangential displacement of the nodes. Due to the axisymmetric model and the purely radial load, no displacement in the tangential direction is to be expected. The models with volume elements correspond to this expectation. The values of these configurations are very close to 0mm. The models with shell elements again lead to large deviations. This time it is noticeable that the values are very widely scattered.

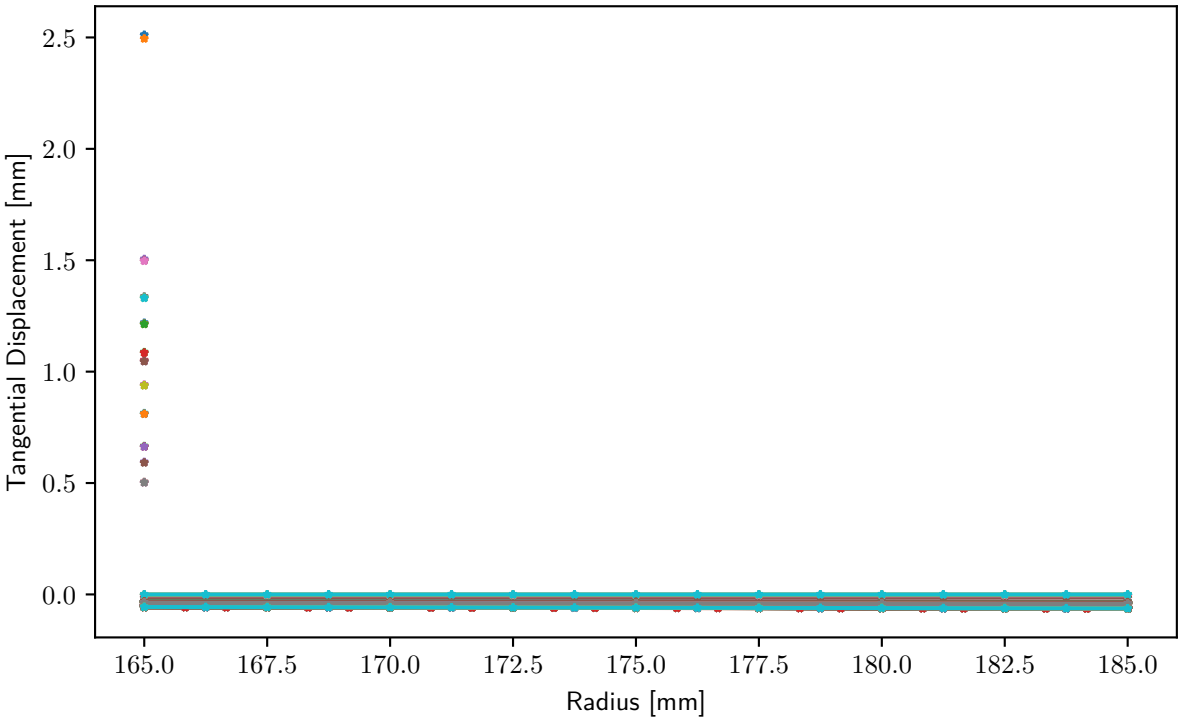

Figure 4.10: Tangential displacement over the radius

The following observations can be derived from all three diagrams. Most of the results are very close to each other, which indicates that the simulations provide correct results. However, no statement can be made as to how well the results match the real part behaviour. The results of the models with shell elements deviate greatly from the rest of the simulation results. These results were to be expected, as shell elements are intended for thin-walled structures and are therefore not suitable for thick-walled tanks, as in this case. Due to the limited number of nodes in the thickness direction, curves such as the radial displacement cannot be displayed and the values for constant curves are also not reliably represented. Further investigation and identification of the deviations (especially in the radial displacement) is carried out in the analysis of the stresses.

Stress

The stress results from the simulations are presented in this section. To verify the model results, the stresses are compared with the values from the tank design software MyCrOChain (Version 0.95.8). In the diagrams, the values of the software are referred to as “reference solution”. As with the displacement diagrams, the diagrams with all simulation results are shown first to provide an overview. Subsequently, individual peculiarities are examined in diagrams with fewer data points. In the following, the $\pm 25°$ and $\pm 10°$ layers are referred to as polar layers and the $\pm 87°$ layers as hoop layers. In the diagrams, the hoop layers are at $165 \leq r \leq 170$ and $175 \leq r \leq 180$. The remaining sections $170 \leq r \leq 175$ and $180 \leq r \leq 185$ corresponds to the polar layers.

Figure 4.11 shows the distribution of the axial stress of all simulations over the radius. Two conspicuous characteristics can be recognised in this diagram. Firstly, in the reference solution (single red line), the hoop layers carry less axial load, and the polar layers carry more axial load than most of the curves. Secondly, an outlier group in the curves does not follow the constant course of most of the curves in the polar layers. The majority of the results agrees qualitatively with the reference solution across the thickness but differs quantitatively. This deviation cannot be attributed to specific simulation parameters. It is therefore assumed that the axial load is incorporated into the model differently in the software than in the simulation models.

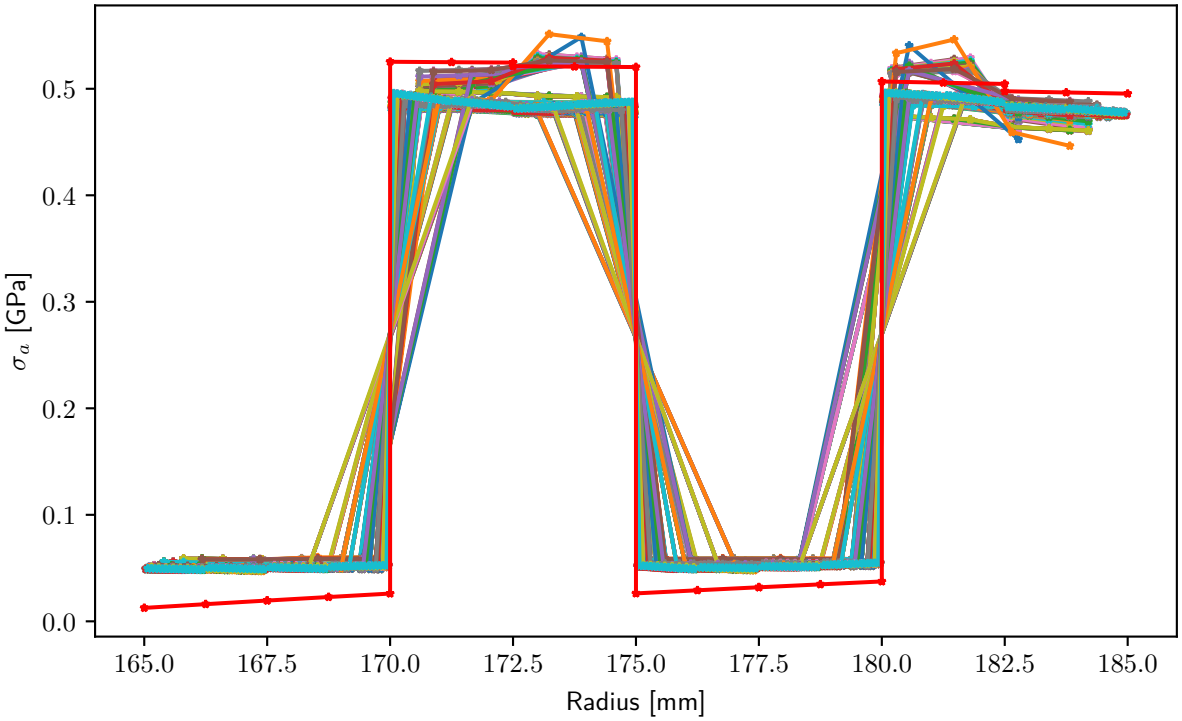

Figure 4.11: Axial stress over the radius (all simulations of basic investigation)

Figure 4.12 shows the radial stresses. The diagram can be divided into three groups of curves. The first group are the curves that are constant at 0 GPa. They represent the configurations with shell elements. For these elements, stresses perpendicular to the shell surface are not defined and therefore cannot be calculated. For clarification, only the configurations with shell elements are shown in Figure 4.12 in Appendix C. The main part of the curves forms the second group. It is characterized by a stepped curve from about -0.07 GPa to about 0 GPa. The width of the steps varies between the individual configurations. All curves that do not belong to the first or second group are assigned to the outlier group. This includes the stepped curves, which do not increase constantly, and the curves, which are significantly above the values of the second group. The curves of the outlier group are analysed in more detail in the diagrams below.

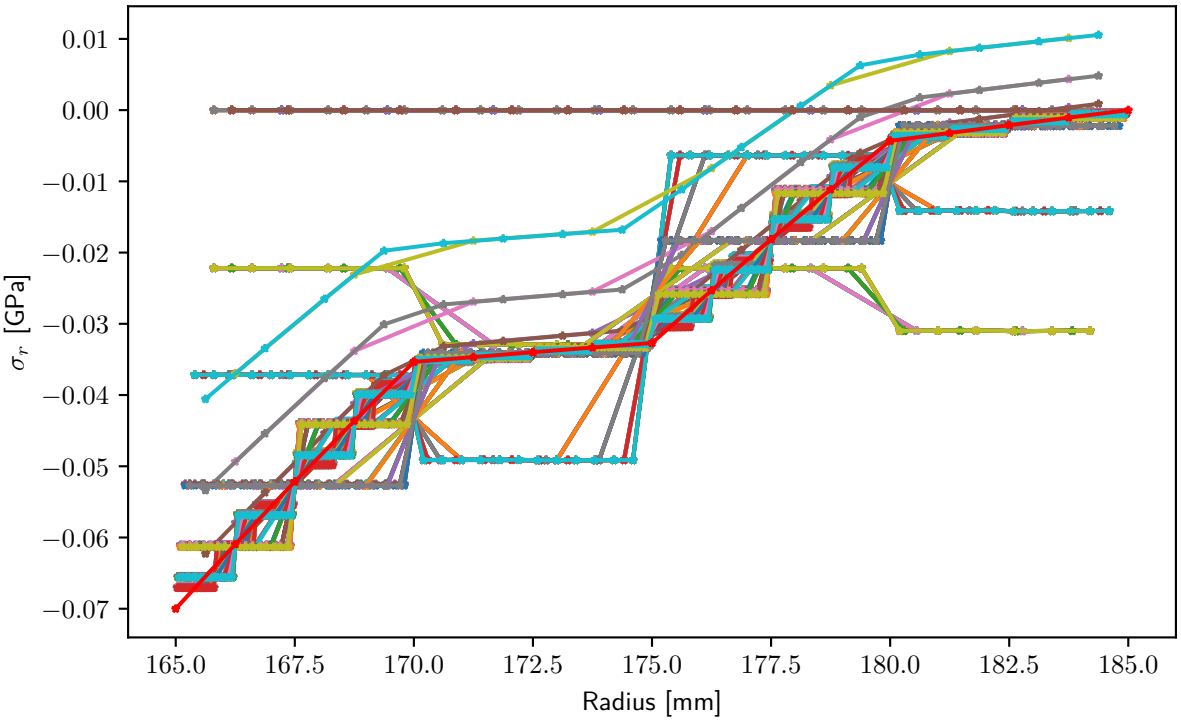

Figure 4.12: Radial stress over the radius (all simulations of basic investigation)

The third diagram on the stresses (Figure 4.13) provides an overview of the tangential stresses. The main part of the curves is slightly above the reference solution. An outlier group can be clearly seen, which has significantly lower values in the area of the inner tangential positions (left in the diagram) and slightly higher values in the area of the outer tangential positions (middle right). In addition, this group is characterized by an increasing curve in the areas, while the reference solution shows a decreasing curve.

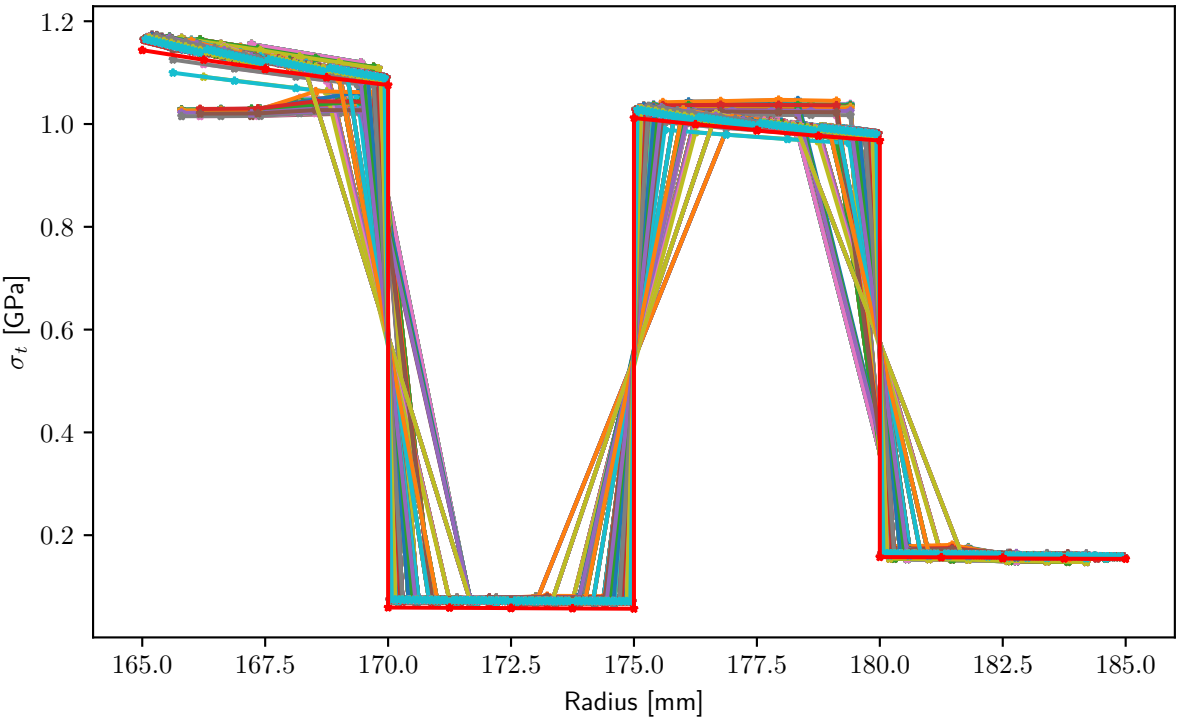

Figure 4.13: Tangential stress over the radius (all simulations of basic investigation)

In the following, the particularities are examined in more detail and assigned to individual parameters or parameter values. The radial stress of solid elements is shown in the following diagram (Figure 4.14). All configurations with an explicit solver are shown here, while the results of the configurations with implicit solvers are shown in Figures C.1, C.2 and C.3 in Appendix C. The diagram shows that when using an explicit solver, a fine mesh is required to achieve good results. The configurations with an element size of 2.0 achieve the only results in this study that approximately correspond to the reference solution. Since the number of elements in the radial direction has no influence on the course of the curves, it can be stated that as many elements as possible are required in the circumferential direction for a good result. The same effect can also be seen with axial and tangential stress. However, it is much less pronounced there.

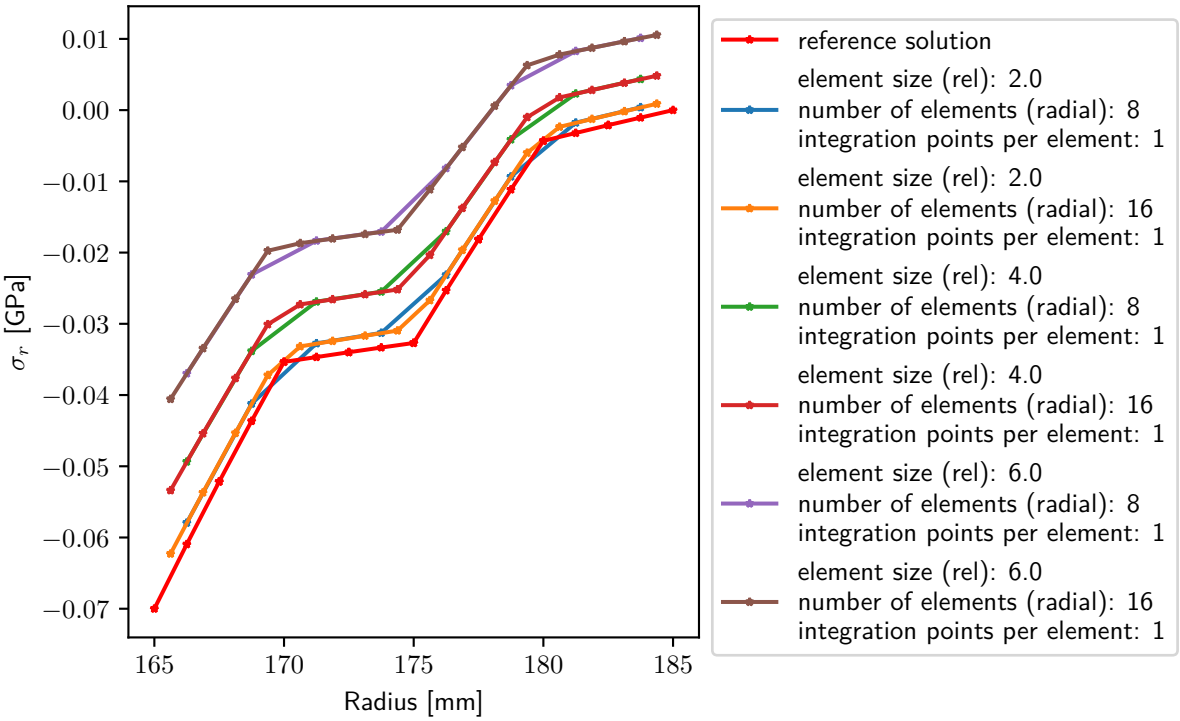

Figure 4.14: Radial stress over the radius (element type: solid, solver: explicit)

All implicit simulations with solid elements deliver the same results. The results agree with the majority of the results (cf. Figure 4.11, 4.12 and 4.13).

The next two diagrams show the results of the configurations with shell elements. Only the diagrams for axial and tangential stress are shown (Figure 4.15 and 4.16). The curves for the radial stress are known and can be viewed in Appendix C (Figure C.4). The results correspond to a large part of the deviations from the overview diagrams of the axial and tangential stress. As all curves show the same qualitative and similar quantitative deviations, the effects of individual parameters are not investigated in this case. The deviations are attributed to the unsuitability of shell elements for thick-walled geometries. It is shown that the definition of several integration points in the thickness direction enables the shell elements to represent the layer structure in the stresses. Nevertheless, the missing out-of-plane stresses and strains and their effect on the in-plane stresses and strains mean that the results are a rough approximation, but not a good solution. In addition to the displacement diagrams, the stress diagrams also show that the shell elements are not suitable for modelling this thick-walled geometry well.

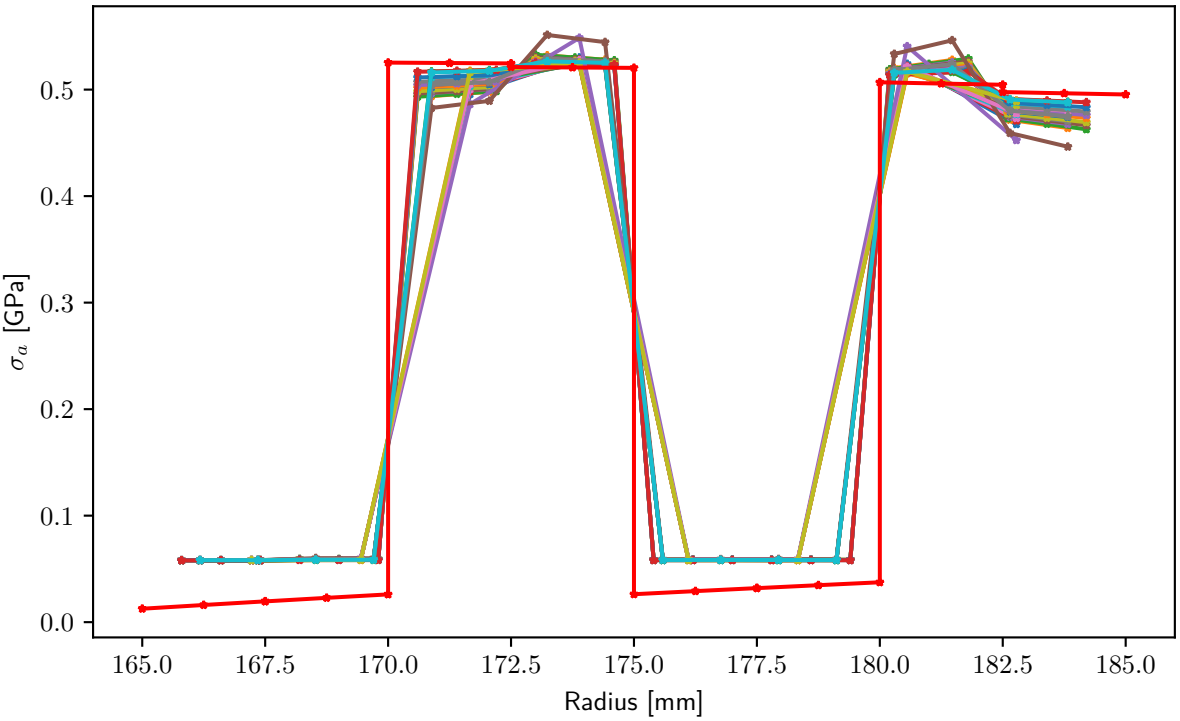

Figure 4.15: Axial stress over the radius (element type: shell)

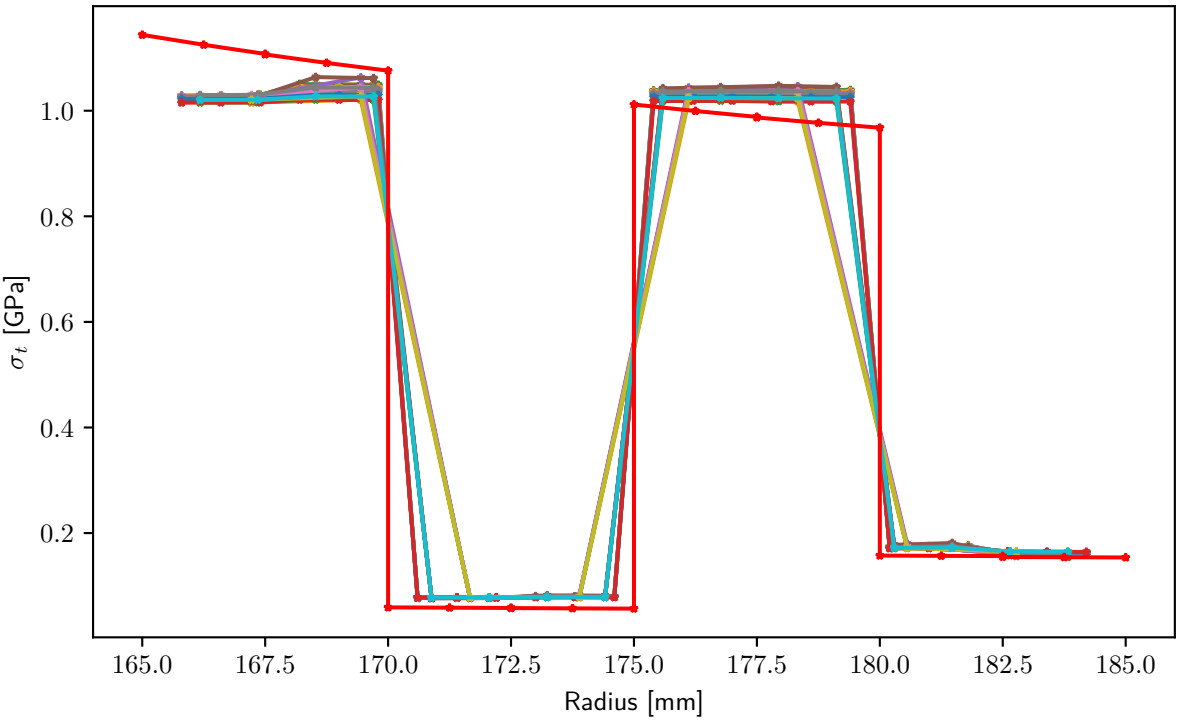

Figure 4.16: Tangential stress over the radius (element type: shell)

Figure 4.17 shows the tangential stresses of all simulations with tshell elements. The diagram shows a maximum deviation of 5% from the reference solution for all configurations. This means that the result of all configurations is calculated with sufficient accuracy. For this reason, only axial and radial stresses are discussed below.

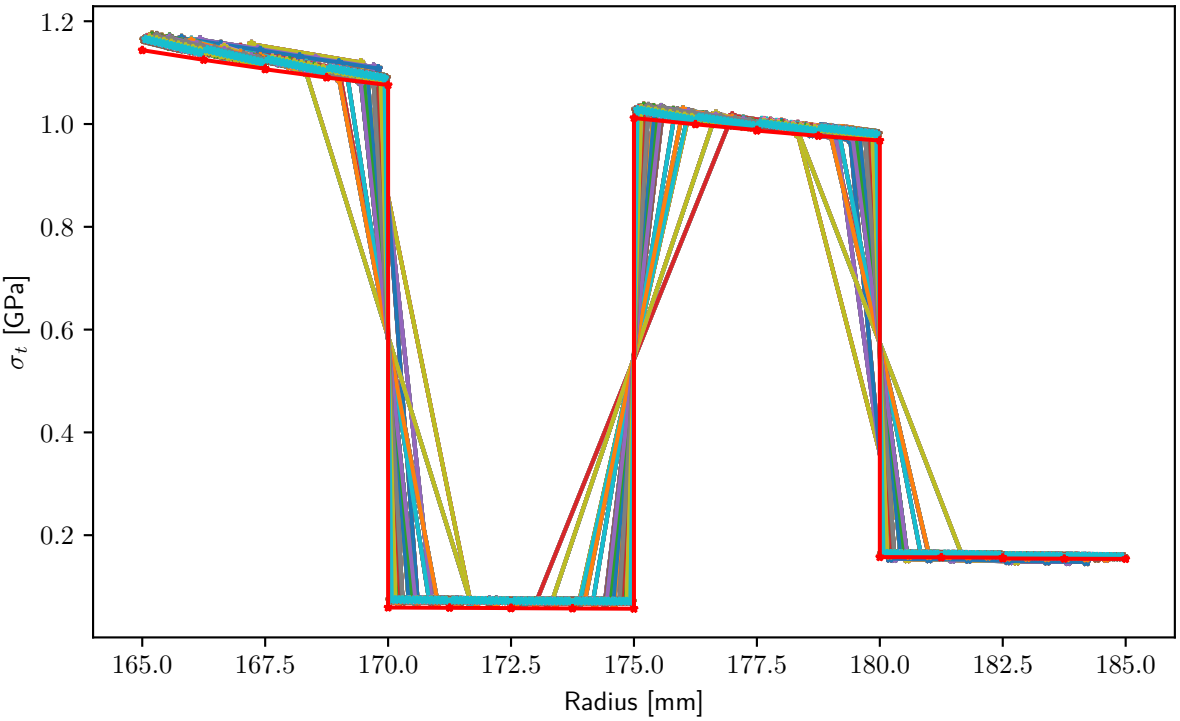

Figure 4.17: Tangential stress over the radius (element type: tshell)

In the next diagram (Figure 4.18), the results of the configurations with tshell elements are examined in more detail. The diagram shows the axial stress for models with different numbers of elements in the thickness direction. Fixed values were chosen for all other parameters (see caption). The majority of the curves corresponds to the the curves from the overview diagrams (Figure 4.11). The deviation from the reference solution is also already known. In addition, modelling with few elements in the thickness direction leads to deviations in the curves. This can be seen in the curve for one element in the radial direction (orange). The deviation is due to the same reason as the deviations for the shell elements. The deviations are slightly smaller than for the shell elements because a constant value for the out-of-plane stresses and strains is determined for the entire element instead of none. A constant value is better than none (shell elements), but not enough to be able to determine the stresses in the structure well. It can be concluded from this that, one element in the thickness direction is not sufficient to accurately represent the axial stress. All other variants with 2 or more elements in the thickness direction and implicit and explicit solvers lead to approximately the same results. Increasing the element size leads to slightly less accurate values, but not to significant deviations (see Figure C.5 in Appendix C).

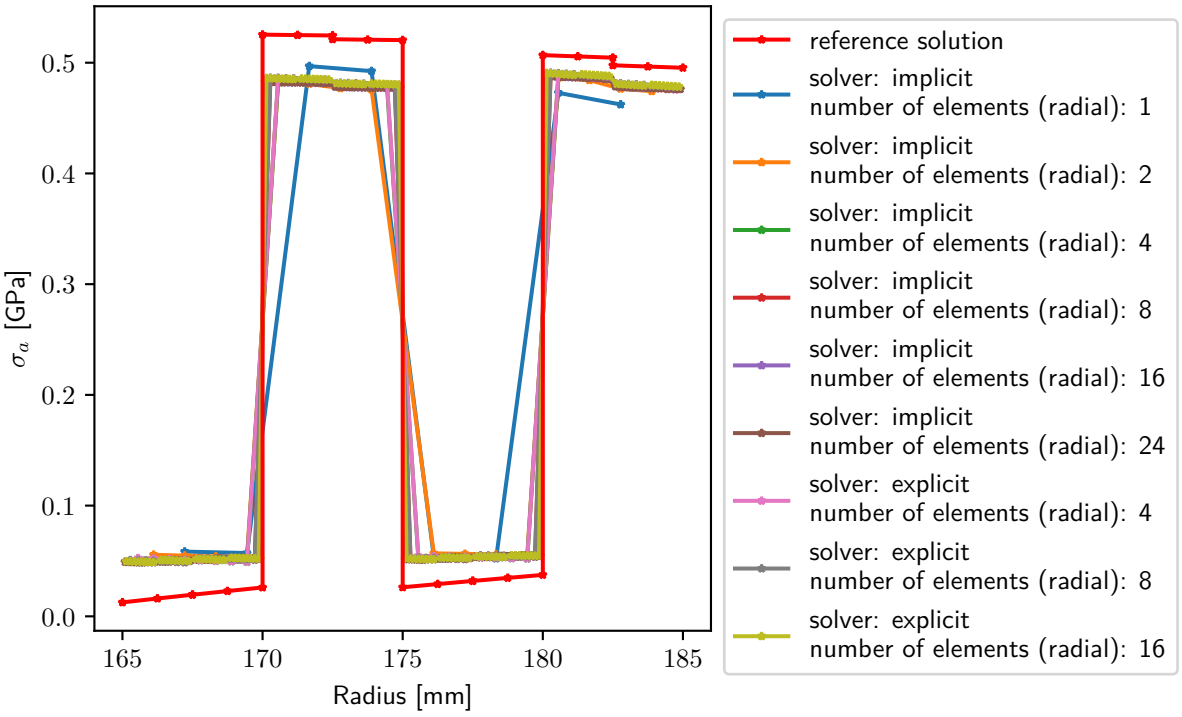

Figure 4.18: Axial stress over the radius (element type: tshell, element size: 2.0, number of integration points: 8)

Figure 4.19 shows the radial stress for the same configurations as the previous diagram. To be able to interpret the results, it must be remembered that tshell elements can only calculate one value for the stress in the thickness direction (see Section2.2.2). This value is assigned to all integration points. As a result, the radial stress is shown in the stair-step progression in the diagram. To be able to compare the results with the reference solution, each step is combined to its mean radius. If this is done, almost all these virtual points lie on the curve of the reference solution. Two deviations can be recognised. The points for one or two radial elements do not match the reference solution. It is noticeable that the curve is not only quantitatively but also qualitatively different.

One reason for this could be that the stress calculation is insufficient for a combination of layers with very different fibre angles in one element. This means that each layer would require its own element. In addition to configurations with eight or more elements, the configuration with four elements also delivers good results. This can be attributed to the angle-ply sublaminates. Whether the layer is rotated in the positive or negative direction makes no difference to the radial stress in this model, if both layers are rotated by the same angle.

As with the axial stress, a coarser mesh also leads to a slightly unclean curve for the tangential stress, but the deviations are not significant (see Figure C.6 in Appendix C).

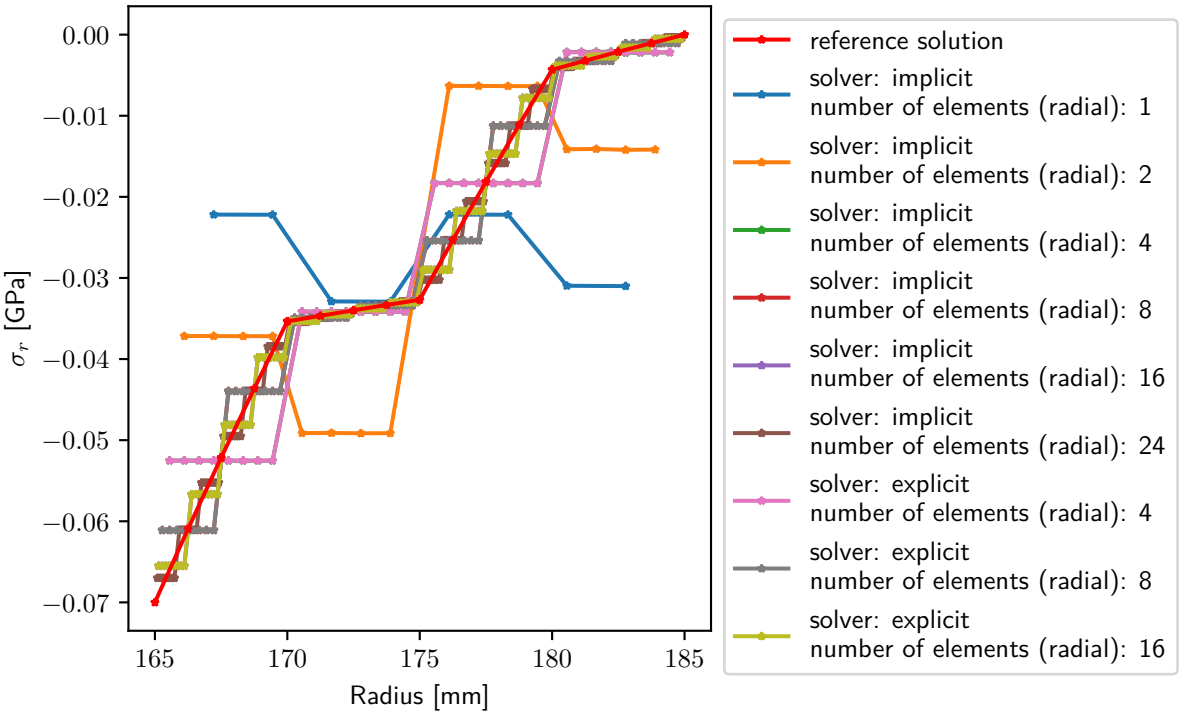

Figure 4.19: Radial stress over the radius (element type: tshell, element size: 2.0, number of integration points: 8)

Varying the number of integration points does not have a significant effect on any of the stress components (see Figures C.7, C.8 and C.9 in Appendix C).

Simulation Time

This section compares the simulation time of the different configurations. The simulation times of the explicit simulations are by a factor of ten longer than those of the implicit simulations. Therefore, the simulations times are shown in two different figures. The first figure (Figure 4.20) shows the simulation times of the implicit simulations and the second figure (Figure 4.21) shows the explicit simulations.

Each of the figures consists of six diagrams. Each diagram represents one of the variation parameters per axis. This means that every possible pair of two variation parameters is shown once. This detailed representation enables a precise analysis of which parameters have an influence on the simulation time and how large this influence is.

The simulation time is indicated in the diagrams using a colour scale. It should be noted that a field in the diagram only has two defined variation parameters, for example element type tshell and number of elements 8. Several configurations have these parameter values, for example a configuration with 2 integration points per element and one with 4. As only one colour can be displayed per field, only the mean value of the values of all matching configurations is shown.

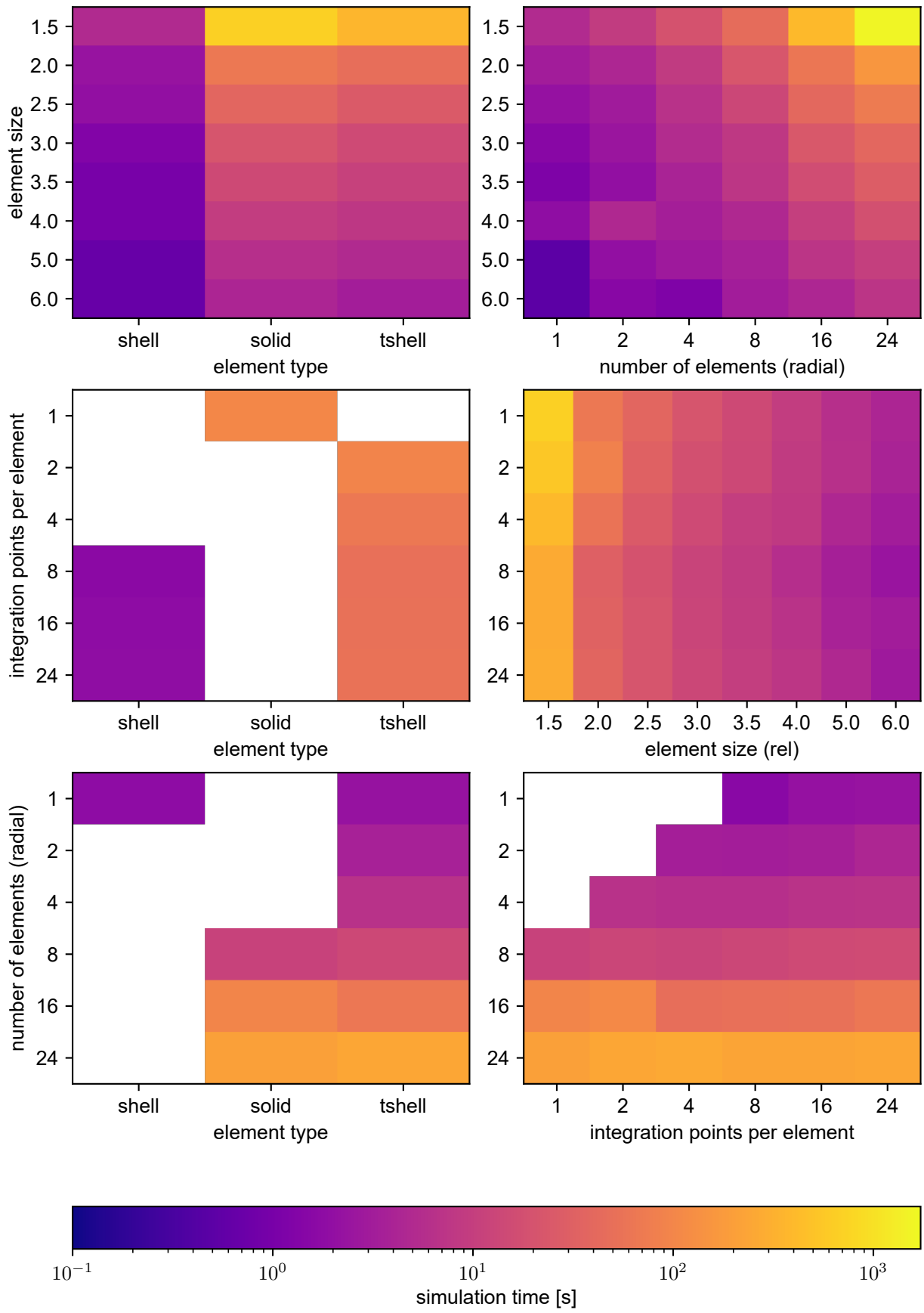

Figure 4.20: Simulation time of all implicit simulations

Three conclusions can be drawn from the diagrams: Fist of all, shell elements require significantly lower simulation times, while the simulation times of solid and tshell elements are very similar (see diagrams in the left column). Secondly more elements / nodes in the model result in longer simulation times (see diagram top right). And thirdly varying the integration points does not lead to a significant change in simulation time (see diagram centre right and bottom right). The first two findings were to be expected. Shell elements require less computational effort, which leads to faster simulation speeds (cf. Section 2.2.2). The number of calculation steps per time step (explicit) and the size of the matrix to be solved (implicit) is dependent on the number of nodes. This means that more nodes and therefore more elements lead to longer simulation times. The third realisation is not as expected. The calculation of a larger number of integration points should lead to an increased calculation effort. The fact that the simulation time and thus the calculation effort only increases minimally is not intuitive, especially if you compare it to the explicit simulations (see next page). A possible explanation for this could be that the calculation of the integration points when using the implicit solver is significantly less time-consuming than the calculation of the node displacement. Why this is the case could not be determined in this thesis.

The durations of the explicit simulations show a very similar behaviour compared to the implicit simulations (see Figure 4.21). However, two fundamental differences can be recognised. Firstly, the simulation times are approximately ten times longer (see colour scale) and secondly, the number of integration points has a noticeable influence on the duration (see diagram centre right and bottom right).

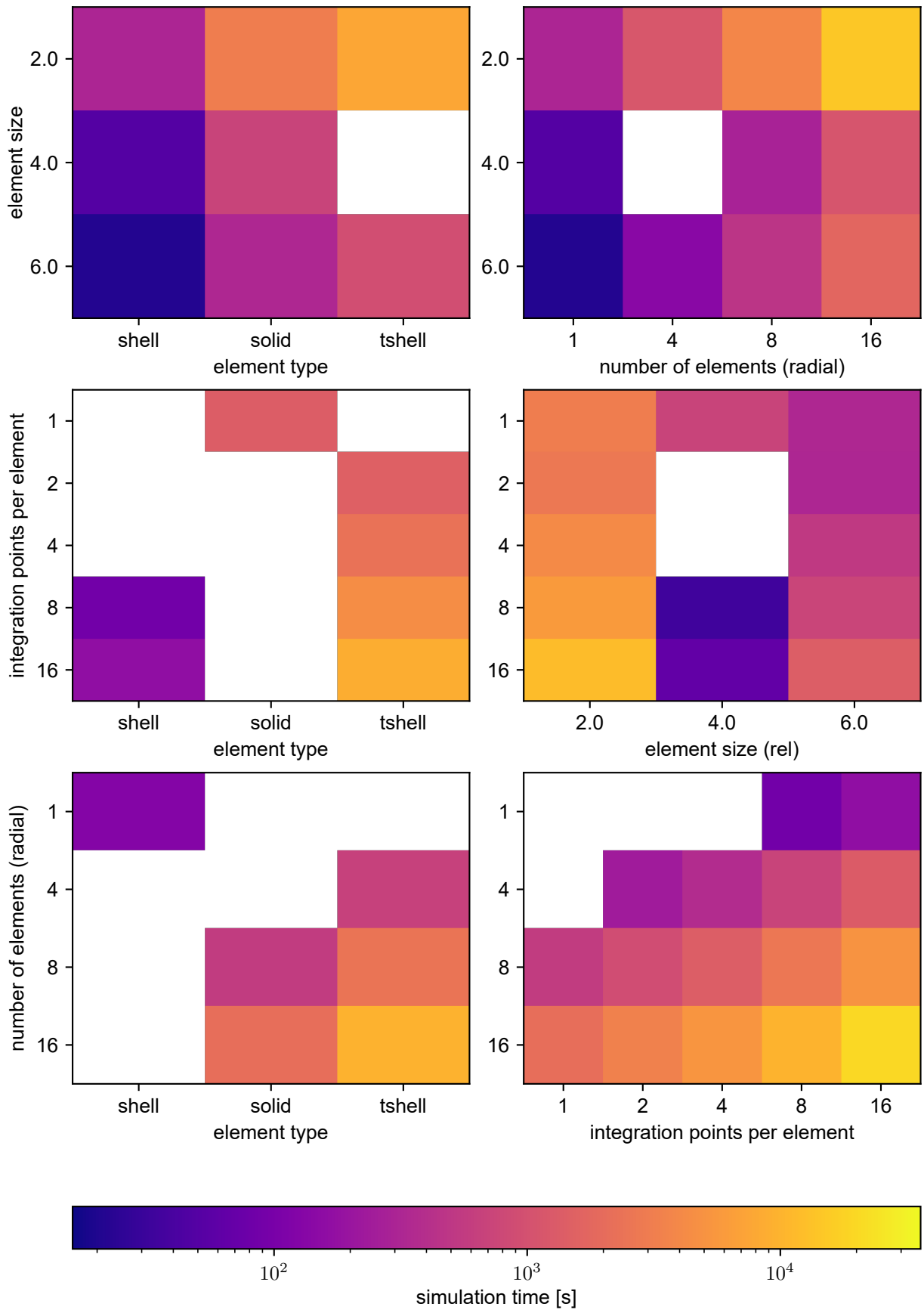

Figure 4.21: Simulation time of all explicit simulations

4.3.3 Mesh Convergence

This section analysis how refining the mesh affects the results (in this case the stresses). The results of this section are not used to evaluate the configurations, but to assess the significance of the results presented above. Specifically, the question arises as to whether the deviations from the reference solution shown could be caused by a mesh that is too coarse. Two aspects of mesh convergence are analysed below. Firstly, the changes in the stress values during the refinements are analyzed and secondly, a value for a theoretical element edge length of 0 mm is estimated using a simplified form of Richardson Extrapolation (RE).

For convergence analysis, it is common to compare models whose element edge length has been halved or doubled. For this reason, only the configurations with element sizes of 1.5, 3.0 and 6.0 are considered. To calculate the change in stresses and the RE, groups of three are formed from the configurations, whose parameter values differ only in the element size parameter. The change in stress and the value of the RE are determined from these groups of three for each calculation point (integration point) and each stress direction (axial, radial and tangential).

Stress Change

When analysing the change in stress during the refinement steps, a value must be selected from which the mesh and therefore the model is considered to have converged. In this case, a change in stress of 1 % is selected as the limit value. If the stress value changes by 1 % or less during a refinement step, the mesh is considered to have converged. It should be noted that it is not the aim of this work to obtain a converged mesh for all models. The investigation of convergence should only provide an indication of whether deviations could be attributed to an insufficiently fine mesh and whether further refinement of the mesh would lead to a (significant) change in the stress values. In addition, if the convergence error is known, it is possible to perform fast simulations on a coarse mesh and subsequently take the error into account when evaluating the results.

The following results were obtained from the convergence analysis. In the first refinement (6.0 to 3.0), 75.8 % of all analysed values fulfil the convergence criterion. The change in stress from the coarse mesh (6.0) to the medium mesh (3.0) is greatest for the radial stress. In the most extreme case, the stress value changes by 26%. Furthermore, larger changes occur in the axial stresses (up to 8 %). The smallest stress changes (up to 2 %) occur with the tangential stresses. If only the solid and tshell elements are considered, all the analysed values for the tangential stress fulfil the convergence criterion. After the second refinement (3.0 to 1.5), 97 % of all evaluation points fulfil the convergence criterion. Slightly increased changes only occur for some axial stress values and are up to 2.3 %. The evaluation shows that almost all of the analysed points converge for the finest mesh (element size 1.5). The few points that do not fulfil the convergence criterion are so close to the limit value that the error caused by the discretisation should only have a minor influence on the results of the investigations.

Richardson Extrapolation (RE)

This section shows how a RE with simplified equations can be used to determine a mesh-independent value for the stress from stress values for different element sizes. The group of three configurations 1, 10 and 22 is used as an example. All three configurations use the same parameter values (element type: solid, number of elements (radial): 8, integration points per element: 1, solver: implicit) and differ only in the mesh size (config. 1: 1.5, config. 10: 3.0 and config. 22: 6.0). The group therefore fulfills the condition (see section 2.3) that the ratio of the element sizes changes twice by the same factor (factor 2). This example is illustrated using the tangential stress.

The values from Table 4.5 are used to calculate the mesh-independent stress at each calculation point (integration point). The units can be neglected in the calculation as long as all values in a row have the same unit. As this is the case in Table 4.5, they are ignored in this case for the sake of clarity.

Table 4.5: Initial stress values of each layer for calculating the mesh-independent tangential stress values from configurations 1, 10 and 22

Configuration number	1	10	22
Index in equation	1	2	3
Mesh size	1.5	3.0	6.0
Layer 1	1.1430	1.1428	1.1417
Layer 2	1.1074	1.1073	1.1063
Layer 3	0.0731	0.0732	0.0733
Layer 4	0.0714	0.0715	0.0717
Layer 5	1.0139	1.0137	1.0112
Layer 6	0.9920	0.9918	0.9902
Layer 7	0.1618	0.1621	0.1627
Layer 8	0.1588	0.1587	0.1585

These values are inserted at the corresponding places in equations 2.7 and 2.8 from Celik et al [38] (cf. Section 2.3). Each equation is applied once per layer. Here, ϵ_{32} stands for the difference of the respective stress values $\phi_3 - \phi_2$ and ϵ_{21} for $\phi_2 - \phi_1$ (specified in the table for each layer) and $r = 2$ for the mesh size ratio (specified once for all layers in the table).

$$p = \frac{ln(\frac{\epsilon_{32}}{\epsilon_{21}})}{ln(r)} \tag{2.7}$$

$$\phi_{h=0} = \phi_1 + \frac{-\epsilon_{21}}{(r)^p - 1} \tag{2.8}$$

This results in a mesh-independent value for each calculation point. Figure 4.22 shows an example of the stress values of the three configurations together with the calculated value for the data point of the innermost layer. For clarification, the mesh-independent value is also shown with the dashed line.

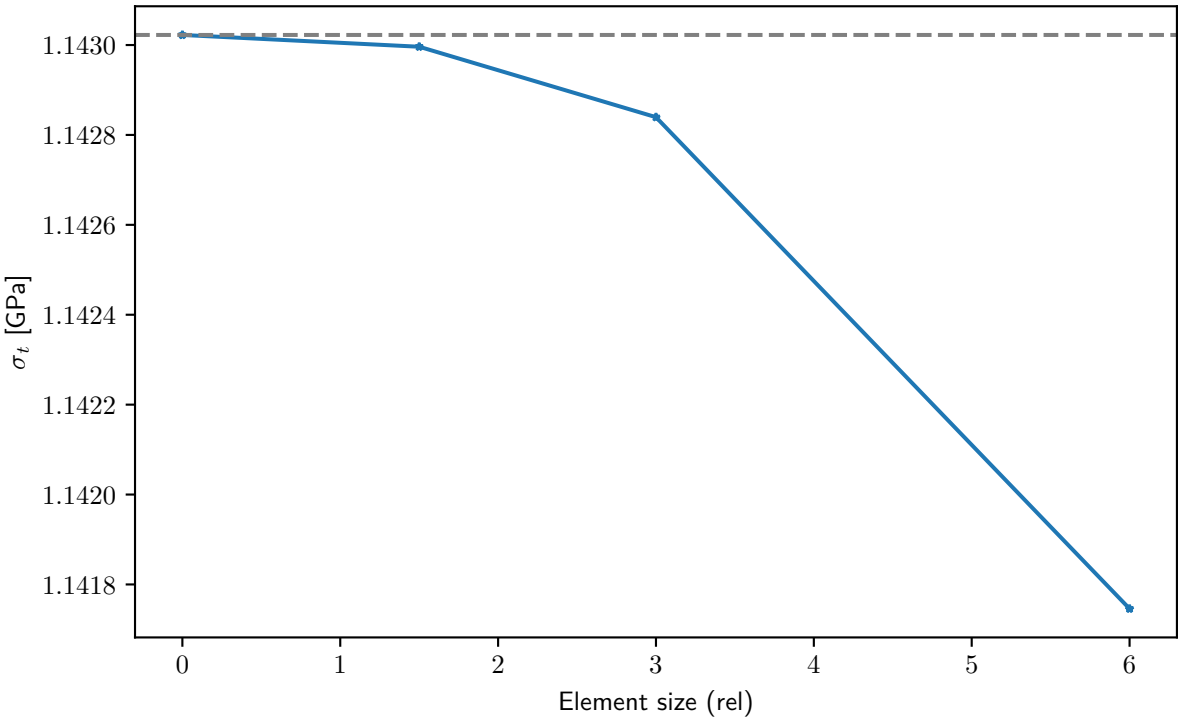

Figure 4.22: Convergence curve and asymptote (mesh-independent value) of the Richardson Extrapolation for the tangential stress of the innermost layer of configurations 1, 10 and 22

The values calculated for all calculation points result in the curve over the radius shown in Figure 4.23.

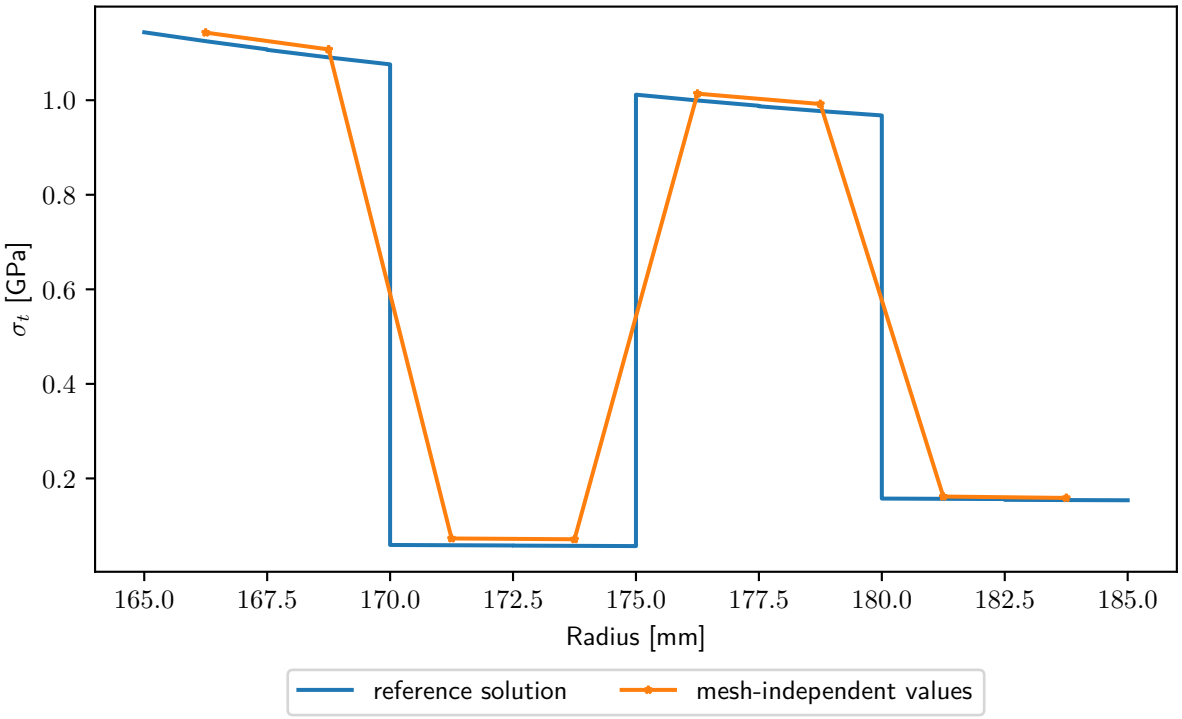

Figure 4.23: Mesh-independent values over the radius compared to the reference values

Figure 4.23 shows that the mesh-independent values match the values of the reference solution well. Figure 4.22 also shows that the discretisation error between the fine mesh (element size 1.5) and the mesh-independent solution is negligible at <0.01 %. Even the difference between the coarse mesh (element size 6.0) and the mesh-independent solution is very small at <1 %. In summary, it can be said that the discretisation error is negligible for all the results shown.

The example shown here is one of the few examples where the application of RE was possible. For many evaluation points, no increasing or decreasing behaviour of the values across all three element sizes was discernible. They showed an oscillating or, in rare cases, constant behaviour instead. An evaluation of this behaviour is not possible with the RE equations presented here. However, the example in which an evaluation was possible and the previous investigation of the change in values shows that the discretisation error is small for all element sizes. The fluctuating behaviour in the values can therefore be explained by the fact that other effects (e.g. numerical effects and inaccuracies) have a greater impact on the results than the discretisation.

By analysing the change in stresses and calculating the mesh-independent values using RE, it was possible to prove that the discretisation error is small for all element sizes and is so small for element size 1.5 that it can be neglected.

4.3.4 Result Evaluation

In the evaluation, a distinction is mainly made between configurations with shell elements and configurations with solid or tshell elements. The shell elements provide results with large deviations in comparison to the other elements. Particularly when analysing the displacements, shell elements are not able to display the displacements well due to the limited number of nodes. In the case of stresses, the integration points of the elements allow the results to be rough approximations. Due to this and the fact that shell elements have significantly shorter calculation times than the other elements, shell elements are suitable for rough predictions. Early in the development process, where it is more important to have fast simulation times and a rough approximation is sufficient as a result, these elements can be used effectively. But they are unsuitable for advanced stages in the development process, as the accuracy of the results is no longer sufficient.

All configurations with 3D elements (solid and tshell) deliver the same results with a few exceptions. These are the configurations with solid elements and medium to coarse mesh and configurations with tshell elements and less than four elements in radial direction. It must be considered that the deviations mainly occur in the radial stresses and displacements, while they are not recognisable in the tangential stresses. As the tangential stress is an essential variable in the tank design, while the radial stress is mostly neglected, this deviation can be accepted under certain circumstances. Especially with tshell elements, where the simulation time can be reduced by using fewer elements in the radial direction, configurations with fewer radial elements could be appropriate.

The following conclusion can be drawn from the remaining configurations which provide good results. In most cases, a particularly large number of elements or integration points only leads to an increase in simulation time without significantly improving the results. The mesh size in particular had no influence on the results in most cases and even the coarsest mesh delivered good results. For further investigations, it must be taken into account that a very simple model with simple boundary conditions was selected in this study. It may well be that more complex models could benefit from a refinement of the mesh.

Based on these findings, the following parameter values are eliminated for the next analysis. The reasons for the elimination are given before each group of bullet points.
Long simulation time without significantly better results

- 24 integration points
- 16 integration points (configurations with explicit solver)
- 24 elements in radial direction

Too large a deviation in the results

- elements in radial direction

Minor influence on results

- Element sizes 1.5, 2.5, 3.0, 3.5, 5.0

Shell elements are still considered in the next investigation since the investigation is small in scope and model complexity and the simulation times of the elements are short.

4.4 Burst Pressure

The burst pressure is one of the most important parameters in the design of a pressurised tank. For this reason, this study examines how well the burst pressure can be determined with the chosen configurations.

4.4.1 Parameter Values

Based on the results of the basic investigation, the number of configurations can be greatly reduced. The values of the adjusted parameter list are shown in the following table.

Table 4.6: Parameter Values of Burst Pressure Investigation

Element Type	Integration Points	Element Size (rel)	Number of Elements (thickness)	Solver
solid	1	2.0	1	implicit
shell	2	4.0	4	explicit
tshell	4	6.0	8	
	8		16	
	16			

These values result in 96 possible configurations. As with the Basic Investigation, all implicit simulations and a reduced number of explicit simulations are carried out due to the computational effort involved. All variants with 16 integration points are omitted from the explicit configurations. This results in a total of 78 configurations for this investigation.

4.4.2 Determination of the Burst Pressure

Due to the rotationally symmetrical geometry and the uniform layer structure over the circumference and length, the structure fails globally and not locally. This global failure makes the simulation of the failure considerably more difficult, as it is no longer possible to calculate the stresses with the simulation methods used once the failure has occurred. The solver cancels the solution progress at this point. A possible solution for evaluating the burst pressure would be to determine the pressure of the last successful calculation point. This method has a major weakness. The results depend on the time interval between the last successful calculation point and the failure point. This problem is less noticeable for explicit simulations, as the intervals between the calculation points are small. Implicit simulations, on the other hand, do not lead to usable results as the distances between the calculation points are too large. In addition, it is difficult to compare the results with each other, as the step size in explicit simulations is selected dynamically by the algorithm.

To avoid the problem of simulating the failure, the tank is simulated without failure, i.e. the layers are simulated with linear elastic material, and the failure is then calculated in the post-process. In this study, the failure is evaluated using the maximum stress criterion for fibre failure. This simple criterion was chosen because reference values are available and the evaluation scripts from the previous section can be largely reused. This method also allows other failure criteria to be used for further analysis in retrospect.

To determine the burst pressure, the stresses from the same ring of elements as in the first investigation are used (see Figure 4.6 in Section 4.2.4). The internal pressure at which the stress exceeds the limit value is determined for all stresses (from each element, integration point and calculation step). In this case, 2.37 GPa was selected as the limit value. The value was taken from the same material data set as the remaining material data. The lowest internal pressure at which the critical stress is reached in any of the evaluated elements is taken as the burst pressure. This results in one burst pressure value for each configuration.

4.4.3 Simulation Results

For the visualization, the burst pressures of all simulations are divided by the reference value so that the deviations from the reference pressure can be shown in the diagrams. In the following diagram (Fig 4.24), all underestimates of the burst pressure (negative deviations) are shown in blue and all overestimates (positive deviations) are shown in red. The colour scale shows small deviations with pale colours and larger deviations with rich colours. Implicit and explicit configurations show no significant differences and are therefore shown in the same diagrams.

The following insights can be gained from the diagrams in the left-hand column of the diagram. Shell elements have by far the greatest deviations (around 7-11 %). The red colour shows that the burst pressure is overestimated. In addition to the large deviation, this is even more critical, as an overestimation harbours a greater risk than an underestimation, as the tank would burst before reaching the determined burst pressure. The results of the configurations with solid elements are very close to the reference value (between $\pm$2 %). The diagram at the top shows that the burst pressure increases with coarser meshes. Configurations with tshell elements show small negative deviations (>-5 %).

The diagrams in the right-hand column provide hardly any new insights. The diagrams in the top right and centre right mainly reflect the findings from the left-hand column, as some parameter values only apply to certain element types (e.g. one element in the radial direction is only covered by shell elements and configurations with one integration point only apply to solid elements). The diagram at the bottom right is again indirectly divided by element type. Solid elements are on the left and shell elements at the top for the same reasons mentioned before. The 3x4 block at the bottom right shows the tshell elements. From these the most accurate results (in relation to the reference solution) are obtained with a minimum number of elements and integration points.

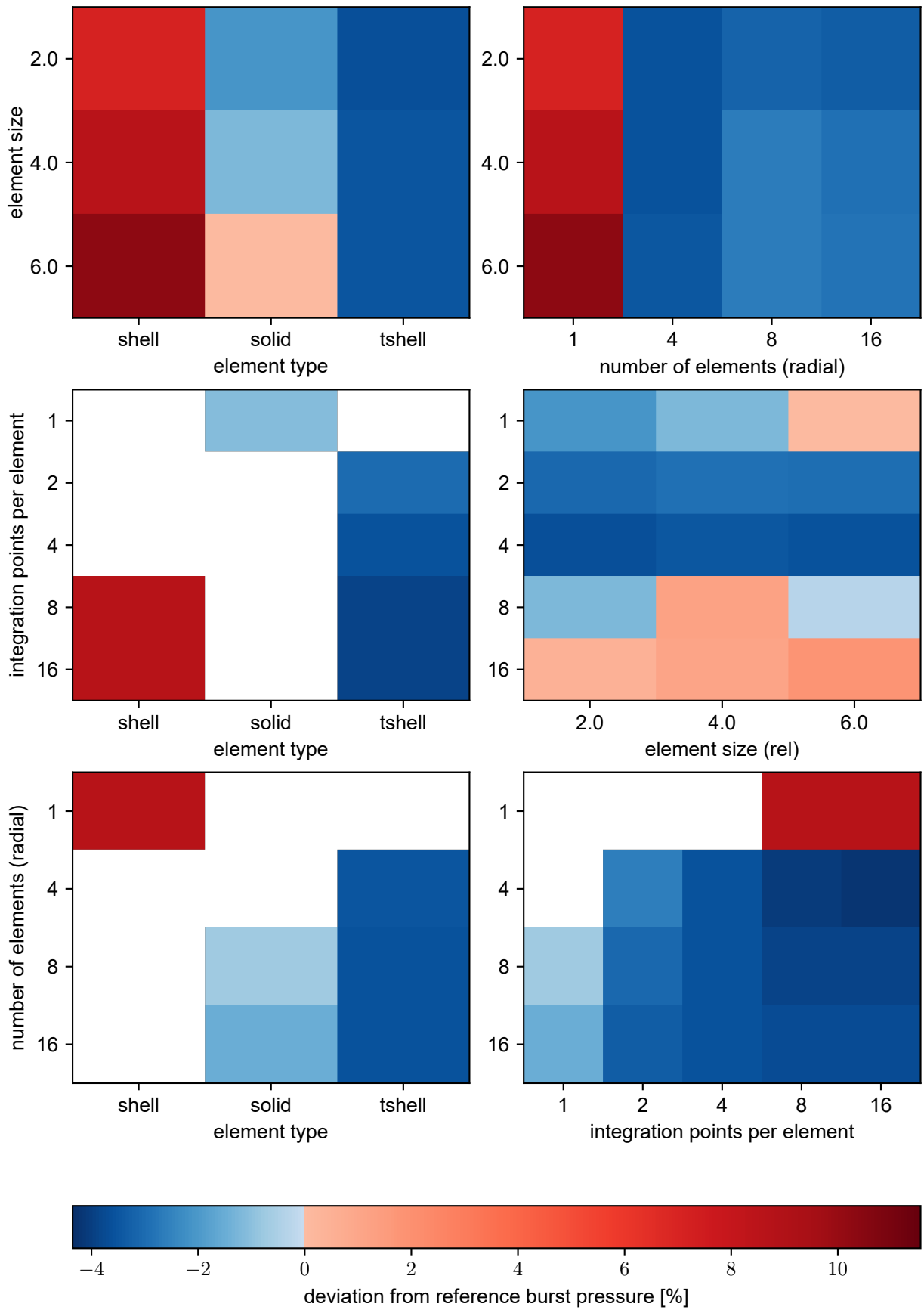

Figure 4.24: Burst pressure (relative deviation from the reference value)

4.4.4 Result Evaluation

Overall, the values reflect the results of the first investigation. This corresponds to the expectation, as nothing has changed in the simulation apart from the increase in load. The failure calculation only takes place in the post-process. It remains the case that the shell elements are not suitable for an exact simulation of the stresses, while solid and tshell elements behave very similarly. From the diagram type used in this section, the solid elements are somewhat closer to the reference solution than the tshell elements. However, due to the small deviations between the two element types, it cannot be directly concluded that solid elements are more accurate. It could be that the most precise values that can be achieved in LS-DYNA with this model do not correspond exactly to the reference value.

In addition to the expected simulation results, the main finding from this investigation is that it is not possible to simulate the failure with this geometry and these settings. To be able to simulate the failure, either a solver must be used that can handle the global failure or a geometry must be used that does not fail globally.

4.5 Gas Model

The goal of this investigation is to test different variants of modelling the internal pressure as a gas. The feasibility is to be examined, and the results validated on the basis of previous investigations (basic investigation). In the end, one method is to be selected that will be used in subsequent investigations.

4.5.1 Gas Model Choice

In LS-DYNA three basic methods are used to model the internal pressure as a gas. The methods are Control Volume Method (CV), Arbitrary-Lagrangian-Eulerian Method (ALE) and Corpuscular Particle Method (CPM). The methods differ in the way the gas is discretised. In the CV method, the volume is treated as one “element” with scalar variables such as temperature, pressure, or internal energy and boundary conditions. The ALE method uses a mesh for the discretisation and the CPM groups the gas particles and calculates the interaction between the groups and between groups and boundary conditions (see Section 2.2.3).

Only the CV method and the CPM are taken into consideration when selecting the appropriate gas model. The high modelling and calculation effort of the ALE method compared to the other two methods makes its use for a relatively simple load case impractical. The CPM method offers many advantages. The discretisation of the gas with particle groups is close to reality and at the same time enables a simple regulator between inaccurate faster simulations and more accurate slower simulations via the parameter of the number of particles used. In addition, this method can model significantly more effects, e.g. during the inflow of the gas or pressure waves during high-velocity impacts.

Due to these advantages, this method would probably be the best choice for further investigations. However, this is not possible as no stable model could be generated using this method. All models tested with this method showed strong dynamic effects in the structure. The dynamic behaviour was unstable, so that the simulation always failed at a certain point. It was not possible to determine which parameters were responsible for this behaviour. It is likely that the CPM would work but would require more background knowledge and time than is available in this thesis.

For these reasons, the CV method is chosen for the following analyses. Of all three variants, it offers the least capabilities for modelling physical effects. However, it is the fastest method and, in contrast to the CPM, also allows the use of implicit solvers. In addition, no effects occur in the models analysed that would be better modelled by other methods. This disadvantage therefore only relates to possible further investigations following this thesis.

Two keywords in LS-DYNA are useful for the specific implementation of the CV method for this model. The *AIRBAG_LOAD_CURVE keyword can be used, where the pressure on the gas is specified. Alternatively, the *AIRBAG_SIMPLE_AIRBAG_MODEL keyword can be used, where mass flow into the volume is defined. Of the two cases, the second is used for all further investigations, as it is closer to reality that a mass flow is specified instead of a pressure curve. In the further course of this chapter, simulations are carried out using this method and various parameter configurations in order to validate the model using the results of the basic investigation.

4.5.2 Simulation Model

The known geometry and boundary conditions from the basic investigation are used for the validation. It is possible to use the geometry that is open at the ends, as openings in the geometry are automatically closed with planar surfaces in LS-DYNA. This also means that no axial load is applied by the gas. For validation, the radial load is replaced by the gas, while the axial load remains as a direct load. Combinations of the parameter values shown in Table 4.7 are used to determine results for validation.

Table 4.7: Parameter Values of Gas Model Investigation

Element Type	Integration Points	Element Size (rel)	Number of Elements (thickness)	Solver
solid	1	1.5	1	implicit
tshell	2	3.0	4	explicit
	4	6.0	8	
	8			

All 66 possible configurations from these values are simulated. The list of these configurations can be viewed in Appendix A.

4.5.3 Simulation Results

In this section, the results of the simulations are presented and compared with reference values. As with the basic investigation, the values from the software tool are used as reference values. They are shown in the diagrams as a blue line. In addition, the results from configuration 75 are shown as a red line. The results of this simulation are chosen because they are well suited to represent the results from the baseline study. It is primarily used for the axial stresses, as a deviation also occurred there in the first investigation.

No deviations are recognisable in the simulation results from the reference values for radial and tangential stress. For this reason, the results are only presented in Appendix D and only the axial stress is discussed in this section. Figure 4.25 shows the axial stress of all simulations of this investigation.

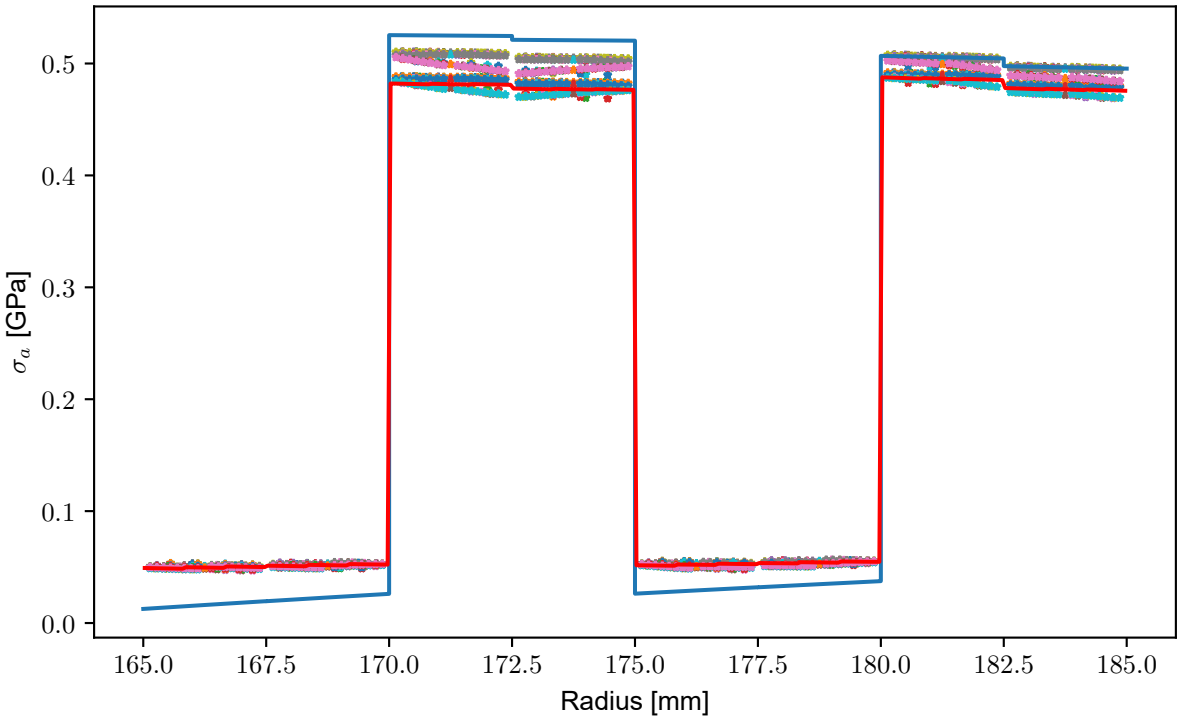

Figure 4.25: Axial stress over the radius (all simulations of gas model investigation)

From the course of the curves and the position of the points, the results for hoop layers match the reference value from the basic investigation very well. For the polar layers, some values fit well (e.g. blue markers), while two types of deviations can be recognised. On the one hand, some configurations have an upward offset of the stresses (grey markers) and on the other hand, configurations with a slightly v-shaped curve occur in the radius range between 170 mm and 175 mm (turquoise markers). A configuration with both types of deviations does also occur (pink markers).

Figure 4.26 shows a subset of the results that illustrates which parameter values are responsible for the offset.

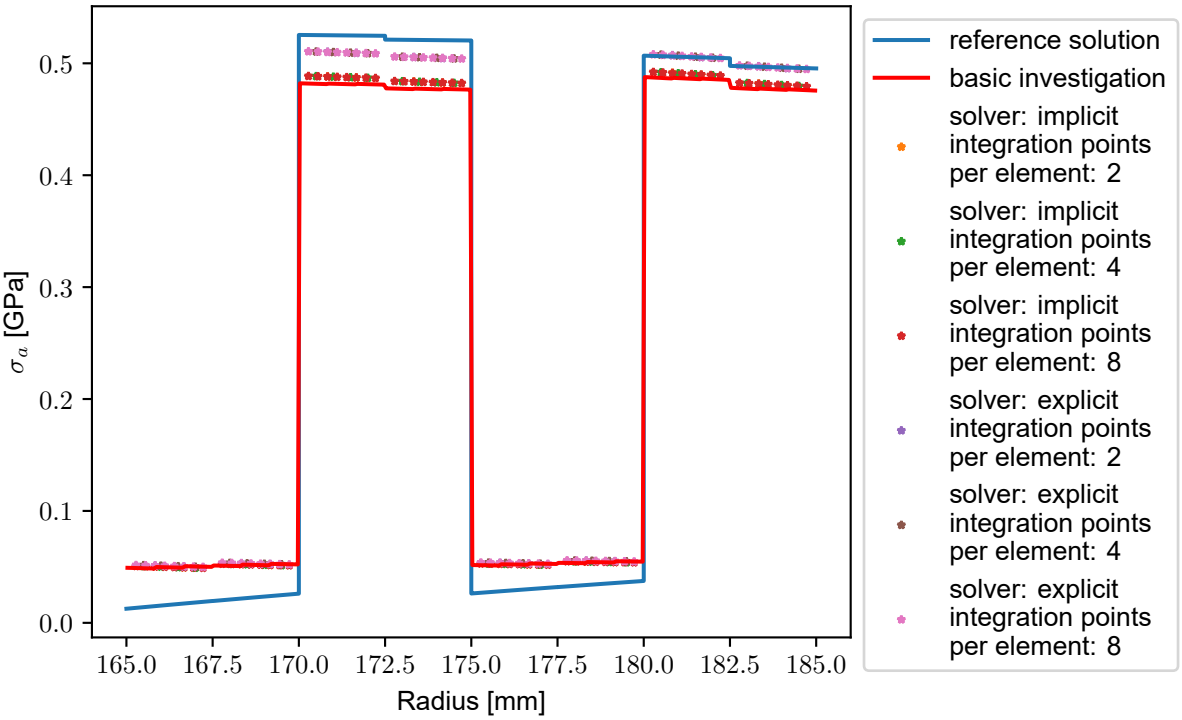

Figure 4.26: Axial stress over the radius (element type: tshell, element size: 1.5, number of elements (radial): 8)

The diagram shows that offset only occurs in simulations with an explicit solver. This applies to all explicit configurations and not just the configurations shown in this diagram. The fact that the deviation occurs in the explicit simulations could indicate that the interaction between structure and gas volume behaves differently with the small time steps of the explicit solver compared to the solution progress of the implicit solver.

Figure 4.27 shows a subset of the results that illustrates which parameter values are responsible for the v-shape.

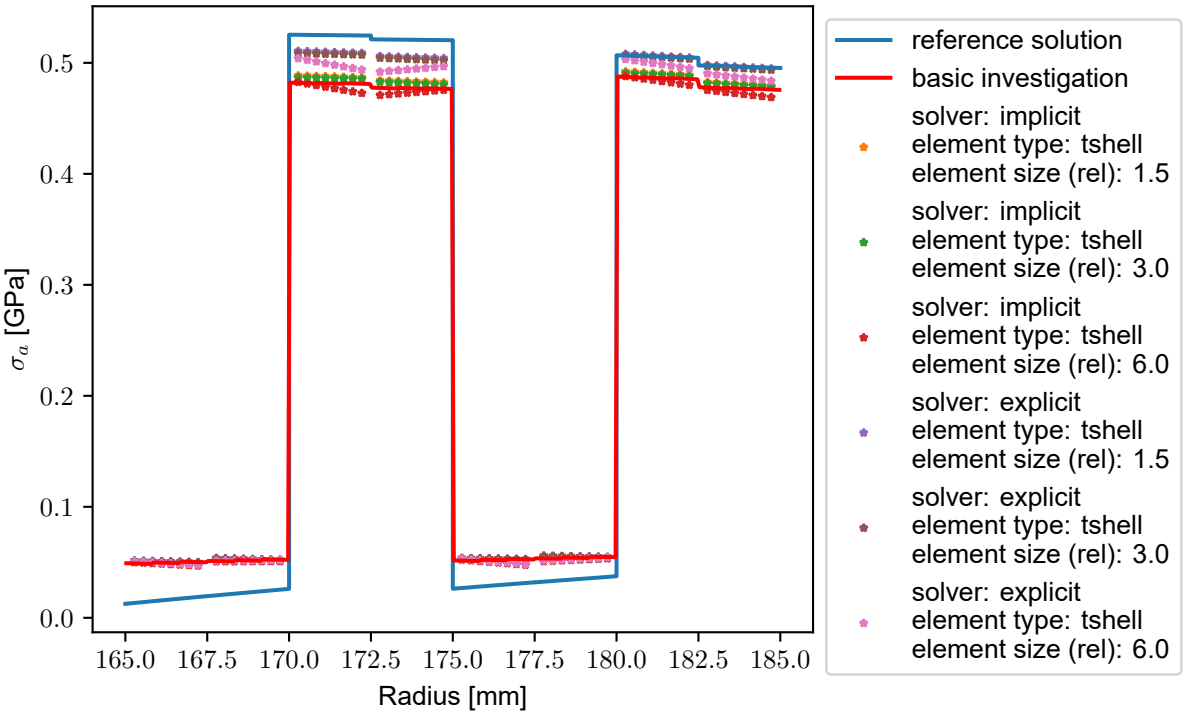

Figure 4.27: Axial stress over the radius (number of elements (radial): 8, integration points per element: 8)

The diagram shows that the v-shape only occurs in simulations with a coarse mesh (mesh size 6.0). As with the offset, this behaviour also applies to all configurations with this mesh and not only to the configurations shown in this diagram. Conversely, these findings show that all configurations with an implicit solver and a mesh size of three or finer deliver very good results for all three stress types. If the result of this investigation is compared with the simulation results of the basic investigation, it can be seen in Figure 4.11 that some configurations also exhibit the v-shaped curve in this investigation. The effect is much less noticeable there, as other effects and deviations are significantly greater. This means that the effect is not caused using the gas model. Why the v-shape occurs in the configurations with element size 6.0 could not be investigated as part of this thesis.

4.5.4 Result Evaluation

Two findings have emerged from the investigation of modelling the internal pressure as a gas. The first finding is that using the CV method is the best method for the transition between modelling the pressure as a load and modelling the pressure as a gas. It is easy to implement and can model the load on the structure well. However, it is limited in the results it can provide. If local effects in the gas volume or detailed inflow processes are to be considered, the use of the CPM is probably more suitable.

The simulation results have shown that the use of the gas model provides the same radial and tangential stresses as the models from the basic investigation. If only these stresses are relevant, the gas model can be used without restrictions. For the axial stresses, the use of the explicit solver showed slight deviations compared to the results of the basic investigation. If these stresses are particularly relevant, the use of the implicit solver may be more appropriate. If the use of an explicit solver is necessary, the results should ideally be verified with reference data.

4.6 Inter-Layer Model

The aim of this analysis is to investigate different ways of modelling the interface between the fibre layers. The first step is to analyse how the models with an inter-layer model (ILM) behave in comparison to models without an ILM. Then different ILMs will be compared with each other using an impact load case. At the end, one ILM is selected that is used for the final examination of the entire tank.

4.6.1 Implementation of Inter Layer-Models

Two basic ILMs are available in LS-DYNA. The interlayer can be modelled as a cohesive contact or as a cohesive element. In the case of a contact, the surfaces of the superimposed layers are connected to each other using a mathematical model. In contrast, cohesive elements are solid elements that are connected to the neighbouring elements via common nodes (see Section 2.2.4). In this ILM, the cohesive properties are defined in the material card. LS-DYNA offers different mathematical models for the simulation of inter-laminar failure. In this case, a bilinear model is selected as this is available for both ILMs. The keyword *CONTACT_AUTOMATIC_SURFACE_-TO_SURFACE_TIEBREAK is used for the contact and the material *MAT_COHESIVE_MIXED_-MODE (MAT_138) is assigned to the elements. The parameter values for both ILMs are shown in Table 4.8. The values are based on the principles of Turon et al. [46] and were adapted on the basis of experience from other projects.

Table 4.8: Parameters for ILMs

Parameter	Contact	Element
Normal energy release rate	$2.00 \cdot 10^{-3}$ J	
Shear energy release rate	$2.00 \cdot 10^{-3}$ J	
Tangential stiffness	100 $\frac{\text{GPa}}{\text{mm}}$	
Normal stiffness	100 $\frac{\text{GPa}}{\text{mm}}$	
Normal failure stress	equation (see below)	
Shear failure stress	equation (see below)	
Maximum failure stress	0.02	
Static coefficient of friction	0.4	
Dynamic coefficient of friction	0.4	
Mass density	-	$1.50 \cdot 10^{-6}$ $\frac{\text{kg}}{\text{mm}^3}$
Ultimate normal displacement	-	0.2 mm
Ultimate tangential displacement	-	0.2 mm

For the same failure stresses, larger elements (coarser mesh) fail significantly later than small elements. The reason for this is that larger elements and therefore a coarser mesh cannot resolve the sharp gradients in stress and displacement near the crack tip. This leads to a delayed crack initiation and propagation [46]. To obtain similar results with fine and coarse meshes, LS-DYNA offers the option of specifying values as a function of the element size. In this study, the approach of Turon et al [46] was used to determine the failure stresses. The same value was used for normal and shear failure stresses.

$$\bar{\tau}^0 = \sqrt{\frac{9\pi E G_c}{32 N_e^0 l_c}} \tag{4.2}$$

In this case, $\bar{\tau}^0$ stands for the preliminary failure stress, E for the transverse modulus of elasticity of the surrounding material, G_c for the energy release rate and l_e for the element edge length. N_e^0 indicates the number of cohesive elements per normal element. Since in this case the cohesive elements are the same size as the normal elements, the value 1 is used for N_e^0. According to the approach of Turon et al. [46], the value for $\bar{\tau}^0$ is only used as the failure stress T if it does not exceed the maximum failure stress τ^0.

$$T = min\left\{\tau^0, \bar{\tau}^0\right\} \tag{4.3}$$

Compared to the previous analyses, the simulation model has to be adapted slightly so that the ILM can be integrated. Depending on which ILM is used, the model is adapted accordingly. As no additional elements are added for cohesive contact, the adaptation is simpler there. The common nodes of elements of neighbouring layers are separated.

These duplicate nodes mean that the elements retain their original shape but have their own nodes and are no longer connected to each other via common nodes. Instead of connecting via common nodes, the connection is established with the surface-to-surface contact.

For the ILM with cohesive elements, the thickness of the normal elements is reduced slightly. The cohesive elements are inserted into the resulting gaps between the layers. In this case, a thickness of the cohesive elements t_{ce} of 0.01 mm was selected. This value comes from a study of micrographs of fibre composite materials that was made available internally. Since the inter-laminar behaviour is modelled within the cohesive elements, these elements can be connected to the normal elements via common nodes. No additional contact is required to connect the elements. If the maximum loads in the cohesive element are exceeded, this element is deleted and ignored for all further calculation steps. For this reason, a so-called eroding contact is required for this modelling method. This contact becomes active as soon as a cohesive element is deleted and describes the contact between the normal elements that are now directly adjacent to each other. The eroding contact is not required when modelling with a cohesive contact, as the behaviour after the load limit is exceeded is already defined in the contact. In the evaluation, it must be considered that the eroding contact significantly extends the calculation time. In this case, around 40 % to 45 % of the total computing time is required for the eroding contact.

4.6.2 Validate Model

For the validation of the simulation models, a model with ILMs is set up that is as similar as possible to the models from the basic investigation. The results of these simulations are compared with a representative result from the basic investigation (configuration 75). Four models were used for the validation, covering both ILM variants and solid and tshell elements (see Table 4.9).

Table 4.9: Configurations for Validation of Simulation Models with ILMs

Element Type	Number of Elements (thickness)	Integration Points	Element Size (rel)
solid	8	1	3.0
solid	8	1	3.0
tshell	8	4	3.0
tshell	8	4	3.0

The same model was used for the geometry as for the basic investigation, whereby the described adjustments were used for the ILMs. In addition, the axial load had to be adapted. Due to the ILMs, the axial load cannot be applied directly as a load, as this would lead to immediate failure and high deformations in the hoop layers. To avoid this problem, the axial load is applied as a predefined displacement. To do this, the final displacement at the right end of the tube ($x = 700mm$) is determined in the reference model (configuration 75) and applied to the models with ILMs as a boundary condition.

Figure 4.28 shows the comparison of the axial stress between configuration 75 (red line) and the four models with ILMs (marker).

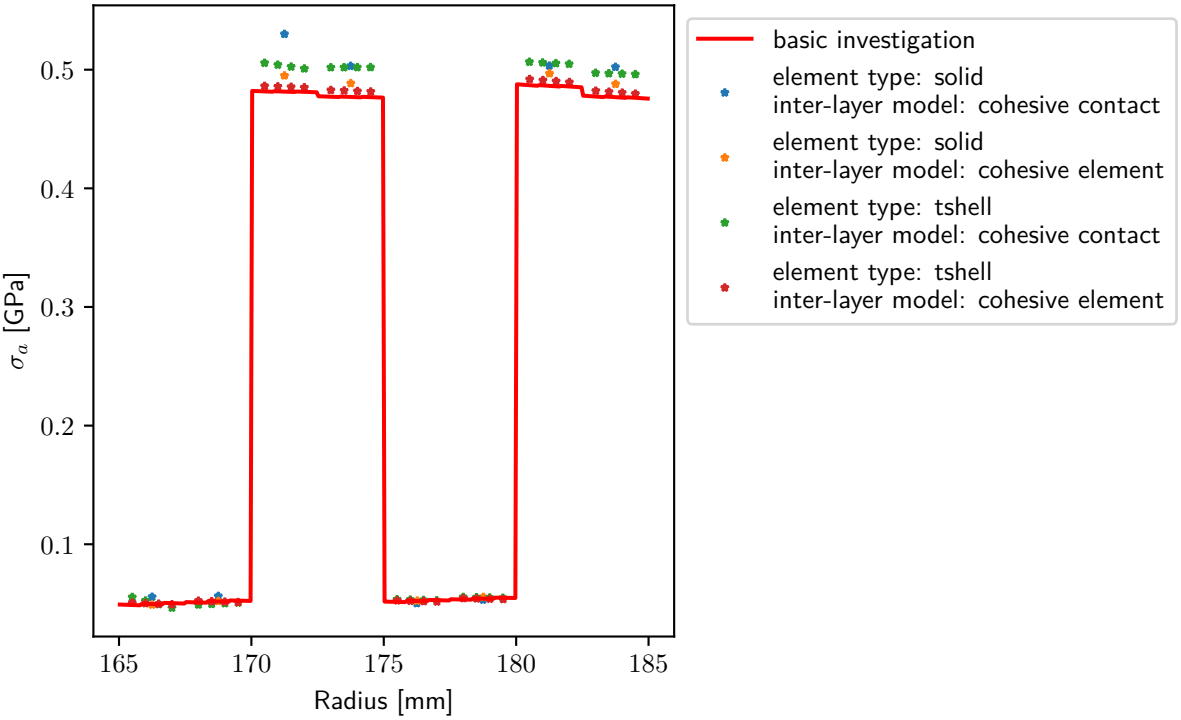

Figure 4.28: Axial stress comparison

The diagram shows that the models with cohesive elements (orange and red markers) are in good agreement with the reference values (deviations <5 %). The deviations of the results with cohesive contacts (blue and green markers) are larger, but at <10 % they are within an acceptable range. As the radial and tangential stresses have smaller deviations than the axial stresses, they are only shown in Appendix E. The comparison of the four models with the reference model has shown that the models with cohesive elements provide a good agreement of the results. The models with cohesive contacts lead to slightly larger deviations but are accurate enough to be considered in this investigation.

4.6.3 Simulation Model

A new load case is used for this investigation. In contrast to the previous investigations, the focus of the load case is not on the internal pressure, but on the impactor. In the first part of the investigation, the tube is only loaded by the impactor. Due to the larger deformation without internal pressure the behaviour of the ILM is more relevant in this load case. In the second load case, selected configurations are loaded with internal pressure and impactor to be able to compare both load cases. The terms impactor and indenter are used in the following. In the context of this thesis, both mean the same thing and refer to the geometry shown in Figure 4.29.

Figure 4.29 shows the geometry and the contact point of the impactor. A cuboid with strongly rounded edges on the contact surface is used for the impactor geometry. The flat area in the centre avoids a point load on initial contact with the tube and establishes contact over a large area as quickly as possible. This avoids problems in the simulation caused by very large loads at small contact surfaces. The rounding also helps, as a concentration of force could occur at the edge.

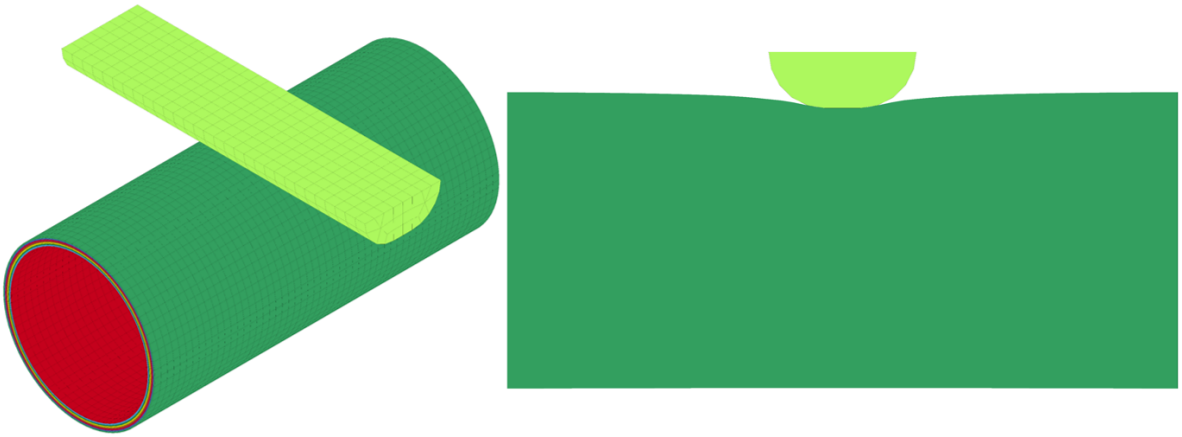

Figure 4.29: Isometric view of tube with impactor (left) and side view of impactor and deformed tube (right)

The impactor is modelled as a rigid body so that the simulation does not become too complex as the impactor also deforms. In addition, a rigid impactor can be modelled well in an experimental test by using a solid metal body. In the simulation, the impactor is forced into the tube with a prescribed displacement of 20 mm (see Figure 4.29).

As the load cases in this investigation are not rotationally symmetrical, the support boundary conditions must also be adapted. For this investigation, the displacements of all nodes at the ends of the tube are blocked in all spatial directions. This boundary condition is chosen because it represents the fastening of the tank with enclosing clamps and the additional stability provided by the domes at the tank ends reasonably well. More realistic boundary conditions would be possible with more complex investigations and modelling. This additional effort would lead to more realistic results but would not necessarily enable a better comparison of the ILMs, which is why the simplified support is chosen.

The contact definitions and, in the case of the model with the cohesive elements, the additional elements increase the computational effort of the simulations considerably. For this reason, the length of the tube is reduced to 60 %. As with the boundary conditions, the change means that the results are less consistent with the original model. However, the change is unlikely to have a major impact on the comparison of the ILMs. By reducing the simulation time, more configurations can be analysed.

Table 4.10 shows the parameter combinations used. Each of the combinations listed is simulated once with cohesive contacts and once with cohesive elements. This results in 28 configurations from the 14 combinations shown. The complete list is shown in Appendix A.

Table 4.10: Parameter Combinations of Inter-Layer Investigation

Element Type	Number of Elements (thickness)	Integration Points	Element Size (rel)	Load Case
solid	8	1	1.5	impactor
solid	8	1	3.0	impactor
solid	8	1	6.0	impactor
solid	16	1	3.0	impactor
tshell	4	2	3.0	impactor
tshell	4	4	3.0	impactor
tshell	8	2	3.0	impactor
tshell	8	4	1.5	impactor
tshell	8	4	3.0	impactor
tshell	8	4	6.0	impactor
solid	8	1	1.5	load + impactor
solid	8	1	1.5	gas + impactor
tshell	8	4	1.5	load + impactor
tshell	8	4	1.5	gas + impactor

In the configurations with internal pressure, configurations with both variants of the pressure, as load and as a gas (CV method), are simulated. This comparison only serves as a check. It is intended to verify that the results from the previous investigation can be transferred to this model with the ILMs.

The configuration with 16 solid elements in the thickness direction differs from all other configurations as it is the only one with more elements than composite layers. Two ways can be used to model this configuration. The ILMs can be inserted between each element layer or only where elements with different composite layers meet. Both variants are shown in Figure 4.30. To ensure that the cohesive elements are recognisable, only the top and bottom elements of the normal elements are shown. A brief preliminary investigation has shown that the results of both variants differ significantly from each other. The variant with the ILMs at the composite layer borders delivers results that match the results of the other configurations from Table 4.10 better. For this reason, this variant is used for the analysis of the results.

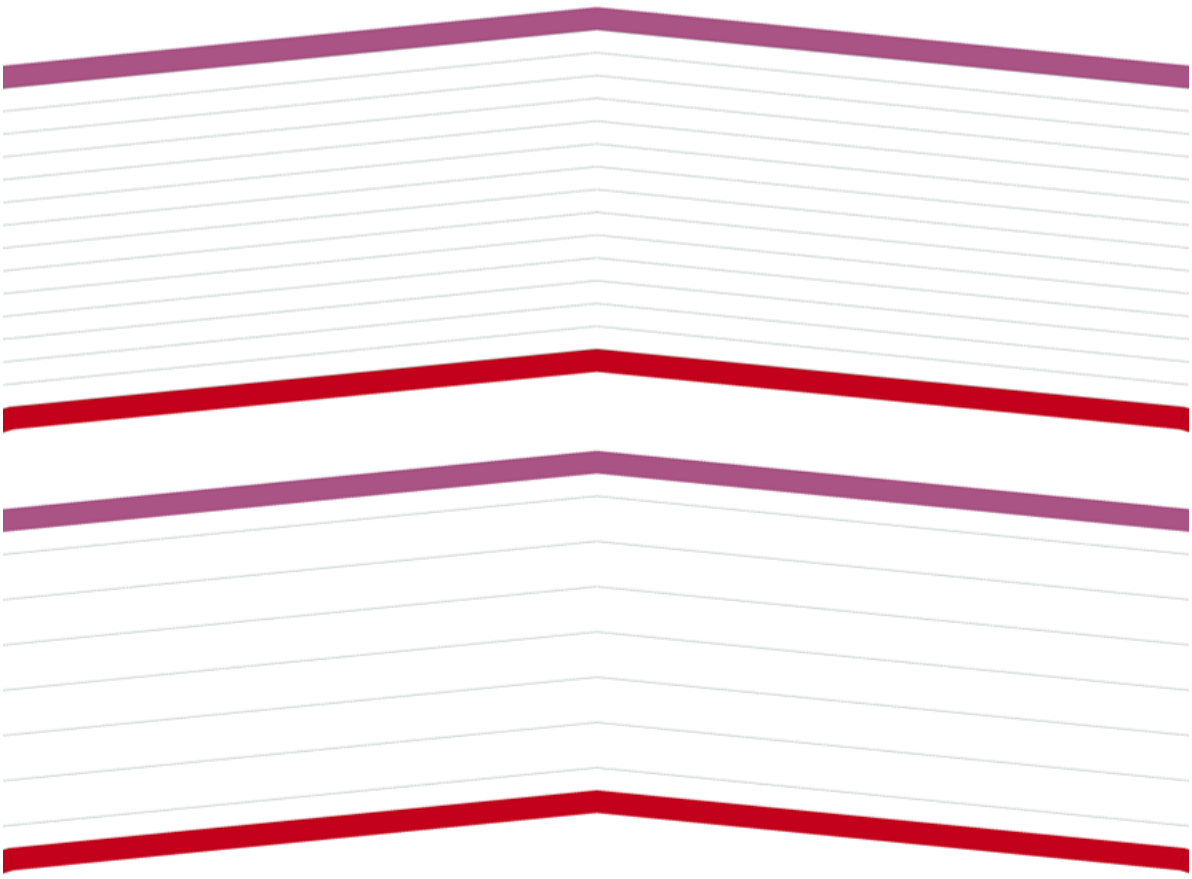

Figure 4.30: ILM for each element layer (top) and ILM for each composite layer (bottom)

4.6.4 Simulation Results

The impact load case means that the model does not behave in the same way everywhere over the length and circumference. The deformation and the damage is localized. As a result, the evaluation of the stresses in the centre of the model ($x = 0mm$) is not meaningful. In addition, the delamination failure cannot be ideally analysed with the previous methods. Instead, the reaction force on the impactor and the energies in the tube are used for this evaluation. These variables offer the possibility of analysing the behaviour of the individual models quickly and comparably. For a detailed assessment of the simulation results, the failure behaviour (fibre failure and delamination) and the stress distribution must be examined graphically. As this is not possible for many models, this analysis is only carried out on a few selected models. In the first step, the reaction forces of the models without internal pressure are analysed and compared with each other. The reaction forces under combined load (internal pressure and impact) are then analysed. In the third step, the energies of the models without internal pressure are analysed. Finally, the results of the most promising models are analysed graphically. In comparison to the previous studies, no reference values are available with which the results can be assessed. For this reason, an assessment is made as to whether the results are qualitatively meaningful and meet expectations, and a comparison is made as to how the results relate to each other in terms of quality and quantity.

Reaction force

Figure 4.31 shows the reaction force between the impactor and the tube as a function of the displacement of the impactor. The curves in the diagram all have a similar shape. The first part of the diagram shows a short phase in which the impactor bridges a narrow gap to the tube. In this part, the reaction force is zero as no contact is made. After that the curves start with a linear gradient at the beginning and then change into a flattened, slightly fluctuating curve. The linear part of the curves represents the linear elastic part of the load case. As soon as the failure limit of the first cohesive elements or the first contacts is reached, the elements are deleted, and the cohesive contacts are converted into frictional contacts. This leads to a sudden change in the structure, resulting in a jump in the curves in the diagram. The more elements or contacts fail at once, the greater the jump. Failure in the ILM leads to a lower stiffness in the tube, which means that the reaction force no longer increases as much, and a flattened curve is created.

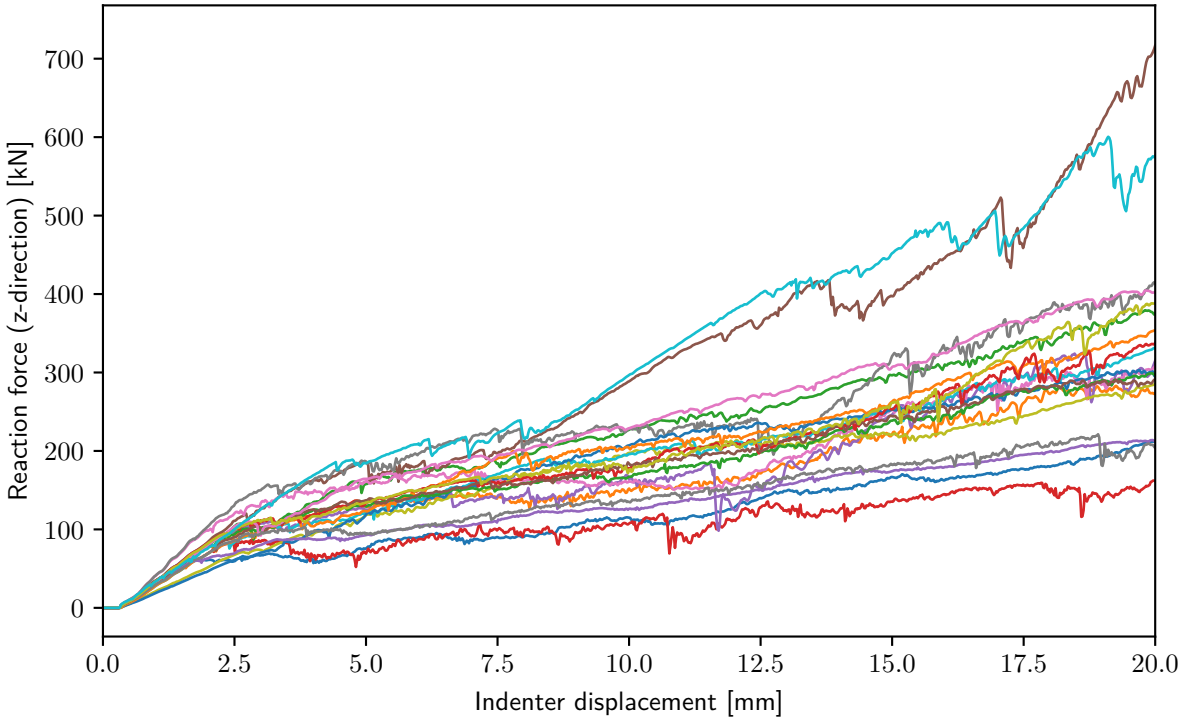

Figure 4.31: Reaction force on indenter (all simulations of inter-layer investigation)

The curves can be roughly divided into three groups, especially for the larger displacements (from 15 mm). The first group consists of the two curves with the highest reaction forces. The second group is formed by the four curves with the lowest reaction forces and the third group comprises the centre block with all other curves. To illustrate that the element size has the greatest influence on the division into these three groups, the curves in Figure 4.32 are coloured according to the corresponding element size.

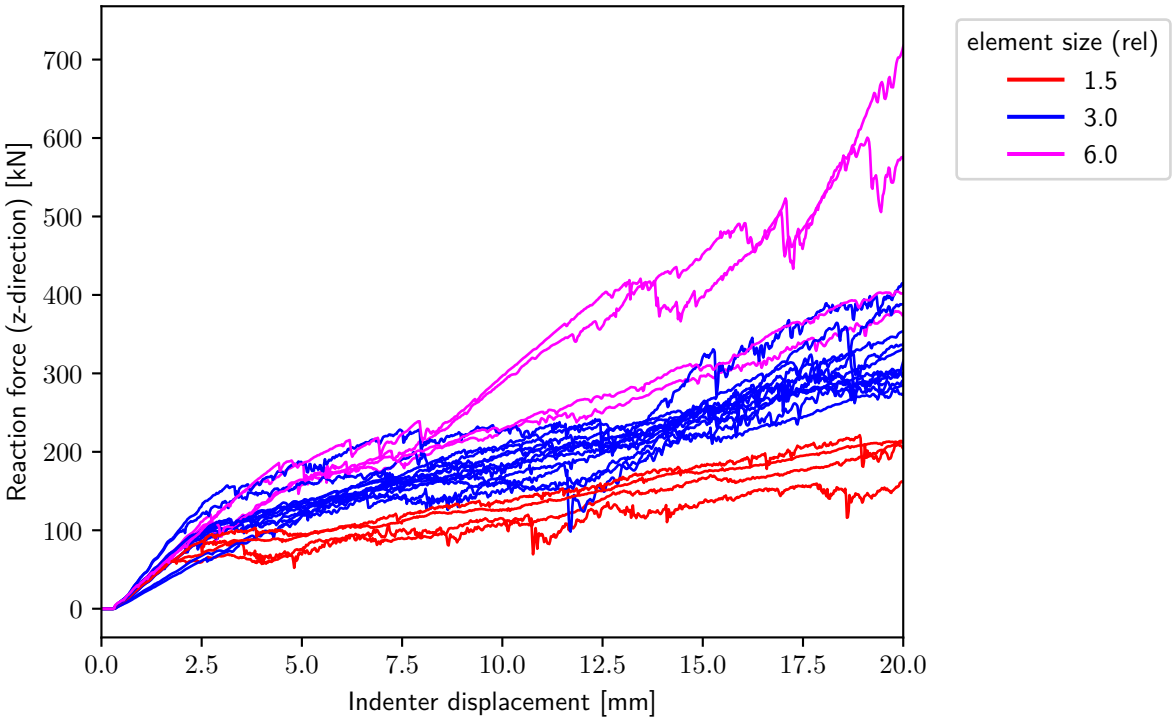

Figure 4.32: Reaction force on indenter (coloured by relative element size)

It can be seen directly that models with a finer mesh (smaller element size) lead to lower reaction forces. The opposite is true for models with a coarser mesh. An overlap can be recognised between the configurations with a relative element size of 6.0 and the configurations with 3.0. This overlap can be explained by colouring the curves based on the ILM used (Figure 4.33).

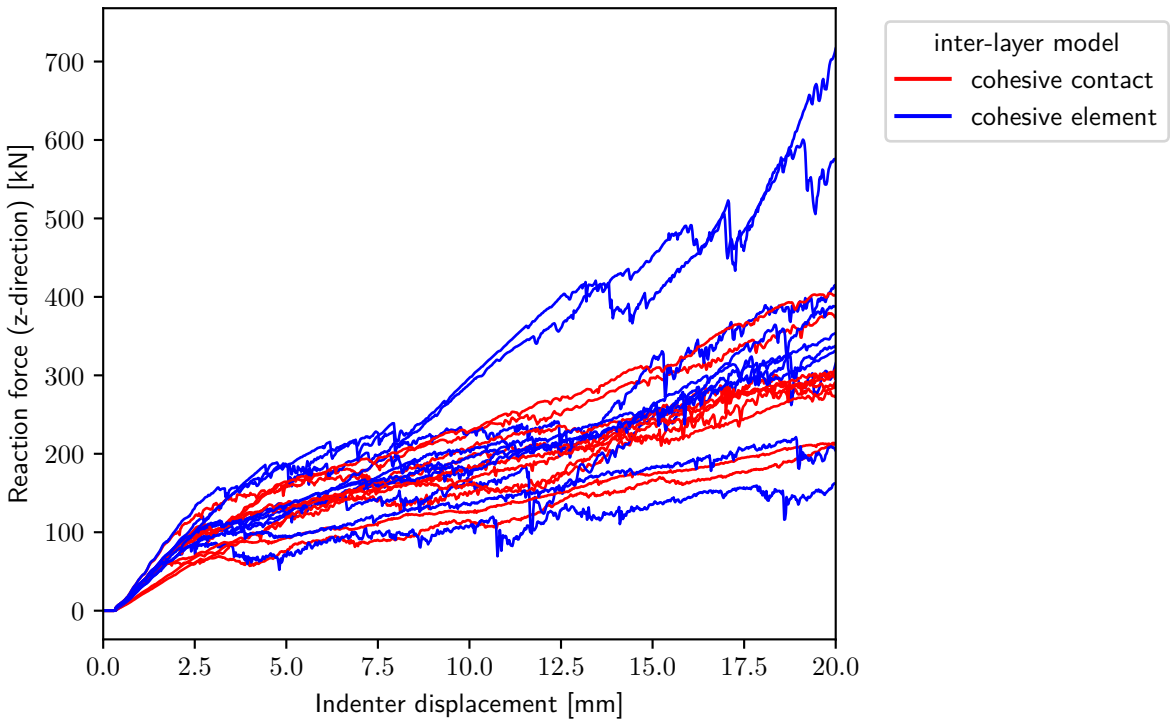

Figure 4.33: Reaction force on indenter (coloured by inter-layer model)

This diagram shows that the reaction forces of the majority of the cohesive contacts are lower than those of cohesive elements in the case of strong indentation (impactor displacement >15 mm). The larger the elements, the stronger the effect. The deviation is greatest for the models with coarse elements and decreases for the models with element size 3.0. A slight reversal of the effect is visible in the models with fine mesh. There, the cohesive elements have slightly lower reaction forces. In summary, these three diagrams show that the element size has a strong influence on the reaction force and the ILM has a recognisable but weaker influence. The third parameter that was varied is the element type. This has no recognisable influence on the reaction force (see Appendix E).

Due to the geometric load application by the impactor and the cylindrical geometry of the tube, an additional effect has an influence on the reaction force. The polygonal approximation of the round geometry with the mesh means that the impactor hits first an edge or the surface of an element. In the models used here, the impactor hits an element edge with its centre (see Figure 4.34).

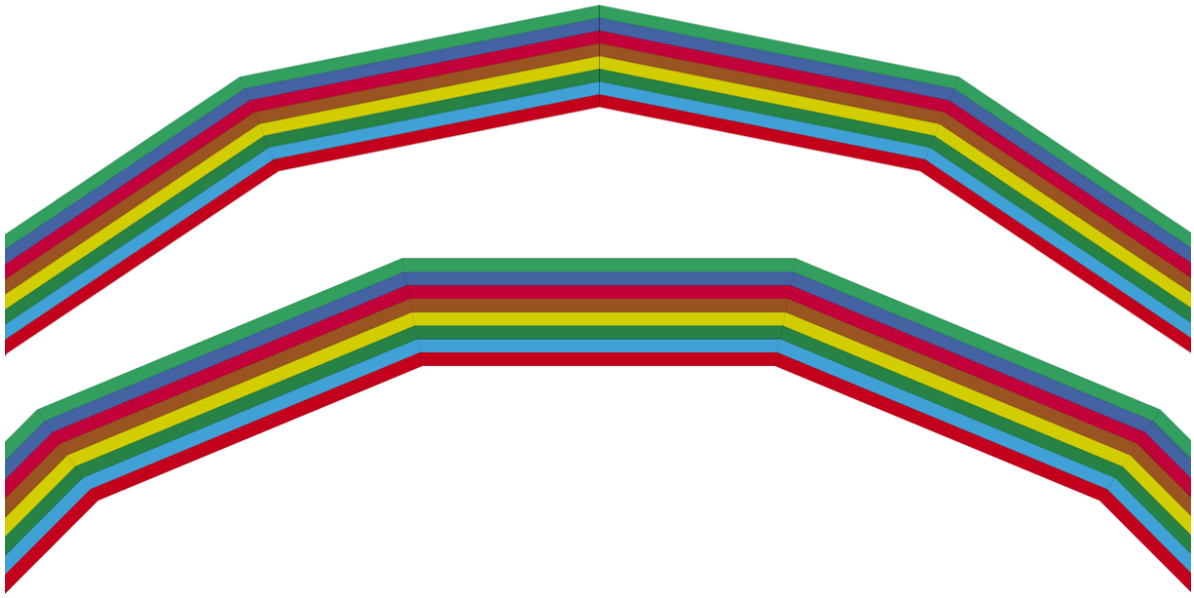

Figure 4.34: Comparison of standard mesh (0°) at the top and rotated mesh (11.15°) at the bottom

As a result, the geometry can appear stiffer than it actually is, particularly in the case of coarsely meshed models. The finer the model, the weaker the effect, as the cylindrical geometry is better approximated. Figure 4.35 shows an investigation in which the model was rotated by 11.15° (see Figure 4.34). As a result, the impactor hits the element surface instead of the element edge in the coarse model.

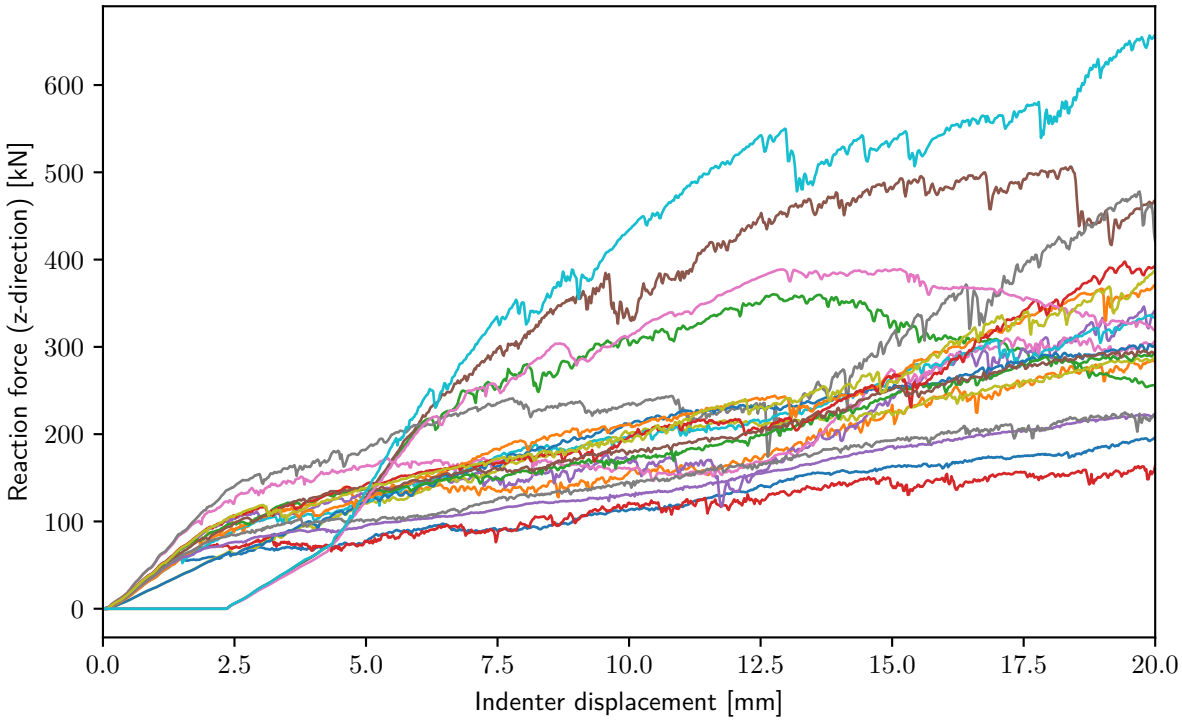

Figure 4.35: Reaction force on indenter (models rotated by 11.15°)

The diagram shows that the curves of the coarse models (upper light blue, brown, pink and green) in particular have changed. The changes are especially noticeable at the beginning and end of the simulation. At the beginning, the distance travelled by the impactor before it hits the tube is significantly greater. At the end, the lower stiffness results in some cases in significantly lower reaction forces compared to the model without rotation (Figure 4.31). These changes cannot be recognised in the models with a fine mesh. The point of impact does not change significantly and the curves reach values between 100 kN and 200 kN at the end, which is comparable to Figure 4.31.

Analysing the reaction forces shows that the model behaves differently depending on the element size and the ILM. However, without reference values, it is not possible to determine which reaction forces are closer to reality.

After analysing the models without internal pressure, the next diagram shows the reaction force under combined load (internal pressure and impact) (Figure 4.36). The curves differ significantly compared to the models with pure impact loading. The internal pressure significantly stabilises the tank and therefore leads to significantly higher reaction forces at the same deformation. It can also be seen that the curves are almost linear and do not show any major fluctuations. This is an indication that material failure and delamination have significantly less significance on the structural stability.

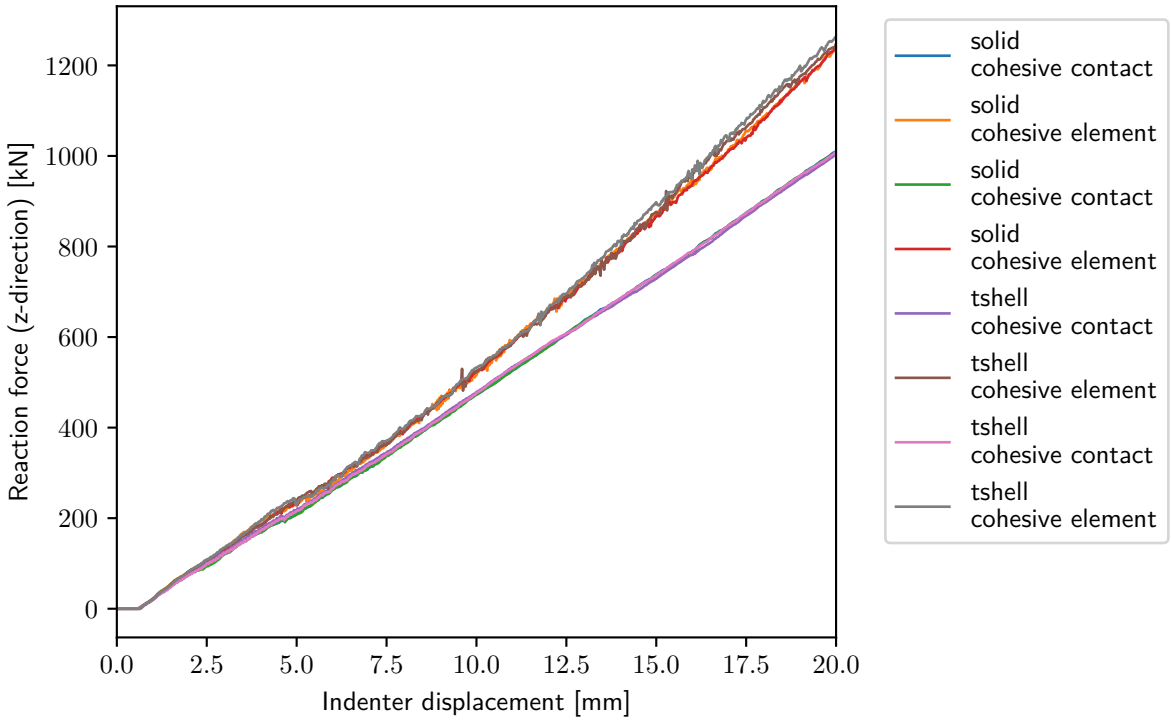

Figure 4.36: Reaction force on indenter (load case: pressure + impact)

The models analysed are divided into two groups in the diagram, which become increasingly clear as the indentation increases. The groups can be distinguished on the basis of the ILM. Models with cohesive elements provide 20 % to 25 % higher reaction forces, compared to the reaction forces of models with cohesive contacts. The element type and the type of internal pressure (direct load or pressurized gas) have no effect on the results. Two hypotheses are put forward as to what causes this deviation. Firstly, the analysis of the energies indicates that a problem occurs in the simulation with the cohesive contacts (see below). Secondly, it could be that the cohesive elements fail later than the cohesive contacts. As a result, there would be less delamination of the elements, and the stiffness would be greater. It was not possible to verify this reason within this thesis.

Energies

The next pages compare the different energies of the models without internal pressure. The following energies are analysed: total energy, internal energy, eroded internal energy, external work, sliding interface (SI) energy and hourglass energy. All energies are shown in a diagram for each model. Diagrams with a blue frame represent models with solid elements and diagrams with a red frame represent tshell elements. The diagrams for the models with cohesive contacts are shown in Figure 4.37 and the diagrams for the models with cohesive elements are shown in Figure 4.38. The model to which the diagram belongs is specified in each diagram. Here, el size stands for the element size and nel for the number of elements over the wall thickness. In the diagrams for models with tshell elements, the number of integration points per element (nip) is also specified.

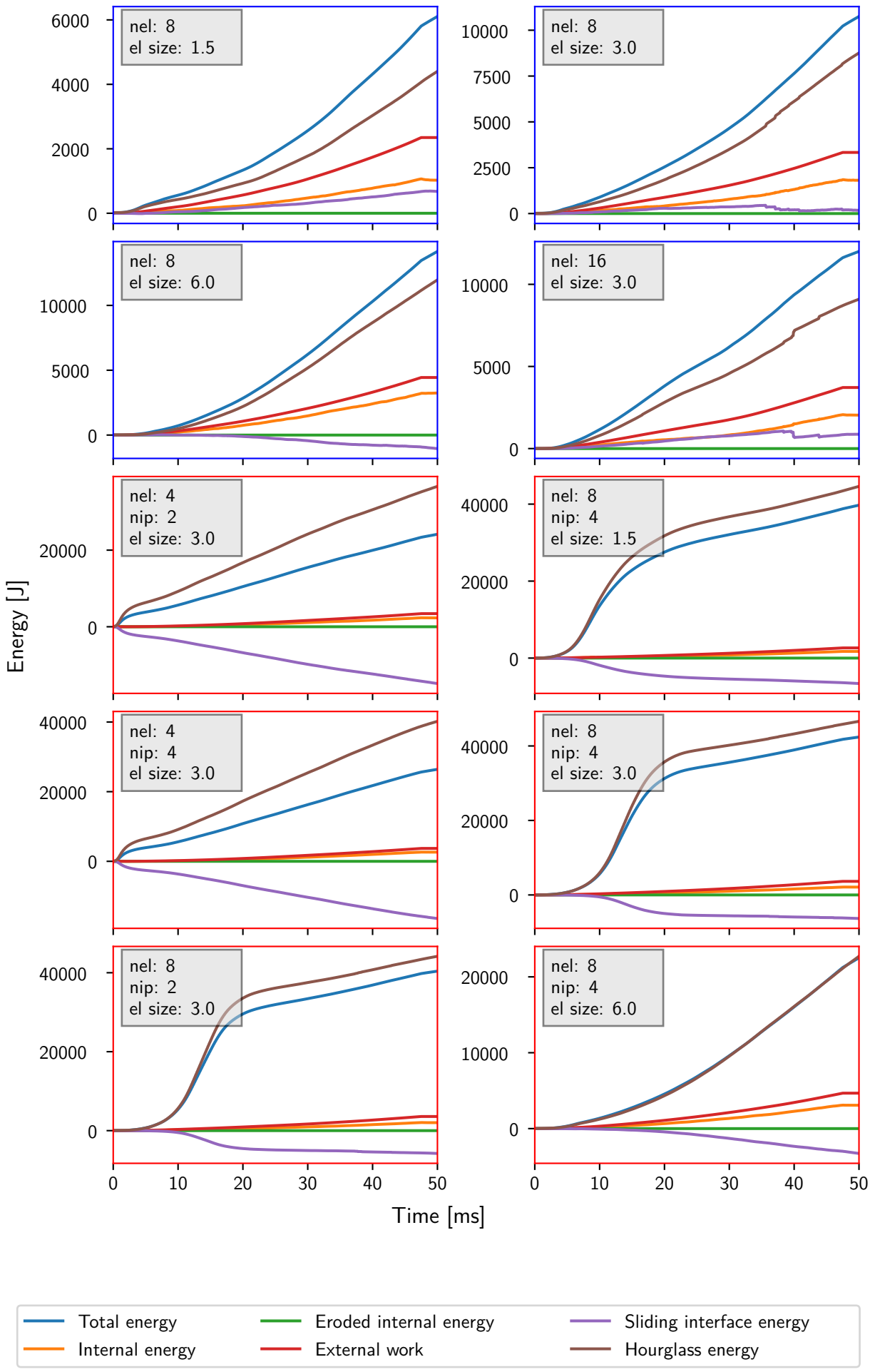

Figure 4.37: Energies (cohesive contact)

To be able to evaluate the energy curves, it is first necessary to define what a diagram of a good simulation would look like. A diagram with good energy curves has the following properties. By definition, all energies are positive. The energy equilibrium is fulfilled (equation 2.3). Since the initial kinetic and internal energies are zero, this means that $E_{total} = W_{ext}$ applies. The hourglass energy is less than 10 % of the internal energy. The SI energy increases with the simulation time, as delamination areas are to be expected at which frictional energy is released. Jumps are permissible at this energy, as they represent the friction of sudden slippage of adjacent layers. It is to be expected that the internal energy forms the largest part of the total energy. The eroded internal energy should behave differently depending on the ILM. No eroded energy is expected for cohesive contacts, as no elements get eroded there, only the contact breaks. The cohesive elements are erased (eroded) on failure, whereby in these simulations the internal energy stored on failure is shown in the corresponding curve.

Compared to these characteristics of a diagram of a good simulation, the results of the simulations with cohesive contacts (4.37) show a major issue. All diagrams show a very high hourglass energy. The hourglass energy exceeds the internal energy by a multiple in all cases. In the models with solid elements, it forms the largest part of the total energy and in the models with tshell elements it even exceeds the total energy.

Another indication of poor-quality simulation results are the negative SI energies. They have negative values, especially in the models with tshell elements. Since the SI energy is positive by definition (cf. Section 2.2.5), this would mean that energy is added to the system through friction. As this is not physically possible, an issue in the simulation is likely. The qualitatively similar curves of hourglass energy and SI energy could indicate that the negative SI energies are caused by hourglassing.

The third important property is that the energy equilibrium is also not fulfilled. In all cases, the total energy is significantly greater than the external work. Since the hourglass energy forms part of the total energy, it is likely that hourglassing is the reason for this imbalance.

To summarise, all models with cohesive contacts deliver poor quality results. The reason for this is the strong hourglassing effect. An adjustment of the hourglass control card or the selection of a different element formulation (e.g. elform 7) could solve the problem (cf. Section 2.2.5) and provide good quality simulation results with cohesive contacts.

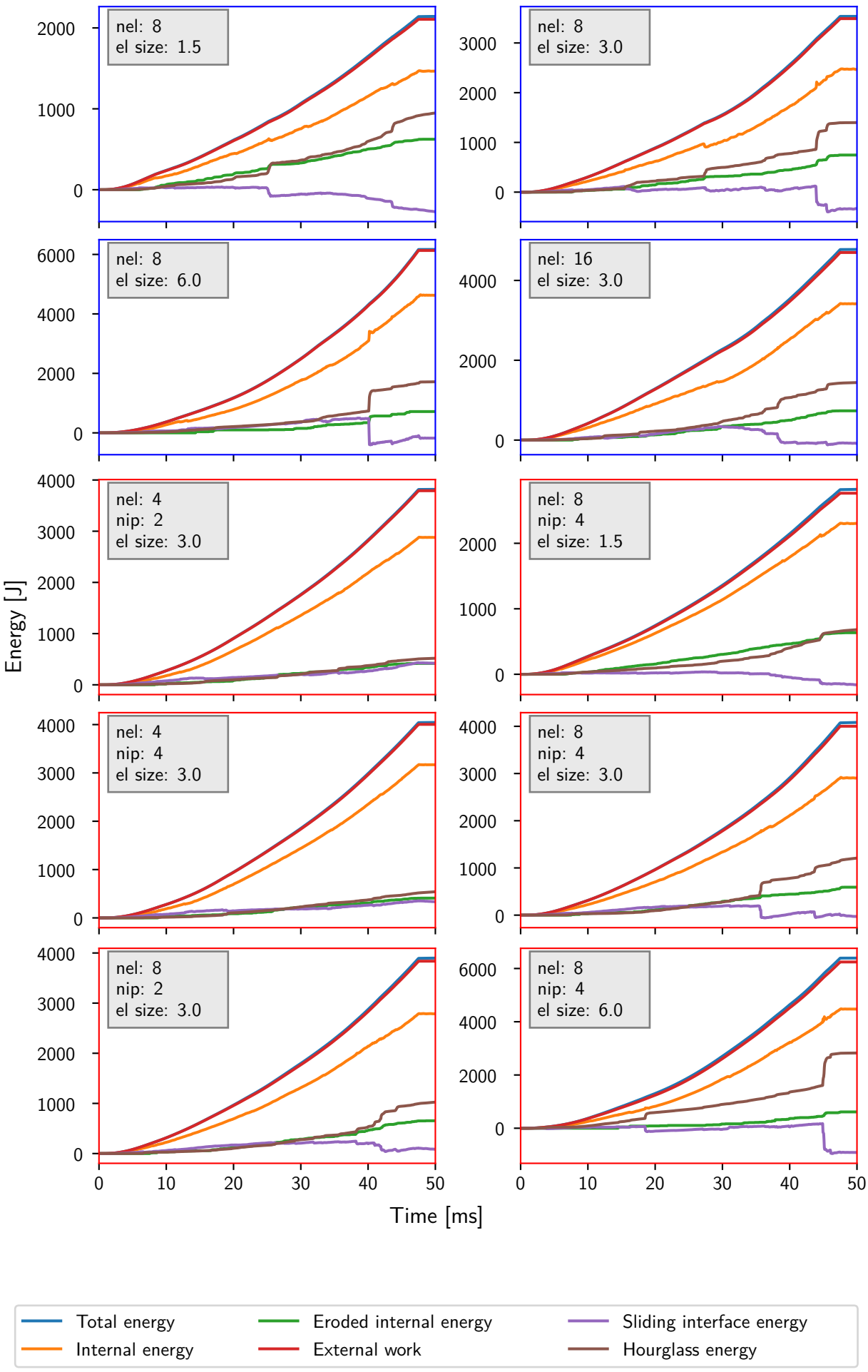

Figure 4.38: Energies (cohesive elements)

Compared to the diagrams of the simulations with cohesive contacts, the diagrams of the simulations with cohesive elements match the characteristics of good simulation results much better. In all diagrams in Figure 4.38, total energy and external work are close to each other, which corresponds to a good fulfilment of the energy equilibrium.

The internal energy has the largest share of the total energy in all cases. This also matches the desired properties. Significant differences can be recognized between the configurations in terms of hourglass energy. Only the configurations with four elements across the wall thickness fulfil the criterion with an hourglass energy of <10 % of the internal energy. For the other configurations, the criterion is not met and is clearly exceeded, e.g. in the diagrams top left (solid with nel: 8 and el size: 1.5) and bottom right (tshell with nel: 8, nip: 4 and el size: 6.0) with a proportion of over 50 %. The diagrams do not show a clear trend as to which parameters promote hourglassing. For the SI energy the same phenomenon can be recognised as for the cohesive contacts. An hourglass energy of more than 10 % of the internal energy leads to a qualitatively similar but negative course of the SI energy. The course of the eroded internal energy corresponds to the expectation. As the simulation time progresses, the energy slowly increases but remains significantly below the internal energy at all times.

In addition to the qualitative characteristics, an expected trend can also be recognised in the quantitative values. With a coarse mesh, more work is required for indentation than with a fine mesh. This tendency is related to the fact that the local deformation cannot be modelled in such detail for larger elements and therefore the deformed area is larger (see Figure 4.39). The figure shows the nodal displacement in the direction of indentation (z-direction) in a view from above. The same colour scale is used for both models. The black bars are intended to facilitate comparison.

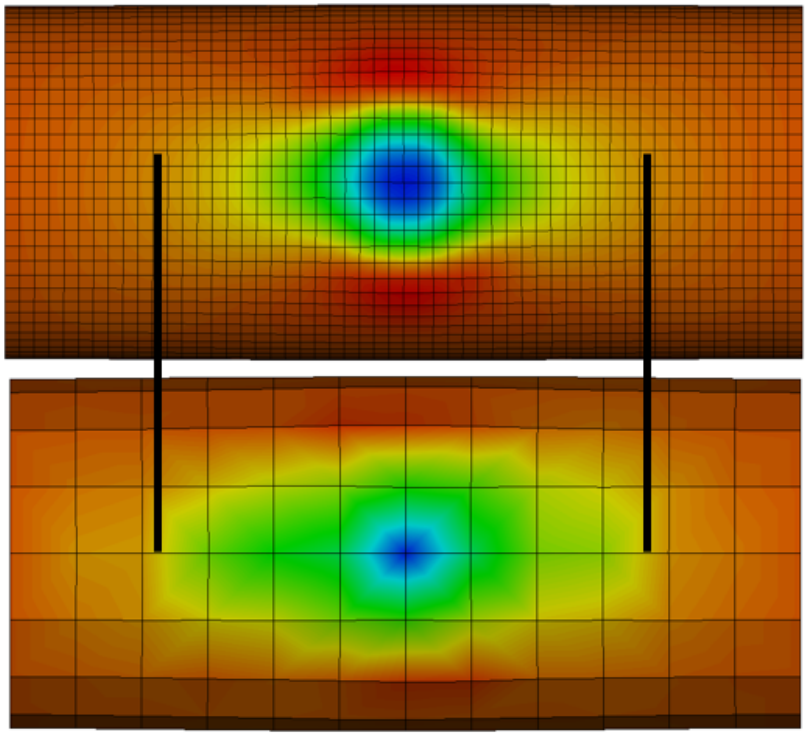

Figure 4.39: Comparison of area of effect of indentation for coarse and fine meshes

To summarise, the energies of the models with cohesive elements provide significantly better results than the models with cohesive contacts based on the defined characteristics. This is particularly true regarding the energy equilibrium and the proportion of internal energy in the total energy. For the hourglass energy, only the models with four elements across the wall thickness provide good results. Considering that it is possible to reduce the hourglass energy, for example by adapting the hourglass control algorithms or by changing the elform, the other models with cohesive elements are also within an acceptable range in terms of the energies. Therefore, all configurations with cohesive elements are considered for further investigations.

Graphical Evaluation

In the graphical evaluation of the results, the deformations and delaminations in the area of the impact are analysed. As the graphical evaluation is significantly more complex than a numerical evaluation, only four configurations are analysed. These configurations consist of two configurations each with solid and tshell elements. One configuration with a coarse mesh and one configuration with a fine mesh are shown for each element type. Due to the results from the evaluation of the energies, only configurations with cohesive elements are shown here. As a brief comparison, the deformation of a configuration with cohesive contacts is shown in Appendix E.

Firstly, the delaminations are compared. In the simulation, cohesive elements are deleted if they have failed. The deleted elements therefore represent delaminations. For the graphical representation, the results are inverted so that only the deleted elements are shown. The deleted elements are displayed from three perspectives. Top left is the isometric view, top right is the top view, and bottom is the front view.

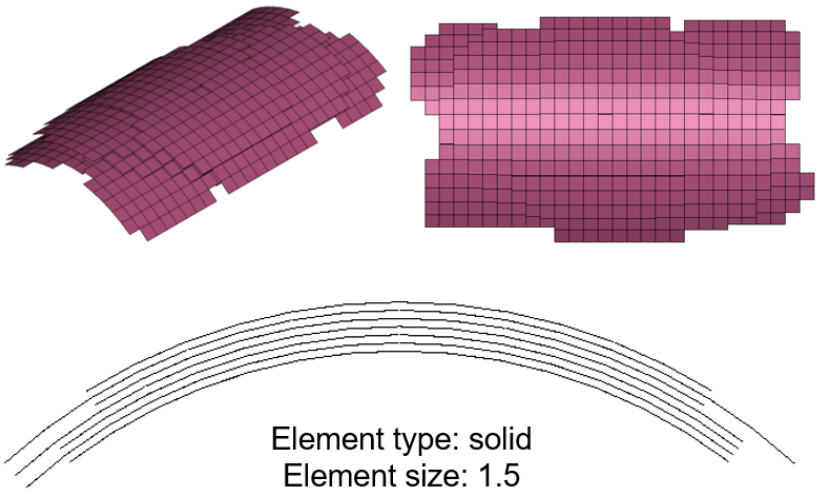

Figure 4.40: Deleted elements (element type: solid; element size: 1.5)

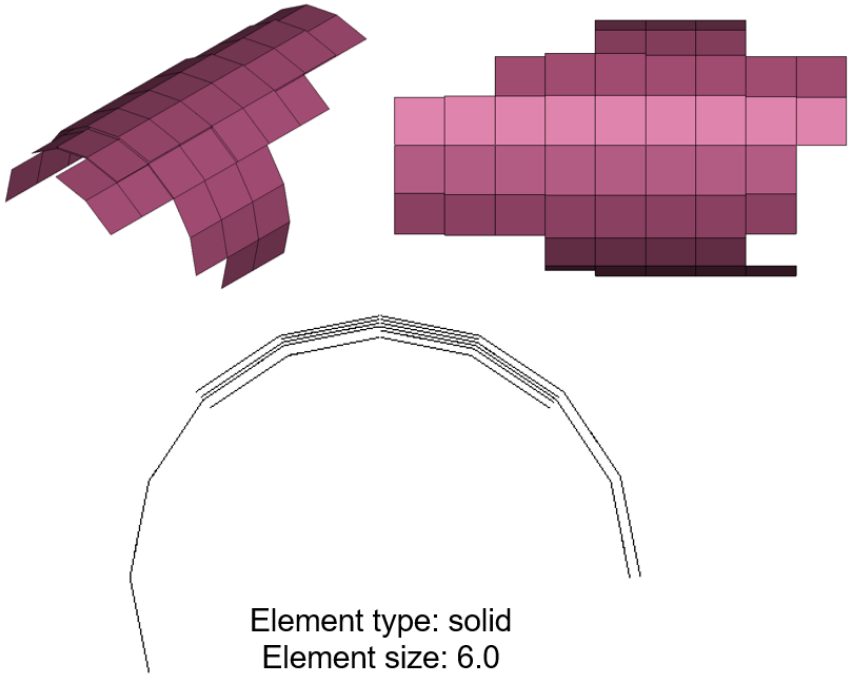

Figure 4.41: Deleted elements (element type: solid; element size: 6.0)

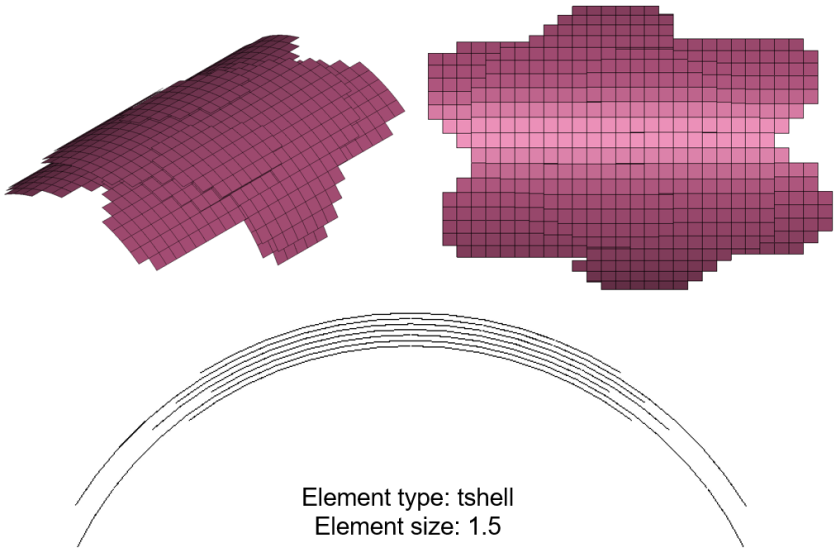

Figure 4.42: Deleted elements (element type: tshell; element size: 1.5)

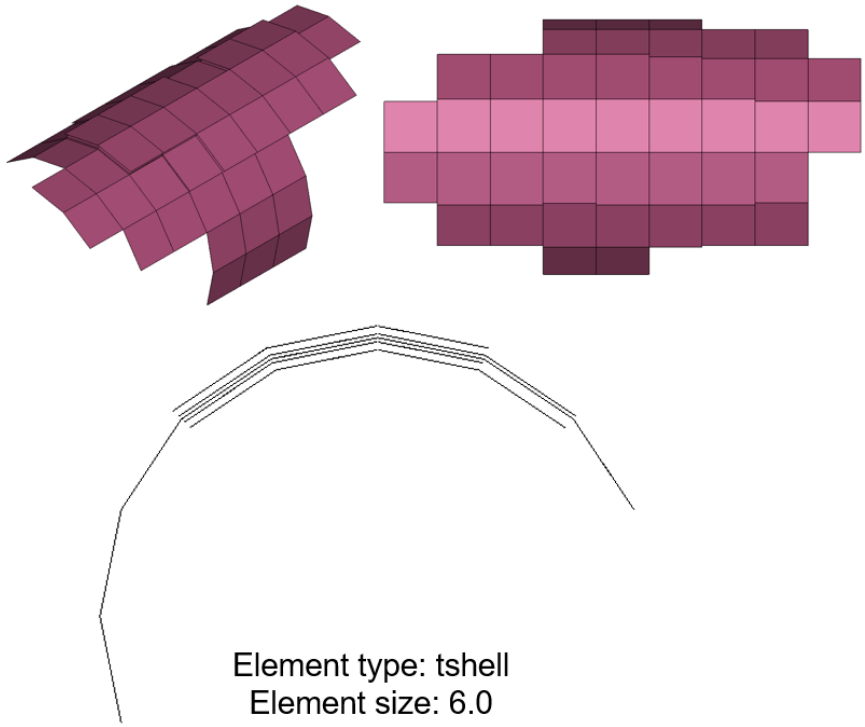

Figure 4.43: Deleted elements (element type: tshell; element size: 6.0)

When comparing the delaminations of the four configurations (Figure 4.40 to 4.43), clear differences between the results of different mesh sizes can be recognised, but only marginal differences between the results of different element types. The delaminations in the models with mesh size 6.0 are slightly larger in the direction of the axis of rotation than in the fine models. In addition, they widen by half the circumference in the circumferential direction, whereas in the fine models they barely extend beyond the impact area. In contrast, the delaminations in the fine models are distributed much more consistently across the wall thickness of the tank. In these models, the delaminations occur in the impact area between all layers, whereas in the coarse models no delaminations occur between some layers.

These results match the data from the diagrams of the numerical analyses. In the last section, it was established that the impact has a greater range of influence in the models with a coarse mesh. This larger range of influence is also reflected in the delaminations, which spread wider in models with a coarse mesh. In addition, the fact that not all layers across the thickness are delaminated in the coarse models could be a reason why the reaction force on the impactor is greater in these models. The reaction force is greater in models with fewer delaminations, as several bonded layers have a higher overall stiffness than the same layers with delaminations at the interfaces.

In the second part of the graphical analysis, the deformation at the point of impact is analysed. The deformations are shown as a section at the centre of the tank normal to the axis of rotation. The same configurations are displayed in the same order as the deleted elements. The green area in the upper part of the figures is the cross-section of the impactor. In Figures 4.44 and 4.47, one irregularity can be recognised in each visualisation of the section. These irregularities only arise from the graphical representation of the section and are not part of the simulation results. Accordingly, they are not considered in the evaluation.

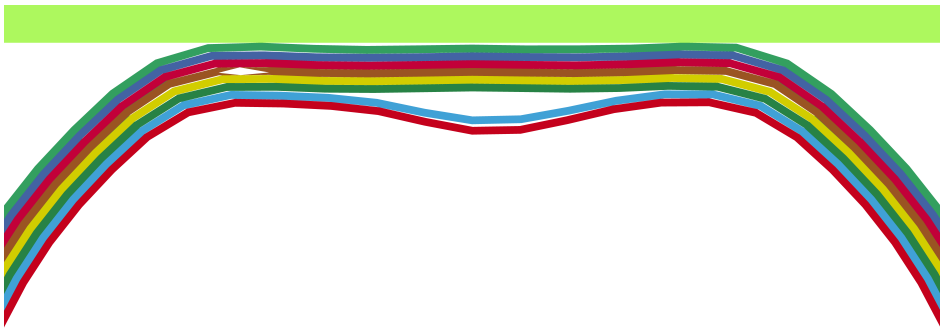

Figure 4.44: Cross section deformation (element type: solid; element size: 1.5)

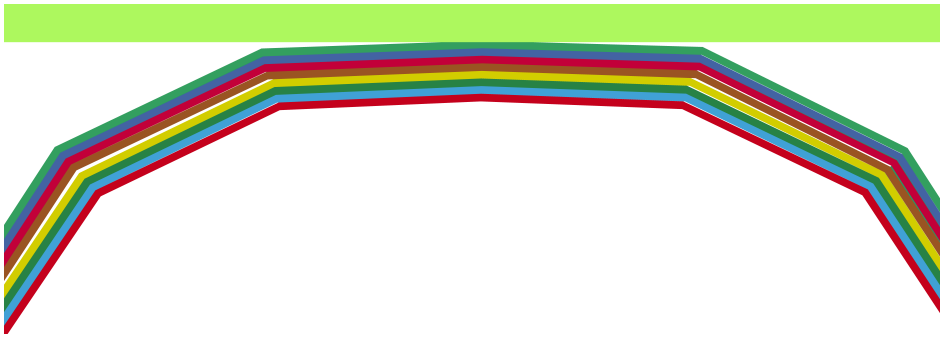

Figure 4.45: Cross section deformation (element type: solid; element size: 6.0)

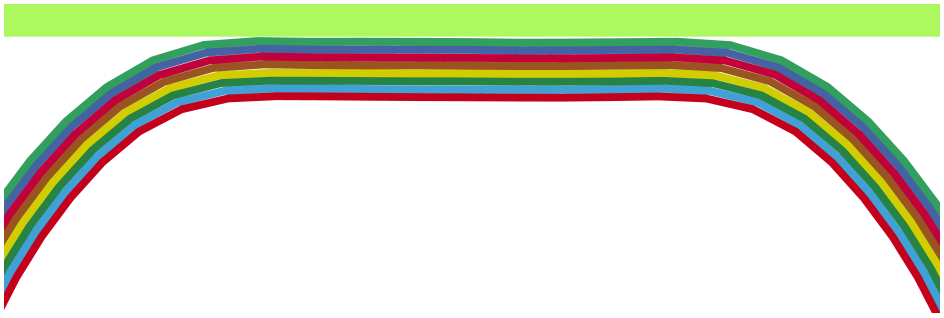

Figure 4.46: Cross section deformation (element type: tshell; element size: 1.5)

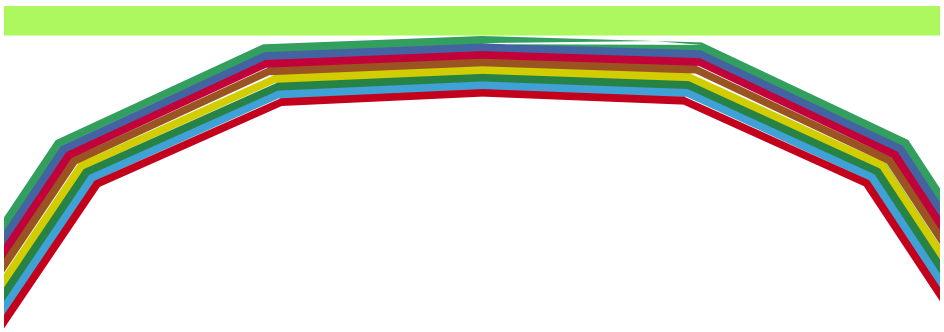

Figure 4.47: Cross section deformation (element type: tshell; element size: 6.0)

It can be seen from the images of the deformations (Figures 4.44 to 4.47) that the model with a fine mesh has a much more natural deformation. Natural deformation means that a round geometry is pressed flat in the centre and the curvature increases at the edges of the contact surface with the impactor.

In contrast, in the coarse model, only the centre node is pressed into the cylinder and the adjacent nodes deviate slightly outwards. The inaccurate approximation of the cylindrical geometry results in a different deformation pattern. In addition, the mesh is so coarse that with the deformation of 20 mm used here, only the centre nodes come into contact with the impactor. Figures 4.45 and 4.47 show a gap between the nodes next to the centre node and the impactor. This results in a concentrated line load instead of the surface load that occur in the fine model and is expected to occur in reality.

The detachment of the lowest layers and inward curvature in Figure 4.44 corresponds to realistic behaviour with large deformations of hollow cylindrical bodies. The compression creates a compressive stress in the inner area of the wall. If the deformation is large enough, the layers deflect downwards, which relieves them [42]. Whether the deformation is large enough to cause such behaviour or whether the deformation is more realistic without this detachment, as in Figure 4.46, cannot be determined with the available information.

The analysis of the deformation has shown no significant difference between models with cohesive elements and cohesive contacts. As an example of this, the deformation of a model with cohesive contacts is shown in Figure E.4 in Appendix E. The model on which this result is based corresponds to the model in Figure 4.44.

4.6.5 Result Evaluation

In the investigation of interlayer modelling in combination with impact loads, the simulation results were evaluated in three ways. In the first step, the reaction force on the impactor was compared, in the second step the energies were compared and in the third step the delaminations and deformations of selected configurations were graphically evaluated.

The analysis of the reaction force showed that the element size had the greatest effect on this result variable, while both ILMs and both element types produced approximately equal forces. The analysis of the energies showed that models with cohesive contacts led to very high hourglass energies and thus to an energy imbalance. The energies of models with cohesive elements show a slightly increased hourglass energy. It is significantly lower compared to the cohesive contacts and the cohesive elements fulfil the energy equilibrium well. For this reason, the cohesive elements are better suited as ILMs for this thesis than cohesive contacts. The graphical evaluation has shown that models with a coarse mesh cannot reproduce the deformation as realistically as models with a fine mesh. In the models with a fine mesh, both the deformation and the delamination look significantly more homogeneous and realistic.

In summary, the investigation of interlayer modelling has shown that a finer mesh with small elements is preferable for the element size despite the longer computing time. In addition, the cohesive elements are selected as the ILM. When analysing the number of elements over the wall thickness, the analysis of the energies showed that fewer elements are less susceptible to hourglassing. In terms of element type, both types produced roughly the same results. Both solid and tshell elements are suitable for modelling impact load cases with an inter-layer model.

4.7 Simulation Methodology for the Simulation of Hydrogen Tanks

In this section, the findings of the previous investigations are used to recommend a modelling method. In the selection process, it is considered that the stacking sequence of the specified tank model differs from the stacking sequence of the preliminary investigations.

4.7.1 Model Parameter Choice

The relevant findings from the previous investigations are used to select the combination of parameters to be used for the overall tank investigation. The following list presents all relevant findings from these investigations.

Basic investigation:

- Shell elements provide stress and deformation results with significantly greater deviations than solid and tshell elements. (Element type)
- A combination of several fibre layers with deviating fibre angles in one tshell elements leads to inaccurate stress results. (Number of elements)
- In explicit simulations, doubling the number of elements has a greater influence than doubling the number of integration points per element. (Number of elements and number of integration points per element)

Burst pressure:

- Solid and tshell elements provide approximately equally good results. (Element type)

Gas model:

- Modelling the internal pressure as a gas using the control volume method (CV method) produces similarly good results as modelling the internal pressure as a load. (Internal pressure model)
- The additional computational effort is negligible. (Internal pressure model)

Inter-layer model:

- The mesh with a size of 1.5 (relative to the tank diameter) represents the deformation during impact best. (Element size)
- Models with cohesive contacts lead to strong hourglassing, which is why cohesive elements are more suitable. (Inter-layer model)
- The use of contacts (eroding contact and contact with impactor) makes the use of the implicit solver impractical. (Solver)

Based on these findings, the parameter combination shown in Table 4.11 is selected as the most promising configuration.

Table 4.11: Selected parameter combination

Parameter	Value
Element type	tshell
Number of elements (radial)	4 (one per angle-ply sublaminate)
Integration points per element	2 (two per angle-ply sublaminate)
Solver	Explicit
Element size (rel)	1.5
Internal pressure model	Gas (CV)
Inter-layer model	Cohesive elements

As tshell and solid elements produced roughly the same results with the fine mesh, a variant with eight solid elements in the thickness direction would also be possible. This variant was not chosen as the simulation time is slightly longer.

4.7.2 Simulation Model

In contrast to the investigations in the previous chapters, the tank geometry is not simplified to a tube for this investigation. Instead, the composite part of the tank, which consists of the cylindrical centre section and the domes at both ends, is modelled in its entirety (see Figure 4.48). Only the fittings that close the two remaining openings and the liner on the inside of the tank structure, which prevents the gas from leaking, are not modelled.

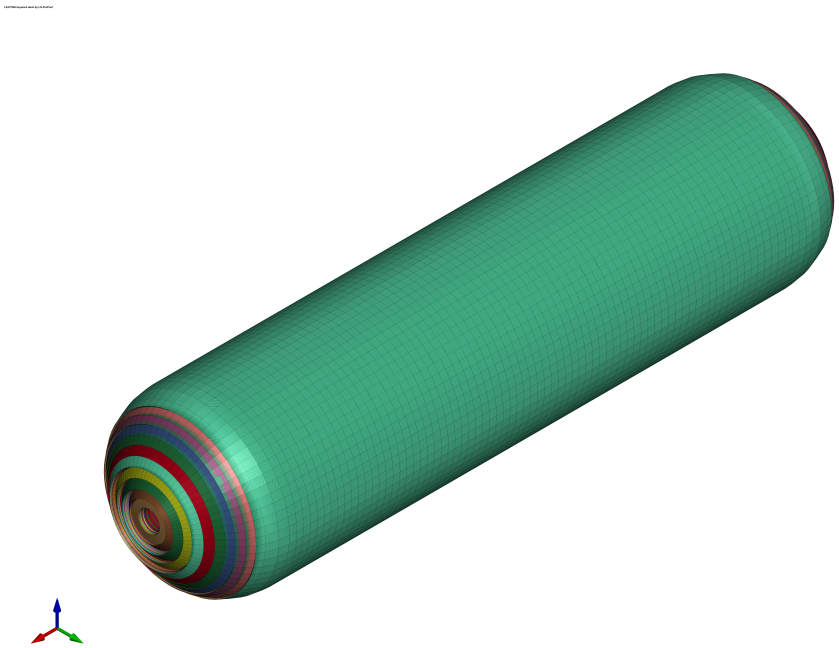

Figure 4.48: Tank geometry

Geometry and Stacking Sequence

The geometry and stacking sequence of the tank originate from an optimisation for a high-pressure hydrogen tank (cf. Chapter 1). Compared to the tube, the internal diameter of the tank remains the same at $d = 330mm$ and the external diameter increases only slightly from $D = 370mm$ to $D = 373.5mm$. The difference in the wall thickness of the tank was created during simplification. The wall thickness for the tube was rounded from 21.75 mm to 20 mm to make it easier to divide by the eight layers. The length of the tank is $L = 1400mm$ as with the tube, but the dome areas of the tank are included in this length, which means that the cylindrical part of the tank is shorter (see Figure 4.49). In the figure, the tank appears slightly longer. However, the additional length only corresponds to the wall thickness at the ends. In terms of the inner contour, both models are the same length.

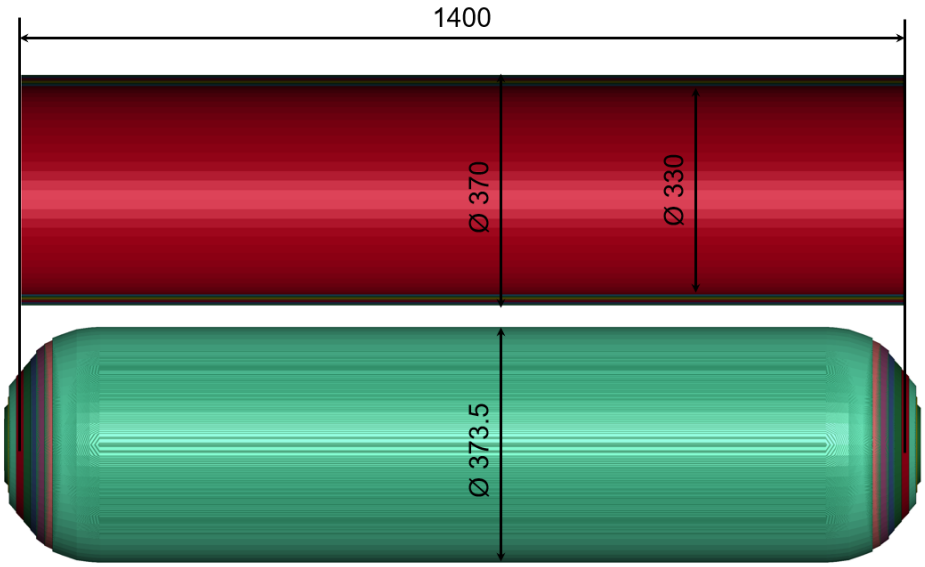

Figure 4.49: Tank geometry comparison

For the stacking sequence, the fibre angles shown in Figure 4.50 are used in the cylindrical part. The exact stacking sequence is given in Appendix F. The proportions of the layer angles correspond approximately to the distribution in the simplified model. There, 25 % of the layers have an angle of <20°, a further 25 % of the layers have an angle of 20° to 40° and the remaining 50 % have an angle of >50°. A fibre winding process is used for manufacturing the tank. Therefore, each layer consists of fibres with positive and negative angles. For reasons of clarity, only the positive angle is mentioned here as a representative of the angle-ply sublaminate. In the cylindrical part, all 87 angle-ply sublaminates have a thickness of 0.25 mm. In the dome area, the fibre direction and thickness of the layers change due to the manufacturing process. In addition, not all plies run to the end of the tank (opening), but end before. Which layers these are is not relevant for this thesis and is therefore not explained further, but they were considered when modelling the stacking sequence in LS-DYNA.

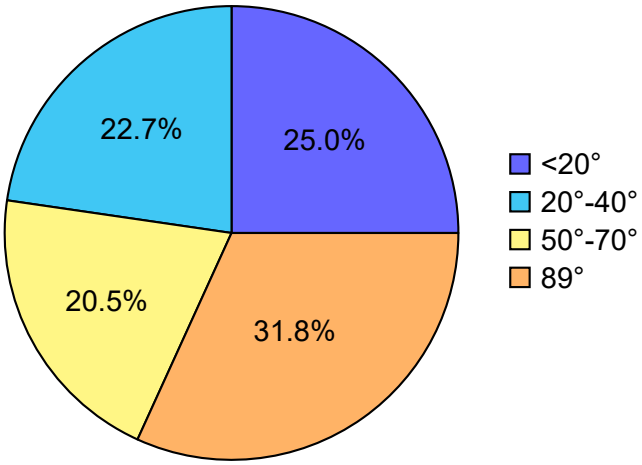

Figure 4.50: Proportions of fibre angles in the stacking sequence of the tank structure

Mesh

The model parameters from Table 4.11 are used to create the simulation model. The large difference in the number of composite layers between the tank and the simplified model (87 to 4 angle-ply sublaminates) means that the number of elements in the radial direction is re-evaluated. Modelling with one element per angle-ply sublaminate results in a model with 87 elements over the 21.75 mm wall thickness of the tank. The high number of elements in combination with the very low element height, which influences the maximum time step size, leads to very long simulation times. The configurations listed in Table 4.12 are simulated in this study.

Due to the high number of composite layers, the number of elements and integration points per element is presented differently in this section. The term combined layers (cl) is newly introduced. It describes how many angle-ply sublaminates are combined in one element. This means that a model with $cl = 1$ has one angle-ply sublaminate (e.g. $\pm$89°) per element. As an odd number of sublaminates with $cl = 2$ cannot be divided exactly between the elements, fewer sublaminates may be combined in the last element. In the case of $cl = 2$, this would mean that the outermost element contains only one sublaminate. The number of integration points per element is adjusted so that each angle-ply sublaminate is represented by two integration points.

Table 4.12: Configurations for tank simulation

Element Type	Combined layers	Load case
solid	0.5	pressure + impact
tshell	1	pressure + impact
tshell	2	pressure + impact
tshell	4	pressure + impact
tshell	8	pressure + impact
tshell	16	pressure + impact

In addition to the tshell elements, a configuration with solid elements is also shown in the table. It serves as an additional comparative variable for re-evaluating the number of elements in the radial direction. It is also intended to show whether a simulation with solid is possible and meaningful. With solid elements, it must be noted that each angle-ply sublaminate must be modelled with two elements in the thickness direction, as the different angles of the $\pm$pair cannot be modelled in one solid element. A model with solid elements therefore requires at least 187 elements in the thickness direction in order to be able to model the stacking sequence. The other modelling parameters from Table 4.11, such as inter-layer model, gas model, etc., are implemented in the same way as in the previous sections.

Boundary Conditions

Due to the change in geometry from the tube to the tank, the boundary conditions must be adapted. Two types of supports are combined. On the one hand, the displacements are limited at the nodes located directly at the openings (see Figure 4.51). In addition, the tank is held and supported by clamps in the cylindrical area (see Figure 4.52).

The openings in the tank model are closed by fittings in the real application. These contain the connection to the hydrogen pipework system on at least one side. As this connection is attached to the structure surrounding the tank, the tank is supported by the fittings. In the model, this support is realised by SPCs in x, y and z direction at one end and y and z direction at the other end at the nodes shown in Figure 4.51.

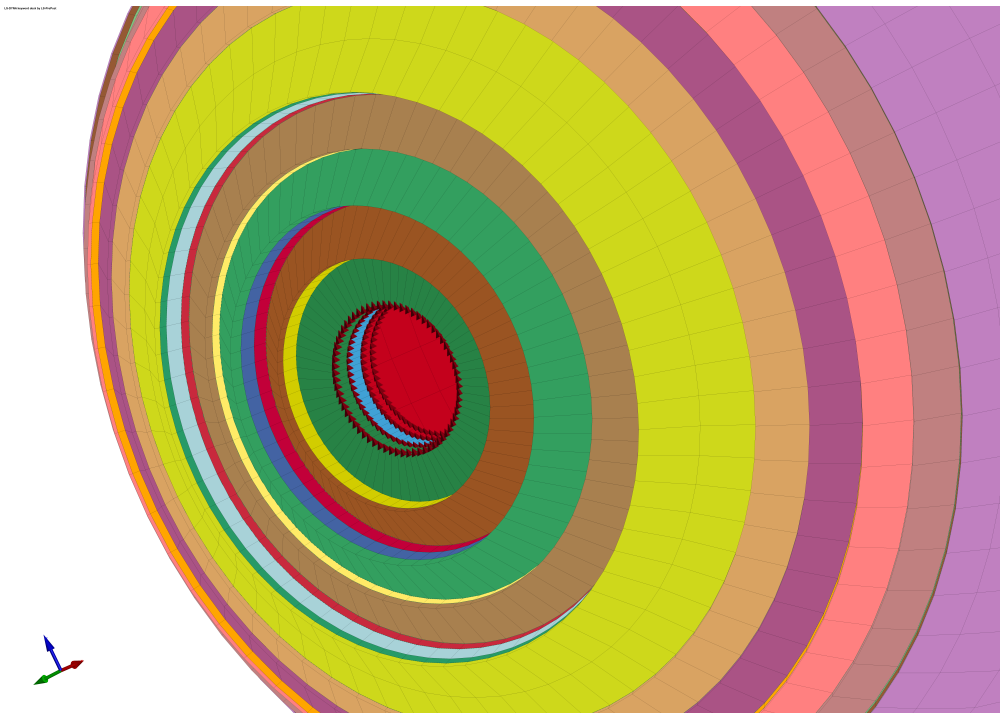

Figure 4.51: SPC boundary condition (red markers)

In addition to attaching the fittings, the tank is supported by clamps (Figure 4.52). It must be ensured that the clamps do not restrict the expansion of the tank too much during filling and at the

same time can absorb the load from the impact. In the model, this is realised in such a way that the clamps behave elastically during filling and are rigid elements during the impact. A frictional contact (*CONTACT_AUTOMATIC_SURFACE_TO_SURFACE) is defined between the tank and the clamps to transfer the loads.

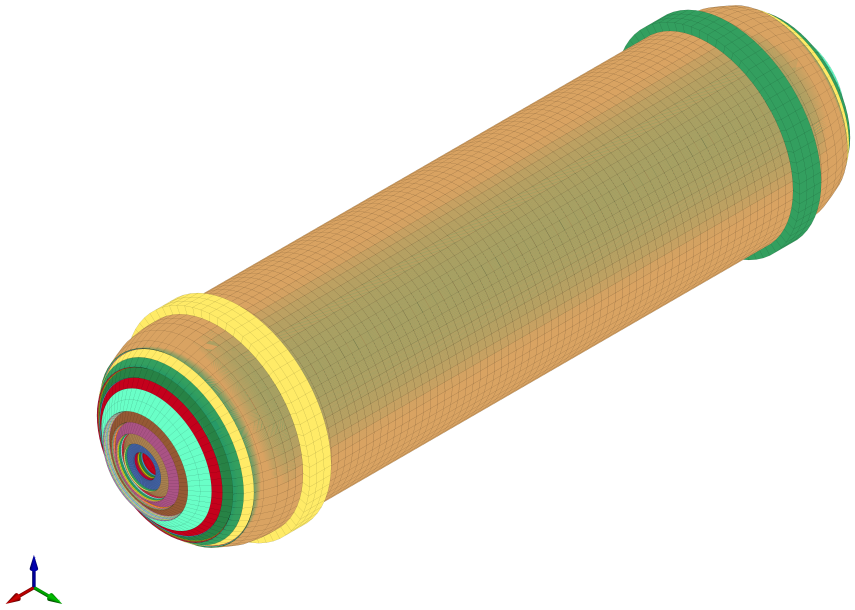

Figure 4.52: Clamps for tank support (yellow and green rings)

Only a few changes are made in the definition of the loads compared to the previous investigations. The internal pressure is modelled as a gas and interacts with the entire inner surface of the tank. The internal pressure is reduced to around two-thirds of the nominal value of 70 MPa, to be able to easily recognise different deformations in the simulation results and at the same time achieve a high load due to the internal pressure. This means that an internal pressure of 45 MPa is used for this investigation. An axial load is not necessary in this case, as the internal pressure on the dome areas automatically leads to an axial load in the cylindrical area.

Material Data and Time Step Size

For most models and simulations, the same material parameters and the same minimum time step size are used as in the previous simulations. Running the simulations showed that the models with many elements across the wall thickness (cl0.5, cl1 and cl2) are prone to instabilities. One reason for these instabilities are the very flat elements. As 174, 87 or 44 elements are modelled over the wall thickness of 21.75 mm, the height of each individual element is very low. This low element height leads to a reduction in the maximum time step for a stable simulation. If the maximum time step size falls below the minimum time step size defined by the user, mass scaling is applied to achieve the minimum time step size. The more mass scaling is required, the higher the probability that the simulation will become unstable.

In this thesis, two approaches are used to counteract the instability. Firstly, the minimum time step size can be lowered in order to reduce the mass scaling. This can lead to a considerable increase in the overall simulation time and should therefore be avoided if possible. A second way to stabilise the simulation is to use a more complex material model. In this case material model Mat54 is replaced by Mat262. Mat262 is also a material model for anisotropic materials such as fibre composites but uses a more complex failure model compared to Mat54. Since the same material properties are used as for Mat54 and material failure is not relevant for this investigation, only a small difference in the simulation results is expected. Mat262 is used because the failure model is less abrupt compared to Mat54. This abrupt failure in Mat54 can lead to instabilities in the simulation. For a similar reason, the material model of the cohesive elements is also changed from the bilinear Mat138 to the trilinear Mat240 (cf. Chapter 2.2.4). The more complex material models have not been used so far, as the failure model and the stabilising effect were not required, and the computational effort increases through the use of these material models. Further details on the material models can be found in the Keyword Manual II [27].

The more complex material model is used for all three configurations mentioned, as the increase in simulation time due to the use of the more complex material models is less significant than the reduction in the minimum time step size. The time step size is only adjusted for the model with cl0.5, as the adjustment of the material is not sufficient there. The time step size is reduced from $2 \cdot 10^{-5}$ ms to $5 \cdot 10^{-6}$ ms.

4.7.3 Simulation Results Re-Evaluation

The same result variables are used to analyse the re-evaluation as in the interlayer study. This means that the reaction force on the impactor and the energies are analysed first and then a graphical analysis of the deformations and delaminations is carried out. In addition, the computational effort is analysed based on the simulation time.

Reaction Force

Figure 4.53 shows the reaction force on the impactor.

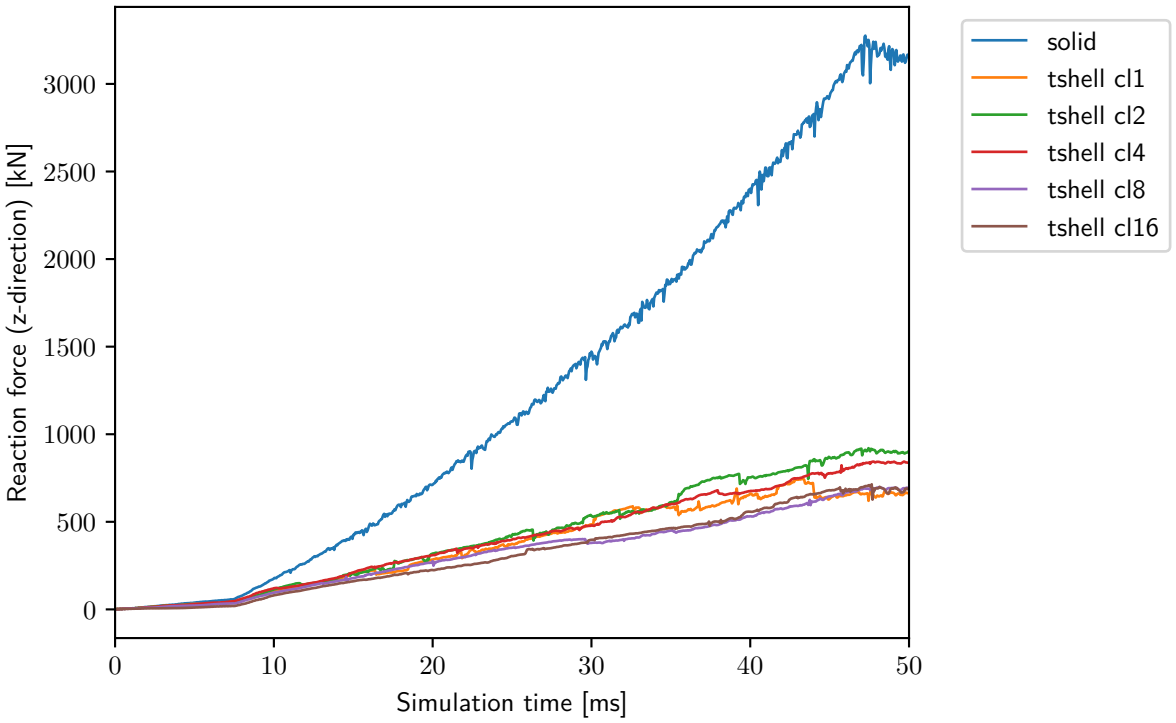

Figure 4.53: Reaction force on indenter (Tank investigation)

The curves of the reaction forces fundamentally reflect the results from the previous investigation of the inter-layer models. The progressions of all curves are roughly linear. What is most striking in this diagram is that the reaction force of the model with solid elements is significantly greater (by a factor of around six to seven) than of the models with tshell elements. This greatly increased reaction force can be explained by the fact that significantly fewer delaminations occur in this model (see graphical evaluation). Interconnected layers have a higher stiffness than several delaminated layers, which means that a higher force is required for the same deformation.

The curves of the models with tshell elements are all relatively close to each other. At the end of the simulation, all curves are in the range between 600 kN and 800 kN. A slight tendency can be recognised, which suggests that more combined layers lead to lower reaction forces. This tendency is only contradicted by the model with cl1, which has the lowest reaction force at the end.

Energies

Figure 4.54 shows the energies of the simulations. When assessing the energies, the same evaluation criteria apply as for the analysis of the interlayer models. The criteria are the fulfilment of the energy equilibrium, an hourglass energy that is less than 10 % of the internal energy and that all energies are positive.

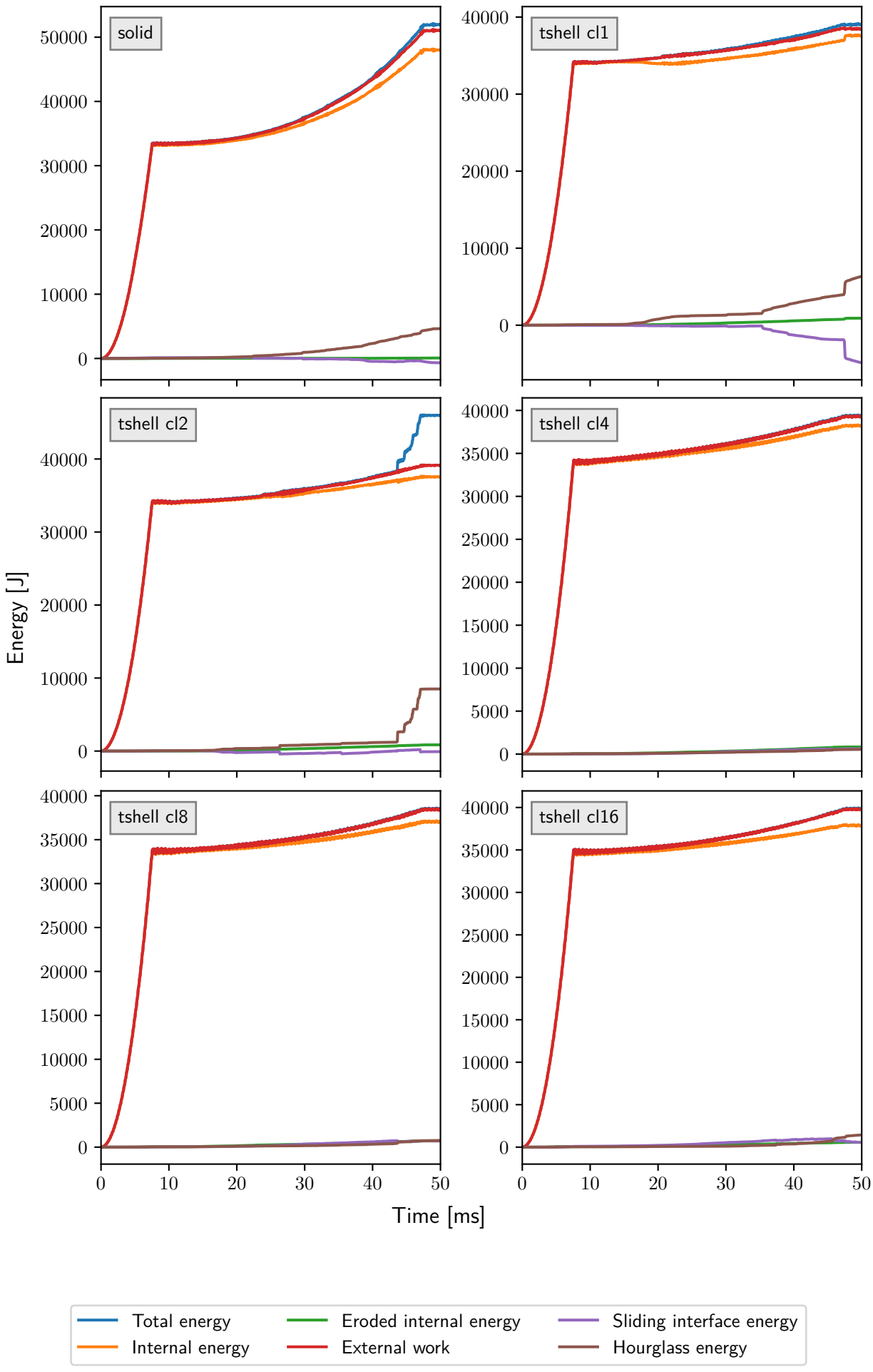

Figure 4.54: Energies (Tank investigation)

The course of the total energy and the external work is qualitatively the same in all diagrams in Figure 4.54 with a small exception in the model with cl2. The curve starts with a sharp rise, then has a kink point and changes to a slightly quadratically rising curve. The two areas of the simulation can be recognised in these curves. The sharp rise at the beginning represents the build-up of internal pressure and the area after the kink represents the impact load case. The area of the pressure build-up is not explained further, as all simulations behave the same in this area. In the simulation part with the impact, the simulation results differ.

The increased reaction force in the model with the solid elements from Figure 4.53 can be seen in the energies in the form of the external work. While the external work in the models with tshell elements is just under 40 kJ at the end of the simulation, it increases significantly more in the model with the solid elements and ends at just over 50 kJ.

If the quality of the simulation results is assessed on the basis of the criteria mentioned, it is noticeable that the models with fewer elements (cl4, cl8 and cl16) deliver better results than the models with more elements. The model with the solid elements and the models with cl1 and cl2 are affected by slight hourglassing. This leads to the correlations known from the last study. Firstly, a slight deviation from the energy equilibrium can be recognised, as the total energy is slightly greater than the external work, and secondly, the hourglass energy is mirrored by a negative SI energy. The model with cl2 also shows a new behaviour. There, the hourglass energy rises sharply at the end. As this increase is not mirrored by the SI energy, the increase leads to an equivalent increase in the total energy. This creates an additional imbalance in the energy equilibrium. Why this behaviour only occurs in the model with cl2 and in no other model in this thesis could not be investigated.

The models with cl4, cl8 and cl16 are not affected by hourglassing and therefore fulfil all energy criteria for good quality simulation results. The fact that these models are less susceptible to hourglassing is possibly due to the shape of the elements. The elements of these models are thicker with the same base area. This less elongated shape could make them less prone to hourglassing.

Graphical Results

The graphical analysis of the simulation results is similar to the graphical analysis of the ILM investigation. For the evaluation, the delaminations in the entire tank and the deformation in the cross-section are analysed. The delaminations of the configurations with many elements (cl0.5 to cl2) are shown in Figures 4.55 to 4.57. The figures with the delaminations of the remaining configurations are shown in Appendix F. In the figures, the deleted cohesive elements are shown as representatives of the delaminations in an isometric perspective.

Figure 4.55: Deleted elements (element type: solid; combined layers: 0.5)

Figure 4.56: Deleted elements (element type: tshell; combined layers: 1)

Figure 4.57: Deleted elements (element type: tshell; combined layers: 2)

When comparing the delaminations, the first thing that stands out is that the variant with solid elements has significantly fewer delaminations than the other two configurations. This result fits with the previous finding that less delamination is associated with a higher stiffness and therefore leads to a higher reaction force on the impactor and higher external work. Why less delamination occurs with this configuration cannot be deduced from the collected results.

In all three figures, delamination occurs at the end of the tank at the hole for the fitting. These delaminations are not considered as they are caused by the abrupt end of the layers in the model. In reality, the end of a layer is levelled out by a small accumulation of resin, which makes the transition less abrupt and delamination less likely.

For the two models with tshell elements, the delaminations in the impact area are approximately the same size. The models differ in the delaminations at the transition from the cylindrical area to the dome. Significantly more delaminations are in the model with cl1. These delaminations are located near the surface and do not extend deep into the model. One possible reason why these delaminations only occur in the model with cl1 could be that the outermost layer of the cohesive elements is closer to the surface in this model. Due to the bending load caused by the impactor and the large wall thickness, greater loads occur the closer the cohesive element is to the surface. The loads in the outermost cohesive layer would therefore be greater for the cl1 model than for the other tshell models.

The results of the models with cl4, cl8 and cl16 are similar to the results of cl2 and are therefore shown in Appendix F. With these models, the trend continues that the number of delaminations in the dome area decreases with increasing cl value. Other perspectives (top and front view) are not shown, as these do not provide any new insights.

The next figures (Figures 4.58 to 4.61) show the deformations in the cross-section at $x = 0$. The results of the configurations cl0.5 to cl4 are shown here and the results of the remaining configurations (cl8 and cl16) are shown in Appendix F. In the figures, the impactor is shown in green and the tank structure below it.

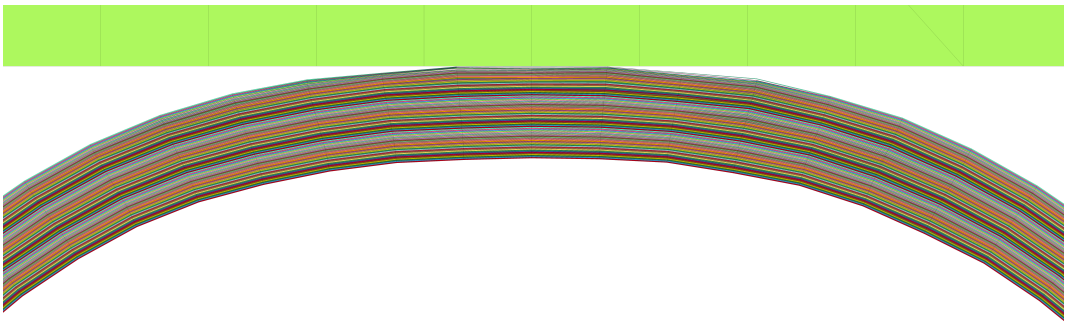

Figure 4.58: Cross section deformation (element type: solid; combined layers: 0.5)

Figure 4.59: Cross section deformation (element type: tshell; combined layers: 1)

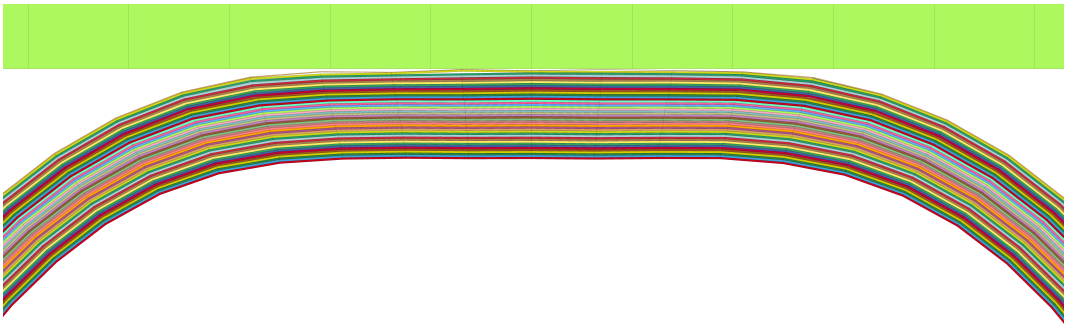

Figure 4.60: Cross section deformation (element type: tshell; combined layers: 2)

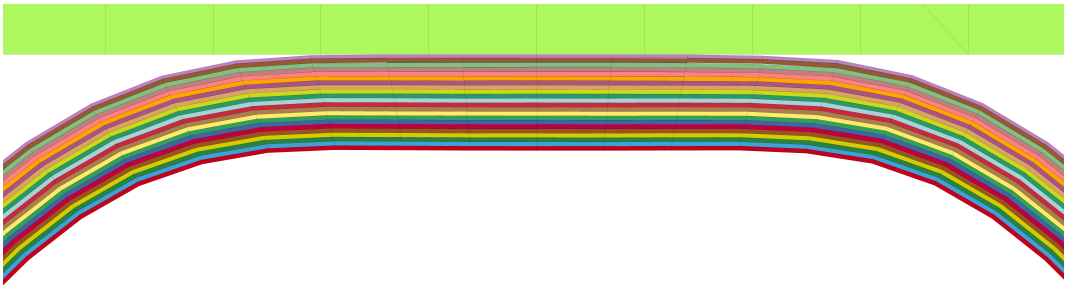

Figure 4.61: Cross section deformation (element type: tshell; combined layers: 4)

The comparison of the deformations confirms the finding that the model with the solid elements has the greatest rigidity. In this model, the deformation of the circular ring structure of the tank is significantly smaller. This means more deflection of the entire tank than deformation of the circular structure.

The deformation (flattening) of the ring shape of the tank is greatest in the configuration with cl2 and cl4. The model with cl1 has a smaller deformation than the models with cl2 and cl4, but it is considerably larger than the solid model. The similar delamination behaviour of the models with cl2 and cl4 matches the similar deformation of both models. The fact that the deformation of the model with cl1 is less can possibly be explained by the additional delaminations in the dome area. Due to these delaminations, the tank could be slightly more elastic normal to the axis of rotation. This would result in more bending deformation and less deformation of the circular structure.

A closer look at the elements that are in direct contact with the impactor reveals that the contact is inaccurate in the models with cl1 and cl2. This inaccuracy is expressed in localised gaps between the uppermost element layer and the impactor as well as detachments (gaps) between the uppermost element layers. These issues do not occur in the model with cl4. The uppermost element layer is in good contact with the impactor and delaminations, but no detachments occur between the uppermost element layers. The deformations of the models with cl8 and cl16 are similar to the deformation of the model with cl4.

In summary, the graphical analysis provided the following results. The findings from the previous analyses were confirmed. The model with the solid elements showed a clearly different behaviour than the models with tshell elements due to the significantly lower number of delaminations. The model with cl1 showed slightly different behaviour in terms of deformation and delamination compared to the other tshell models. The models with cl2 to cl16 delivered the same results apart from minor details.

Simulation Time

As the final part of the re-evaluation, the simulation effort of the different variants is compared. The simulation times are shown in Table 4.13. As the resources on the workstation are limited, a different number of nodes was used depending on the workstation utilisation and the scope of the simulation. For this reason, the table also shows the simulation time for a simulation with a single node in addition to the simulation time. This conversion is not exact, as not all parts of a simulation scale with the number of nodes and communication with additional nodes generates an additional overhead. The conversion is still sufficiently accurate, as the difference between the simulation time is at least 40 min, which is large compared to the time that is required for the additional overhead.

Table 4.13: Simulation time of tank simulation

Combined layers	Number of used CPU nodes	Simulation time	Simulation time on a single node
0.5	4	423 h 34 min 55 s	1694 h 19 min 40 s
1	2	73 h 6 min 5 s	146 h 12 min 10 s
2	2	21 h 24 min 26 s	42 h 48 min 52 s
4	1	6 h 10 min 13 s	6 h 10 min 13 s
8	1	1 h 20 min 12 s	1 h 20 min 12 s
16	1	41 min 3 s	41 min 3 s

It can be seen from the simulation times on a single node that the simulation time increases significantly as the number of elements doubles (from one cl value to the next). Two increases are particularly large. The first is the jump from cl4 to cl2, where the simulation time increases by a factor of about seven. This jump is particularly large due to the additional simulation effort of the more complex material models used for the configurations with cl0.5 to cl2. The second large jump is between the simulation time of the model with cl1 and the model solid model with cl0.5 (about factor 11.5). This large increase is due to the reduction of the minimum time step interval. Between the remaining configurations, the simulation time changes from one cl value to the next by a factor in the range 2.0 to 4.5.

4.7.4 Re-Evaluation

The re-evaluation of the number of elements across the wall thickness has shown that the models with tshell elements all deliver similar results. In contrast, the results of the model with solid elements differ greatly. It is not possible to evaluate the results of which model delivers the most realistic and therefore best results, as no reference values are available. However, it is possible to assess which models have the fewest problems with the simulation and the simulation results. In this case, the models with fewer elements perform better. Specifically, this means the models with cl4, cl8 and cl16. They hardly differ from the other tshell models in terms of the reaction force on the impactor, have no problems with hourglassing, show reasonable deformations and delaminations in the graphical evaluation and have good contact with the impactor. In addition, these models have shorter simulation times.

This result is in contrast to the findings of the preliminary tests, which showed that one element should be used for each angle-ply sublaminate. These different results are due to the fact that problems with elements that are too thin could not occur in the preliminary tests due to the small number of layers in the stacking sequence. Only the investigation of the entire tank with the large number of layers revealed this problem. If the tests are compared independently of the stacking sequence, the preliminary investigations shows that four to eight layers should be used and the investigation in this section shows that six layers provide a good result.

The re-evaluation results in the following suggestions for the simulation methodology for thick-walled hydrogen tanks. If a fast model is required and a detailed representation of the delamination over the wall thickness is not necessary, the use of the model with cl16 is recommended. With this model as a basis, the number of elements over the wall thickness can be increased depending on the application. If a detailed representation of interlayer effects is required, or if the influence of interlayer effects is not known before the simulation, a model with more elements can be used depending on the available computing power. Additional problems such as hourglassing or unstable simulations may occur with the models with cl1 and cl2, which must be taken into account accordingly.

4.8 Application of Simulation Method

Once the modelling method has been determined, the application of the method is presented in this chapter. The use cases presented here are examples. The modelling method can also be used for other applications. One method is selected for the application based on the recommendations in the previous section. This method is used for the investigation of two application-oriented simulations. In the first part, the impact behaviour of the tank at different internal pressures is investigated. The internal pressure is varied between full (70 MPa), half full (35 MPa) and empty (no internal pressure). In the second case, the burst pressure of the tank is simulated. In this case, no impact load is used.

4.8.1 Simulation Model and Parameters

Based on the recommendations from the previous section, the model with cl8 is selected. This model is chosen because hardly any inter-laminar effects are to be expected in the investigations and the short simulation time allows several load cases to be analysed. The model with cl16 is not used as it is possible that the inter-laminar layers influence the burst pressure. The model with cl8 is therefore a good compromise between short simulation times and sufficient inter-laminar layers.

The model from the previous section is reused to investigate the impact behaviour. Compared to the last investigation, only the value of the internal pressure needs to be adjusted, as the load case is qualitatively the same. For the burst pressure analysis, the impactor is removed from the model so that a pure load due to internal pressure is created. A brief preliminary investigation has shown that the clamps have no influence on the burst pressure in this model. They are not used in the investigation in order to keep the model as simple as possible. The internal pressure of the tank is slowly increased with the simulation time. 140 MPa is selected as the final value. In comparison to the burst pressure investigation at the beginning of the thesis, a simulation of the bursting is possible in this case, as a different geometry is used. Due to the different geometries of the cylindrical inner part and the dome-shaped ends, the tank is not expected to rupture over its entire length.

4.8.2 Simulation Results Impact

The impact load cases are analysed using the same methods as in the previous section (reaction force, energy, delamination and deformation). However, in this case the analysis of the energies is not carried out, as it is expected that this analysis will not provide any new findings in addition to the other analyses.

Figure 4.62 shows the reaction force of the tank on the impactor for the variants with different internal pressures.

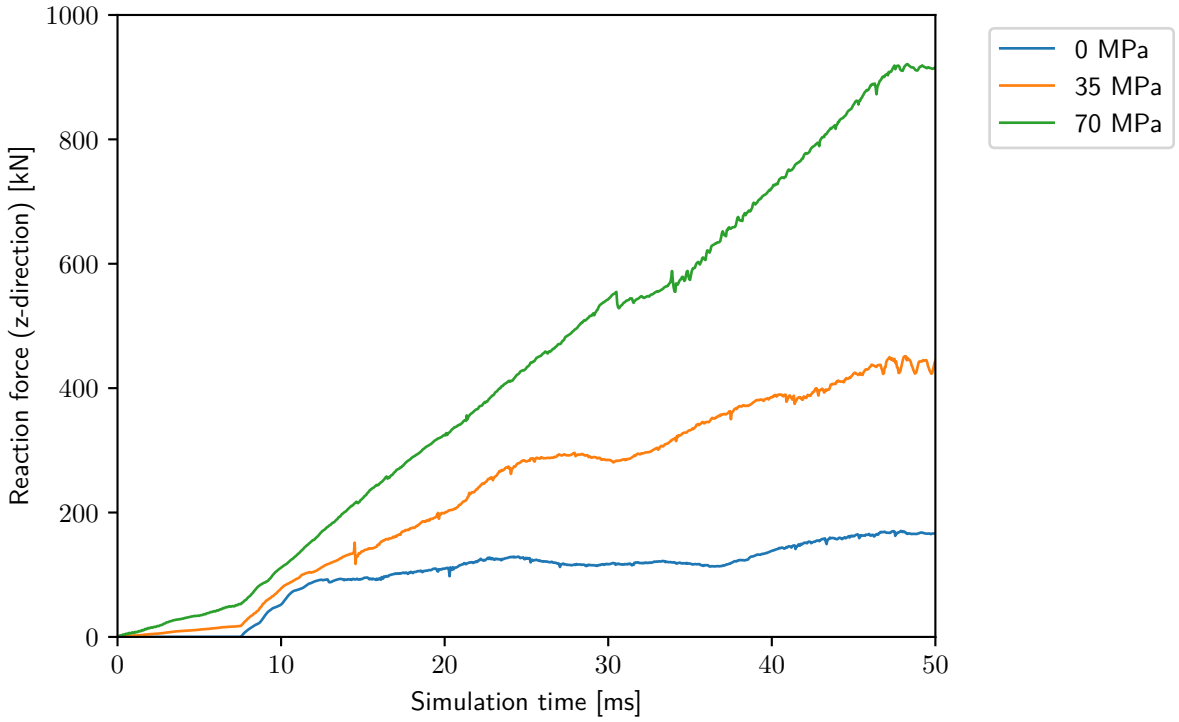

Figure 4.62: Reaction force on impactor (impact investigation)

The diagram shows the three steps of the simulation. In the first step up to 7.5 ms, the internal pressure is built up. In the second step (7.5 ms to 47.5 ms), the tank is impacted. In the last 5 % of the simulation, from 47.5 ms to the end, the external loads are constant so that oscillations in the curves have a smaller effect on the final value.

The different course of the curves in the first section is because the gap between the impactor and the tank in the initial state is smaller than the expansion of the tank. As the tank does not expand without internal pressure, no force acts on the impactor. The second section is the most relevant for comparing the models. The basic shape of the curves corresponds to the expectation. The tank with the highest internal pressure generates the greatest forces on the impactor and the tank without internal pressure the lowest forces. The curves also show how much load the tank can absorb before the first delamination occurs and what proportion the internal pressure has on the resistance of the tank.

The curve of the tank without internal pressure rises linearly up to around 100 kN and then bends. After that, the increase in force is very low until the end of the simulation and final value is around 180 kN. This shows that the structure of the tank can absorb 100 kN before major damage occurs. The simulation result of the filled tank (70 MPa) shows a different course. This curve increases linearly over the entire simulation. One exception is a small jump between 30 ms and 35 ms. This jump indicates that larger delaminations occur there. The linear progression shows that the tank structure is strongly supported by the internal pressure. The final value of the curve is just over 900 kN. The simulation result of the model with 35 MPa internal pressure shows elements from both curves. The curve rises more than without internal pressure but also shows a slightly flattening curve. The model behaviour lies in the middle between the two other variants. However, the final value of the curve with a value just above 400 kN is significantly closer to the final value of the model without internal pressure than to the final value of the model with 70 MPa. This could lead to the conclusion that the stabilising effect of the internal pressure increases faster than the value of the internal pressure. To verify this assumption, further tests with different internal pressures would have to be carried out.

The delaminations (deleted elements) are shown in the following three figures (Figures 4.63 to 4.65). Only the isometric view is used for the illustration, as other views do not provide any additional information.

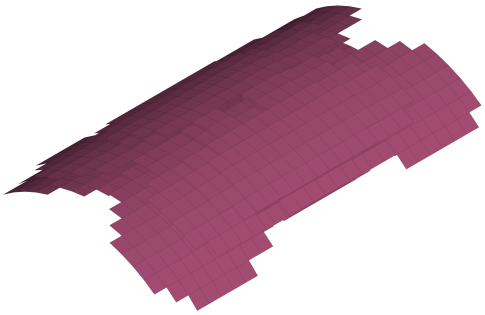

Figure 4.63: Deleted elements (internal pressure: 0 MPa)

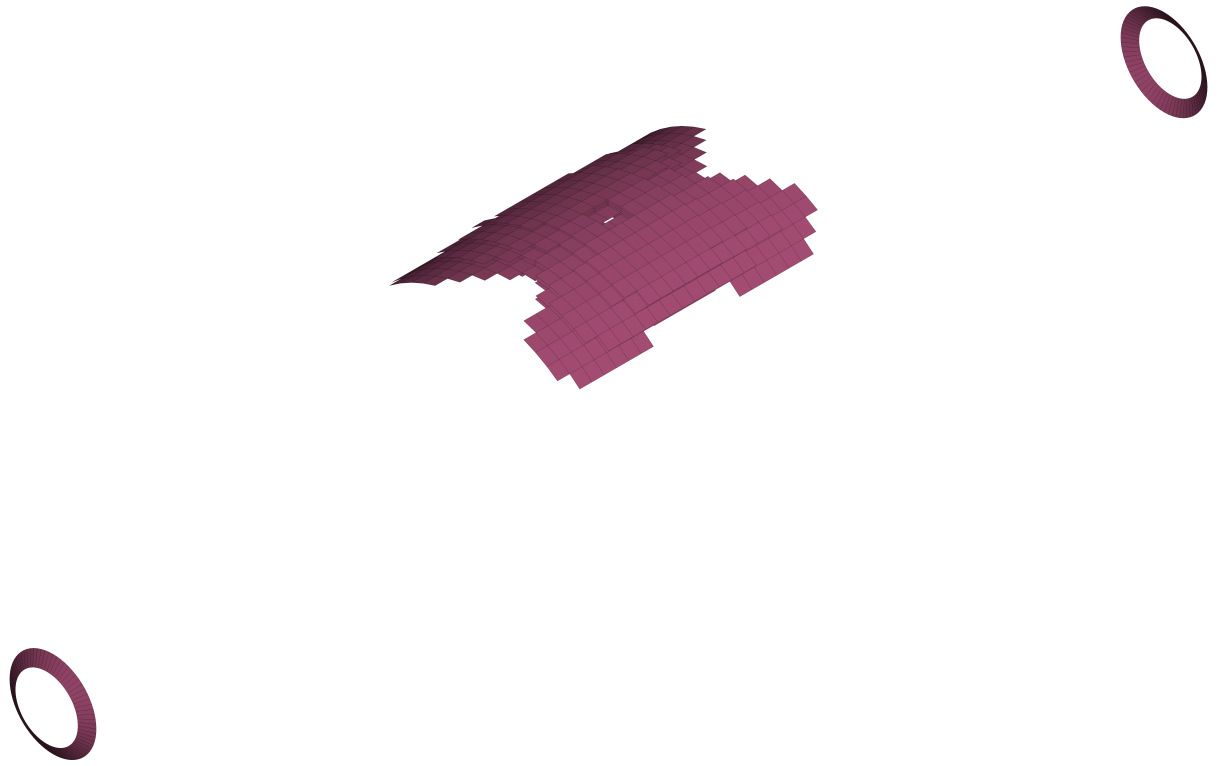

Figure 4.64: Deleted elements (internal pressure: 35 MPa)

Figure 4.65: Deleted elements (internal pressure: 70 MPa)

The figures show that the delamination in the impact area is very similar for all three models. The most noticeable difference in this area is that the x-shape of the delamination area is easier to recognise when the tank is empty or half full. Outside the impact area, it is noticeable that the delamination in the dome area increases with increasing internal pressure. In the image of the tank without internal pressure, only the impact area is shown, as no other delaminations occur. The expansion of the delaminations is a further sign of the stabilising effect of the internal pressure. This effect means that the load and therefore also the deformation is distributed more evenly across the tank. The higher loads in the dome area lead to the additional delaminations.

Figures 4.66 and 4.67 show the deformation of the tank. In contrast to previous investigations, the deformation is not analysed based on the cross-section, as the differences are difficult to recognise there. Instead, the deformation in the impact direction (z-direction) is shown using a colour scale. To ensure comparability, the same scale is used in both figures. As the model with 35 MPa forms an intermediate value between 0 MPa and 70 MPa, as in the other analyses, this model is not analysed in this case.

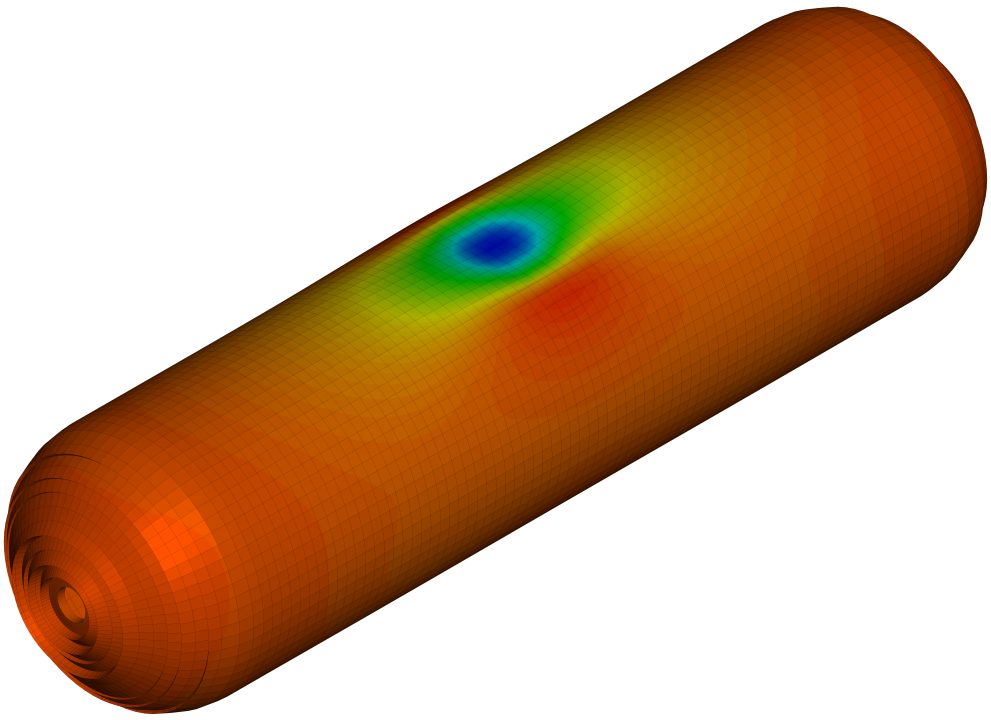

Figure 4.66: z displacement (internal pressure: 0 MPa)

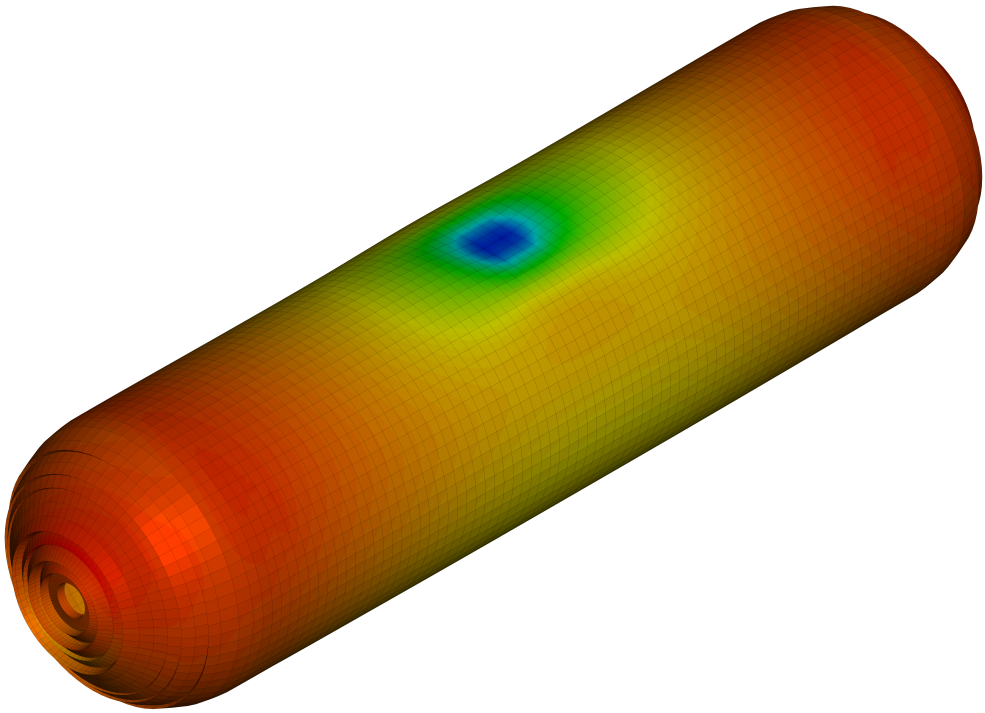

Figure 4.67: z displacement (internal pressure: 70 MPa)

The findings of the previous analyses can be directly recognised in these results. The deformation of the tank without internal pressure occurs almost only in the impact area. The depression caused by the impactor can be clearly recognised (blue and green colours). A reddish colouring can also be observed to the side of the impact. This indicates a slight bulge in the tank. The combination of the blue and green colours in the centre and the reddish ones next to it shows a deformation of the circular shape of the cross-section in this area. In comparison, the model with 70 MPa internal pressure shows almost no bulging next to the impact, which indicates less deformation of the circular cross-section. Instead, the entire tank bends significantly more, which can be recognised by the yellowish colour tones in the middle area. To summarise, it can be stated that an increased internal pressure leads to a lower local deformation and a higher global deformation.

4.8.3 Simulation Results Burst Pressure

The simulation of bursting resulted in the following failure pattern (Figure 4.68).

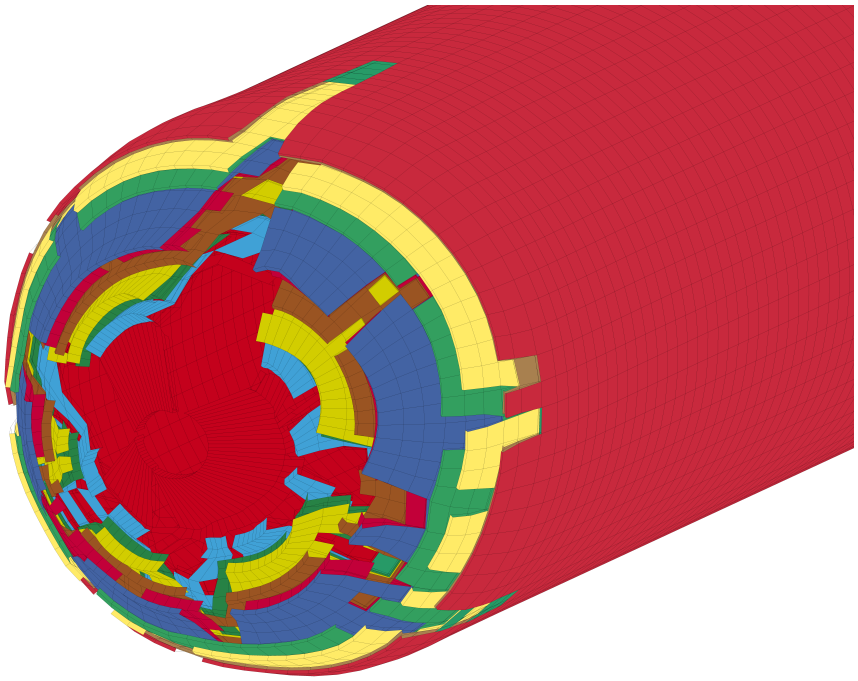

Figure 4.68: Burst failure

The illustration shows that the failure occurs in the dome area. It is likely that the failure starts at the opening of the tank. The diagram in Figure 4.69 shows the course of the internal pressure.

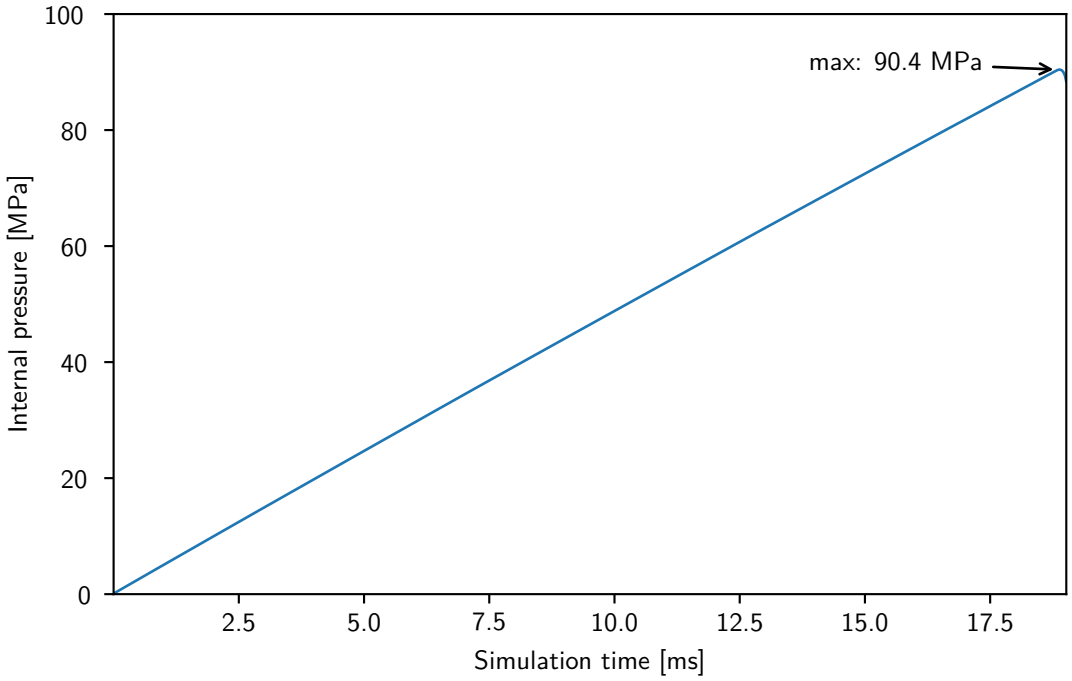

Figure 4.69: Internal pressure of tank

At 90 MPa, the burst pressure achieved is well below the expected burst pressure. The stacking sequence was designed for a burst pressure of 140 MPa. The fact that the expected burst pressure is not reached is probably not due to the modelling method, but to the model used. The model has two decisive differences compared to reality. Firstly, the metal insert that closes the openings at the tank ends is missing. This insert is not only attached to the annular surface of the opening, but also to part of the inner surface of the dome (see Figure 2.1 in Section 2.1). As a result, the boundary conditions are introduced over a larger area than is the case in the model. In addition, a closed opening is less prone for the start of a failure. The second difference compared to reality is the end of the layers. In the model, the layers end abruptly, whereas in reality a smoother transition occurs due to the resin.

These differences between the model and reality mean that neither the value of the burst pressure nor the failure behaviour would occur in reality in the same way. An evaluation of the modelling method is difficult in this context. However, it is conceivable that the model used with the aforementioned differences to reality exhibits such a failure.

4.8.4 Application Findings

The application of the modelling methodology has shown that the simulations deliver meaningful and comprehensible results in terms of qualitative structural behaviour. From this perspective, the simulation methodology fulfils the requirement of being able to simulate a tank structure in different load cases while taking the detailed fibre architecture into account. However, a comparison with reference values is not possible, as either no reference values are available, or the model is inadequate for a comparison. Therefore, it is not certain that the method will deliver precise results.

5 Conclusion

The aim of this thesis is to develop a simulation methodology for the analysis of thick-walled hydrogen tanks. In the first step, the current state of the art was determined through literature research. Subsequently, four preliminary investigations were carried out on a simplified tank model. In these preliminary tests, various load cases were used to determine the most suitable values for the most important modelling parameters. A modelling method was selected based on the results of the preliminary tests. This method was tested on the overall tank model and the parameter selection was refined. Finally, the refined modelling method was applied to two sample load cases.

The investigations have led to the following results. The stress and displacement values of the simulations with shell elements deviate significantly from the reference values. This means that shell elements are unsuitable for simulating the structural behaviour of the tank despite the very low computational effort involved.

The investigation of the number of elements over the wall thickness has shown that a combination of several fibre composite layers with different fibre angles in one element leads to inaccurate stress results. This finding only applies to structures with a few thick layers. In this case eight layers with a thickness of $t_{layer} = 2.5mm$ were used. The investigation on the tank with 87 layers has shown that the elements must not be too thin, as hourglassing and instabilities occur in this case. Models with 22 or fewer elements and $t_{layer} \geq 1.0mm$ delivered good results. The comparison of the simulation times has shown that a higher number of elements has a greater effect on the simulation time than a larger number of integration points. Thus, halving the number of elements across the wall thickness in combination with increasing the number of integration points to model the same number of fibre composite layers leads to a shorter simulation time.

For the number of elements across the wall thickness, models with solid elements are dependent on the number of fibre layers. When using solid elements, at least one element must be used for each fibre orientation. This makes solid elements unsuitable for models with many thin layers of different fibre angles.

When modelling the internal pressure, the control volume (CV) method provides similarly good results as modelling the pressure as a load. The use of the CV method enables an extension of the modelling and evaluation options in the thermodynamic area. The additional computational effort compared to the direct load is negligible. Compared to the corpuscular particle method (CPM), the CV method is less extensive and detailed. However, it is easy to implement, less susceptible to instabilities in the simulation and requires less computational effort compared to the CPM.

The element size or mesh density has no significant influence on the simulation results when the tank is loaded with internal pressure. Under impact loading, a fine mesh is recommended, as this can model the deformation in more detail and more realistically.

Using cohesive contacts as an inter-layer model (ILM) leads to strong hourglassing. In contrast, significantly less hourglassing occurs with cohesive elements and in some cases none at all. The use of cohesive elements is therefore recommended.

The choice of the solver depends on the use of contacts. If no contacts are used, an implicit solver leads to quick results. However, if contacts are used, e.g. for the impactor or the ILM (eroding contact), an explicit solver is more suitable. In addition to contacts other criteria, such as large deformations, favour the use of an explicit solver.

From the above findings the following conclusions can be drawn. Tshell elements should be used as the element type. They provide precise results and can be used flexibly at the same time. The number of elements can be adapted to the desired resolution of the interface layers and the available computing power via the wall thickness in combination with the number of integration points per element. When modelling the internal pressure, the CV method can be used if thermodynamic variables are relevant for the simulation. Otherwise, modelling the pressure directly as a load is sufficient. The element size should be adapted to the load case. Local load cases such as an impact require a fine mesh (1.5), while a coarse mesh (6.0) is sufficient for global load cases such as pure internal pressure. Cohesive elements are recommended as an inter-layer model. For the solver, implicit is the faster option in selected cases, while the explicit solver can be used in all other cases.

Based on these conclusions, the model parameters in Table 5.1 were selected for an application example.

Table 5.1: Selected parameter combination for application

Parameter	Value
Element type	Tshell
Number of elements (radial)	11 (two per angle-ply sublaminate)
Integration points per element	2 (two per angle-ply sublaminate)
Solver	Explicit
Element size (rel)	1.5
Internal pressure model	Gas (CV)
Inter-layer model	Cohesive elements

The application has shown that the results for the impact load case are conclusive. However, a more precise assessment is not possible without reference values. The expected results are not achieved for burst failure. This is probably not due to the simulation methodology, but to an inadequate simulation model.

In this thesis, a simulation methodology was developed for the simulation of thick-walled hydrogen tanks. With the selected methodology, the behaviour of the fibre structure under internal and external loads can be simulated in detail. At the same time, the simulation effort can be flexibly chosen via the level of detail. In addition to the structural behaviour, thermodynamic variables can also be simulated.

6 Outlook

The investigations in this thesis include many different modelling parameters. Due to the large number of parameters analysed, not all of them could be examined in detail. In addition, new questions have arisen from this thesis. For this reason, possible topics of investigation that would extend or deepen the results of this thesis are presented below.

One possible topic is the verification of the research results with experimental data. In this thesis, all simulations with impact load cases could only be evaluated for conclusiveness based on various result variables such as deformation behaviour and energy balances. Verification of the results with data would support the findings of this work.

A second topic that could extend the scope of this thesis would be a detailed investigation of the CPM method. The stable integration of the method into a good tank model could open new possibilities in the joint investigation of thermodynamic and structural mechanics.

A third option is to continue the application of the simulation methodology. The simulation of the burst pressure has shown that the model used is inadequate for a simulation. Extending the model to include the fittings and other components such as the liner would improve the quality and accuracy of the model.

This work provides a good basis for further investigation of the topics identified.

Bibliography

[1] Umweltbundesamt, “Europäische energie- und klimaziele,” https://www.umweltbundesamt.de/daten/klima/europaeische-energie-klimaziele#zielvereinbarungen, 2023, last accessed: 2024-09-05.

[2] W. F. Lamb *et al.*, “A review of trends and drivers of greenhouse gas emissions by sector from 1990 to 2018,” *Environtal Ressearch Letters*, vol. 16, no. 073005, 2021.

[3] C. Diaz, “1 in 7 cars sold globally now is electric,” https://www.weforum.org/agenda/2023/03/ev-car-sales-energy-environment-gas/, 2023, last accessed: 2024-09-11.

[4] A. Magliano, C. Perez Carrera, C. M. Pappalardo, D. Guida, and V. P. Berardi, “A comprehensive literature review on hydrogen tanks: Storage, safety, and structural integrity,” *Applied Sciences*, vol. 14, no. 20, 2024. [Online]. Available: https://www.mdpi.com/2076-3417/14/20/9348

[5] C. Winnefeld, T. Kadyk, B. Bensmann, U. Krewer, and R. Hanke-Rauschenbach, “Modelling and designing cryogenic hydrogen tanks for future aircraft applications,” *Energies*, vol. 11, no. 1, 2018. [Online]. Available: https://www.mdpi.com/1996-1073/11/1/105

[6] M. P. Alves, W. Gul, C. A. Cimini Junior, and S. K. Ha, “A review on industrial perspectives and challenges on material, manufacturing, design and development of compressed hydrogen storage tanks for the transportation sector,” *Energies*, vol. 15, no. 14, 2022. [Online]. Available: https://www.mdpi.com/1996-1073/15/14/5152

[7] CAE Training and Consulting, “Ls-dyna implicit training: Lecture 1: Implicit versus explicit,” https://www.youtube.com/watch?v=oT0a4b5P74w, 2020, last accessed: 2024-09-19.

[8] ANSYS, Inc., *LS-DYNA KEYWORD USER’S MANUAL VOLUME I*, 14th ed., ANSYS,Inc., Canonsburg, Pennsylvania, 2024.

[9] DYNAmore GmbH, “What are the differences between implicit and explicit?” https://www.dynasupport.com/faq/general/what-are-the-differences-between-implicit-and-explicit, 2024, last accessed: 2024-09-19.

[10] T. Erhart, T. Borrvall, N. Karajan, M. Schenke, and C. Schmied, “Implicit analysis using ls-dyna,” https://www.dynamore.de/de/download/presentation/2020/implicit-2020.pdf, 2020, last accessed: 2024-09-19.

[11] Livermore Software Technology, *LS-DYNA Theory Manual*, 14765th ed., Livermore Software Technology, Livermore, California, 2022. [Online]. Available: https://ftp.lstc.com/anonymous/outgoing/jday/manuals/DRAFT_Theory.pdf

[12] DYNAmore GmbH, “Elements.” [Online]. Available: https://www.dynasupport.com/tutorial/ls-dyna-users-guide/elements

[13] P. Hadagali, “Subject-specific finite element modeling of the adolescent thoracic spine for scoliosis research.” Ph.D. dissertation, 09 2014.

[14] R. Maini, “A three-dimensional numerical analysis of the effect of embedding cylindrical microwire sensors on the compressive strength of carbon-fiber reinforced composite laminates,” Ph.D. dissertation, 12 2017.

[15] DYNAmore GmbH, “Shell formulations.” [Online]. Available: https://www.dynasupport.com/howtos/element/shell-formulations

[16] P. Thakor, K. Sunil, U. Kumar, Nidhi, and S. Shanbhag, “Fe analysis of egg shaped shells,” 09 2021.

[17] Kitware Public, “Gauss 5x1,” https://vtk.org/Wiki/File:GAUSS_5x1.png, 2012, accessed: 2025-01-12.

[18] D. K. Ceng Mrina Msname, W. Ng, O. Hwang, J. Sohn, and E.-B. Lee, “Recommended finite element formulations for the analysis of offshore blast walls in an explosion,” *Latin American Journal of Solids and Structures*, vol. 15, 10 2018.

[19] ANSYS, Inc., “Incompressible cfd solver,” 2024. [Online]. Available: https://lsdyna.ansys.com/icfd/

[20] ——, “Simulate the response of materials to short periods of severe loading,” 2024. [Online]. Available: https://www.ansys.com/de-de/products/structures/ansys-ls-dyna

[21] A. Hirth, A. Haufe, and L. Olovsson, “Airbag simulation with ls-dyna past – present – future,” 6th European LS-DYNA Users’ Conference, Gothenburg, 2007.

[22] S. Mattern, “Overview on airbag-modeling possibilities in ls-dyna,” DYNAmore GmbH, 2020. [Online]. Available: https://www.dynamore.de/de/download/presentation/2020/201009_dynamore-express__airbag-modeling.pdf

[23] J. Macher, A. Hausberger, A. Macher, M. Morak, and B. Schrittesser, “Critical review of models for h2-permeation through polymers with focus on the differential pressure method,” *International Journal of Hydrogen Energy*, vol. 46, 05 2021.

[24] DYNAmore GmbH, “Tied, tied offset, and tiebreak contacts.” [Online]. Available: https://www.dynasupport.com/howtos/contact/tied-tied-offset-and-tiebreak-contacts

[25] H. Fang and D. Wang, “Simulation analysis of delamination damage for the thick-walled composite-overwrapped pressure vessels,” *Materials*, vol. 15, no. 19, p. 6880, 2022.

[26] DYNAmore GmbH, “Cohesive element formulation.” [Online]. Available: https://www.dynasupport.com/howtos/element/cohesive-element-formulation

[27] ANSYS, Inc., *LS-DYNA KEYWORD USER’S MANUAL VOLUME II*, 14th ed., ANSYS,Inc., Canonsburg, Pennsylvania, 2024.

[28] A. Maurel-Pantel, M. Voisin, Q. Bui, N. Cocheteau, F. Lebon, and C. Hochard, “A cohesive zone model for fracture initiation and propagation of fused silica direct bonding interface,” *Engineering Fracture Mechanics*, vol. 219, p. 106649, 09 2019.

[29] L. Jiang, S. Xiao, B. Yang, Y. Guangwu, T. Zhu, D. Dong, and J. Zhang, “Finite element analysis of tensile properties for single-strap butt joint of carbon fiber reinforced composite,” *Computing in Science & Engineering*, vol. PP, pp. 1–1, 11 2018.

[30] DYNAmore GmbH, “Energy data.” [Online]. Available: https://www.dynasupport.com/tutorial/ls-dyna-users-guide/energy-data

[31] ——, “Total energy.” [Online]. Available: https://www.dynasupport.com/howtos/general/total-energy

[32] ANSYS, Inc., “Contact energy.” [Online]. Available: https://lsdyna.ansys.com/contact-energy/

[33] I. Gandikota, “What is rigid wall energy and how do i output this quantity?” [Online]. Available: https://ansys13.ansys.com/KnowledgeArticles/Phase-2A/2062877/2062877.pdf

[34] DYNAmore GmbH, “Damping.” [Online]. Available: https://www.dynasupport.com/howtos/general/damping

[35] ——, “Hourglass.” [Online]. Available: https://www.dynasupport.com/howtos/element/hourglass

[36] E. Q. Sun, “Shear locking and hourglassing in msc nastran, abaqus, and ansys,” in *Msc software users meeting*, 2006, pp. 1–9.

[37] Z. Zlatev, I. Dimov, I. Faragó, and Á. Havasi, *Richardson extrapolation: Practical aspects and applications*. Walter de Gruyter GmbH & Co KG, 2017, vol. 2.

[38] I. B. Celik, U. Ghia, P. J. Roache, and C. J. Freitas, “Procedure for estimation and reporting of uncertainty due to discretization in cfd applications,” *Journal of fluids Engineering-Transactions of the ASME*, vol. 130, no. 7, 2008.

[39] H. Wang, S. Fu, Y. Chen, and L. Hua, “Thickness-prediction method involving tow redistribution for the dome of composite hydrogen storage vessels,” *Polymers*, vol. 14, no. 5, p. 902, 2022.

[40] Z. Hu, M. Chen, and B. Pan, “Simulation and burst validation of 70 mpa type iv hydrogen storage vessel with dome reinforcement,” *International Journal of Hydrogen Energy*, vol. 46, no. 46, pp. 23 779–23 794, 2021.

[41] A. Babaytsev and L. Rabinskiy, “Design calculation technique for thick-walled composite constructions operating under high-speed loading,” *Periodico Tche Quimica*, vol. 16, no. 33, pp. 480–489, 2019.

[42] R. A. J. Weerts, “The impact behavior of thick-walled composite-overwrapped pressure vessels,” Ph.D. dissertation, Eindhoven University of Technology, 2021.

[43] P. Blanc-Vannet, “Burst pressure reduction of various thermoset composite pressure vessels after impact on the cylindrical part,” *Composite Structures*, vol. 160, pp. 706–711, 2017.

[44] DYNAmore GmbH, “Ls-dyna r14.1.0 released (2023/12),” 2023. [Online]. Available: https://www.dynasupport.com/news/ls-dyna-r14-1-0-released

[45] M. Vinot, N. Betz, T. Behling, L. Dauth, R. Jemmali, M. Holzapfel, and N. Toso, “Low-velocity impact on thick-wall wound composites for the sizing of hydrogen storage tanks,” in *4th International Conference on Impact Loading of Structures and Materials - ICILSM24*, Mai 2024. [Online]. Available: https://elib.dlr.de/204351/

[46] A. Turon, C. Dávila, P. Camanho, and J. Costa, “An engineering solution for mesh size effects in the simulation of delamination using cohesive zone models,” *Engineering Fracture Mechanics*, vol. 74, no. 10, pp. 1665–1682, 2007. [Online]. Available: https://www.sciencedirect.com/science/article/pii/S0013794406003808

A Configurations

The following tables show the configurations of all simulations with their parameter values. The following abbreviations are used for the tables: **CN**: Configuration Number, **ET**: Element Type, **IP**: Integration Points, **ES**: Element Size, **NE**: Number of Elements (radial), **S**: Solver, **ILM**: Inter-Layer Model, **LC**: Load Case, So: solid, Sh: shell, TSh: tshell, i: implicit, e:explicit, cc: cohesive contact, ce: cohesive element

Table A.1: Configurations Basic Investigation

CN	ET	IP	ES	NE	S		CN	ET	IP	ES	NE	S
1	So	1	1.5	8	i		31	Sh	8	2.5	1	i
2	So	1	1.5	16	i		32	Sh	16	2.5	1	i
3	So	1	1.5	24	i		33	Sh	24	2.5	1	i
4	So	1	2.0	8	i		34	Sh	8	3.0	1	i
5	So	1	2.0	16	i		35	Sh	16	3.0	1	i
6	So	1	2.0	24	i		36	Sh	24	3.0	1	i
7	So	1	2.5	8	i		37	Sh	8	3.5	1	i
8	So	1	2.5	16	i		38	Sh	16	3.5	1	i
9	So	1	2.5	24	i		39	Sh	24	3.5	1	i
10	So	1	3.0	8	i		40	Sh	8	4.0	1	i
11	So	1	3.0	16	i		41	Sh	16	4.0	1	i
12	So	1	3.0	24	i		42	Sh	24	4.0	1	i
13	So	1	3.5	8	i		43	Sh	8	5.0	1	i
14	So	1	3.5	16	i		44	Sh	16	5.0	1	i
15	So	1	3.5	24	i		45	Sh	24	5.0	1	i
16	So	1	4.0	8	i		46	Sh	8	6.0	1	i
17	So	1	4.0	16	i		47	Sh	16	6.0	1	i
18	So	1	4.0	24	i		48	Sh	24	6.0	1	i
19	So	1	5.0	8	i		49	TSh	2	1.5	4	i
20	So	1	5.0	16	i		50	TSh	2	1.5	8	i
21	So	1	5.0	24	i		51	TSh	2	1.5	16	i
22	So	1	6.0	8	i		52	TSh	2	1.5	24	i
23	So	1	6.0	16	i		53	TSh	4	1.5	2	i
24	So	1	6.0	24	i		54	TSh	4	1.5	4	i
25	Sh	8	1.5	1	i		55	TSh	4	1.5	8	i
26	Sh	16	1.5	1	i		56	TSh	4	1.5	16	i
27	Sh	24	1.5	1	i		57	TSh	4	1.5	24	i
28	Sh	8	2.0	1	i		58	TSh	8	1.5	1	i
29	Sh	16	2.0	1	i		59	TSh	8	1.5	2	i
30	Sh	24	2.0	1	i		60	TSh	8	1.5	4	i

CN	ET	IP	ES	NE	S		CN	ET	IP	ES	NE	S
61	TSh	8	1.5	8	i		101	TSh	24	2.0	16	i
62	TSh	8	1.5	16	i		102	TSh	24	2.0	24	i
63	TSh	8	1.5	24	i		103	TSh	2	2.5	4	i
64	TSh	16	1.5	1	i		104	TSh	2	2.5	8	i
65	TSh	16	1.5	2	i		105	TSh	2	2.5	16	i
66	TSh	16	1.5	4	i		106	TSh	2	2.5	24	i
67	TSh	16	1.5	8	i		107	TSh	4	2.5	2	i
68	TSh	16	1.5	16	i		108	TSh	4	2.5	4	i
69	TSh	16	1.5	24	i		109	TSh	4	2.5	8	i
70	TSh	24	1.5	1	i		110	TSh	4	2.5	16	i
71	TSh	24	1.5	2	i		111	TSh	4	2.5	24	i
72	TSh	24	1.5	4	i		112	TSh	8	2.5	1	i
73	TSh	24	1.5	8	i		113	TSh	8	2.5	2	i
74	TSh	24	1.5	16	i		114	TSh	8	2.5	4	i
75	TSh	24	1.5	24	i		115	TSh	8	2.5	8	i
76	TSh	2	2.0	4	i		116	TSh	8	2.5	16	i
77	TSh	2	2.0	8	i		117	TSh	8	2.5	24	i
78	TSh	2	2.0	16	i		118	TSh	16	2.5	1	i
79	TSh	2	2.0	24	i		119	TSh	16	2.5	2	i
80	TSh	4	2.0	2	i		120	TSh	16	2.5	4	i
81	TSh	4	2.0	4	i		121	TSh	16	2.5	8	i
82	TSh	4	2.0	8	i		122	TSh	16	2.5	16	i
83	TSh	4	2.0	16	i		123	TSh	16	2.5	24	i
84	TSh	4	2.0	24	i		124	TSh	24	2.5	1	i
85	TSh	8	2.0	1	i		125	TSh	24	2.5	2	i
86	TSh	8	2.0	2	i		126	TSh	24	2.5	4	i
87	TSh	8	2.0	4	i		127	TSh	24	2.5	8	i
88	TSh	8	2.0	8	i		128	TSh	24	2.5	16	i
89	TSh	8	2.0	16	i		129	TSh	24	2.5	24	i
90	TSh	8	2.0	24	i		130	TSh	2	3.0	4	i
91	TSh	16	2.0	1	i		131	TSh	2	3.0	8	i
92	TSh	16	2.0	2	i		132	TSh	2	3.0	16	i
93	TSh	16	2.0	4	i		133	TSh	2	3.0	24	i
94	TSh	16	2.0	8	i		134	TSh	4	3.0	2	i
95	TSh	16	2.0	16	i		135	TSh	4	3.0	4	i
96	TSh	16	2.0	24	i		136	TSh	4	3.0	8	i
97	TSh	24	2.0	1	i		137	TSh	4	3.0	16	i
98	TSh	24	2.0	2	i		138	TSh	4	3.0	24	i
99	TSh	24	2.0	4	i		139	TSh	8	3.0	1	i
100	TSh	24	2.0	8	i		140	TSh	8	3.0	2	i

CN	ET	IP	ES	NE	S		CN	ET	IP	ES	NE	S
141	TSh	8	3.0	4	i		181	TSh	24	3.5	8	i
142	TSh	8	3.0	8	i		182	TSh	24	3.5	16	i
143	TSh	8	3.0	16	i		183	TSh	24	3.5	24	i
144	TSh	8	3.0	24	i		184	TSh	2	4.0	4	i
145	TSh	16	3.0	1	i		185	TSh	2	4.0	8	i
146	TSh	16	3.0	2	i		186	TSh	2	4.0	16	i
147	TSh	16	3.0	4	i		187	TSh	2	4.0	24	i
148	TSh	16	3.0	8	i		188	TSh	4	4.0	2	i
149	TSh	16	3.0	16	i		189	TSh	4	4.0	4	i
150	TSh	16	3.0	24	i		190	TSh	4	4.0	8	i
151	TSh	24	3.0	1	i		191	TSh	4	4.0	16	i
152	TSh	24	3.0	2	i		192	TSh	4	4.0	24	i
153	TSh	24	3.0	4	i		193	TSh	8	4.0	1	i
154	TSh	24	3.0	8	i		194	TSh	8	4.0	2	i
155	TSh	24	3.0	16	i		195	TSh	8	4.0	4	i
156	TSh	24	3.0	24	i		196	TSh	8	4.0	8	i
157	TSh	2	3.5	4	i		197	TSh	8	4.0	16	i
158	TSh	2	3.5	8	i		198	TSh	8	4.0	24	i
159	TSh	2	3.5	16	i		199	TSh	16	4.0	1	i
160	TSh	2	3.5	24	i		200	TSh	16	4.0	2	i
161	TSh	4	3.5	2	i		201	TSh	16	4.0	4	i
162	TSh	4	3.5	4	i		202	TSh	16	4.0	8	i
163	TSh	4	3.5	8	i		203	TSh	16	4.0	16	i
164	TSh	4	3.5	16	i		204	TSh	16	4.0	24	i
165	TSh	4	3.5	24	i		205	TSh	24	4.0	1	i
166	TSh	8	3.5	1	i		206	TSh	24	4.0	2	i
167	TSh	8	3.5	2	i		207	TSh	24	4.0	4	i
168	TSh	8	3.5	4	i		208	TSh	24	4.0	8	i
169	TSh	8	3.5	8	i		209	TSh	24	4.0	16	i
170	TSh	8	3.5	16	i		210	TSh	24	4.0	24	i
171	TSh	8	3.5	24	i		211	TSh	2	5.0	4	i
172	TSh	16	3.5	1	i		212	TSh	2	5.0	8	i
173	TSh	16	3.5	2	i		213	TSh	2	5.0	16	i
174	TSh	16	3.5	4	i		214	TSh	2	5.0	24	i
175	TSh	16	3.5	8	i		215	TSh	4	5.0	2	i
176	TSh	16	3.5	16	i		216	TSh	4	5.0	4	i
177	TSh	16	3.5	24	i		217	TSh	4	5.0	8	i
178	TSh	24	3.5	1	i		218	TSh	4	5.0	16	i
179	TSh	24	3.5	2	i		219	TSh	4	5.0	24	i
180	TSh	24	3.5	4	i		220	TSh	8	5.0	1	i

CN	ET	IP	ES	NE	S		CN	ET	IP	ES	NE	S
221	TSh	8	5.0	2	i		261	TSh	24	6.0	4	i
222	TSh	8	5.0	4	i		262	TSh	24	6.0	8	i
223	TSh	8	5.0	8	i		263	TSh	24	6.0	16	i
224	TSh	8	5.0	16	i		264	TSh	24	6.0	24	i
225	TSh	8	5.0	24	i		265	So	1	2.0	8	e
226	TSh	16	5.0	1	i		266	So	1	2.0	16	e
227	TSh	16	5.0	2	i		267	So	1	4.0	8	e
228	TSh	16	5.0	4	i		268	So	1	4.0	16	e
229	TSh	16	5.0	8	i		269	So	1	6.0	8	e
230	TSh	16	5.0	16	i		270	So	1	6.0	16	e
231	TSh	16	5.0	24	i		271	Sh	8	2.0	1	e
232	TSh	24	5.0	1	i		272	Sh	16	2.0	1	e
233	TSh	24	5.0	2	i		273	Sh	8	4.0	1	e
234	TSh	24	5.0	4	i		274	Sh	16	4.0	1	e
235	TSh	24	5.0	8	i		275	Sh	8	6.0	1	e
236	TSh	24	5.0	16	i		276	Sh	16	6.0	1	e
237	TSh	24	5.0	24	i		277	TSh	2	2.0	4	e
238	TSh	2	6.0	4	i		278	TSh	2	2.0	8	e
239	TSh	2	6.0	8	i		279	TSh	2	2.0	16	e
240	TSh	2	6.0	16	i		280	TSh	4	2.0	4	e
241	TSh	2	6.0	24	i		281	TSh	4	2.0	8	e
242	TSh	4	6.0	2	i		282	TSh	4	2.0	16	e
243	TSh	4	6.0	4	i		283	TSh	8	2.0	4	e
244	TSh	4	6.0	8	i		284	TSh	8	2.0	8	e
245	TSh	4	6.0	16	i		285	TSh	8	2.0	16	e
246	TSh	4	6.0	24	i		286	TSh	16	2.0	4	e
247	TSh	8	6.0	1	i		287	TSh	16	2.0	8	e
248	TSh	8	6.0	2	i		288	TSh	16	2.0	16	e
249	TSh	8	6.0	4	i		289	TSh	2	6.0	4	e
250	TSh	8	6.0	8	i		290	TSh	2	6.0	8	e
251	TSh	8	6.0	16	i		291	TSh	2	6.0	16	e
252	TSh	8	6.0	24	i		292	TSh	4	6.0	4	e
253	TSh	16	6.0	1	i		293	TSh	4	6.0	8	e
254	TSh	16	6.0	2	i		294	TSh	4	6.0	16	e
255	TSh	16	6.0	4	i		295	TSh	8	6.0	4	e
256	TSh	16	6.0	8	i		296	TSh	8	6.0	8	e
257	TSh	16	6.0	16	i		297	TSh	8	6.0	16	e
258	TSh	16	6.0	24	i		298	TSh	16	6.0	4	e
259	TSh	24	6.0	1	i		299	TSh	16	6.0	8	e
260	TSh	24	6.0	2	i		300	TSh	16	6.0	16	e

Table A.2: Configurations Burst Pressure

CN	ET	IP	ES	NE	S		CN	ET	IP	ES	NE	S
301	So	1	2.0	8	i		341	TSh	4	6.0	8	i
302	So	1	2.0	16	i		342	TSh	4	6.0	16	i
303	So	1	4.0	8	i		343	TSh	8	6.0	4	i
304	So	1	4.0	16	i		344	TSh	8	6.0	8	i
305	So	1	6.0	8	i		345	TSh	8	6.0	16	i
306	So	1	6.0	16	i		346	TSh	16	6.0	4	i
307	Sh	8	2.0	1	i		347	TSh	16	6.0	8	i
308	Sh	16	2.0	1	i		348	TSh	16	6.0	16	i
309	Sh	8	4.0	1	i		349	So	1	2.0	8	e
310	Sh	16	4.0	1	i		350	So	1	2.0	16	e
311	Sh	8	6.0	1	i		351	So	1	4.0	8	e
312	Sh	16	6.0	1	i		352	So	1	4.0	16	e
313	TSh	2	2.0	4	i		353	So	1	6.0	8	e
314	TSh	2	2.0	8	i		354	So	1	6.0	16	e
315	TSh	2	2.0	16	i		355	Sh	8	2.0	1	e
316	TSh	4	2.0	4	i		356	Sh	16	2.0	1	e
317	TSh	4	2.0	8	i		357	Sh	8	4.0	1	e
318	TSh	4	2.0	16	i		358	Sh	16	4.0	1	e
319	TSh	8	2.0	4	i		359	Sh	8	6.0	1	e
320	TSh	8	2.0	8	i		360	Sh	16	6.0	1	e
321	TSh	8	2.0	16	i		361	TSh	2	2.0	4	e
322	TSh	16	2.0	4	i		362	TSh	2	2.0	8	e
323	TSh	16	2.0	8	i		363	TSh	2	2.0	16	e
324	TSh	16	2.0	16	i		364	TSh	4	2.0	4	e
325	TSh	2	4.0	4	i		365	TSh	4	2.0	8	e
326	TSh	2	4.0	8	i		366	TSh	4	2.0	16	e
327	TSh	2	4.0	16	i		367	TSh	8	2.0	4	e
328	TSh	4	4.0	4	i		368	TSh	8	2.0	8	e
329	TSh	4	4.0	8	i		369	TSh	8	2.0	16	e
330	TSh	4	4.0	16	i		370	TSh	2	6.0	4	e
331	TSh	8	4.0	4	i		371	TSh	2	6.0	8	e
332	TSh	8	4.0	8	i		372	TSh	2	6.0	16	e
333	TSh	8	4.0	16	i		373	TSh	4	6.0	4	e
334	TSh	16	4.0	4	i		374	TSh	4	6.0	8	e
335	TSh	16	4.0	8	i		375	TSh	4	6.0	16	e
336	TSh	16	4.0	16	i		376	TSh	8	6.0	4	e
337	TSh	2	6.0	4	i		377	TSh	8	6.0	8	e
338	TSh	2	6.0	8	i		378	TSh	8	6.0	16	e
339	TSh	2	6.0	16	i							
340	TSh	4	6.0	4	i							

Table A.3: Configurations Gas Model

CN	ET	IP	ES	NE	S		CN	ET	IP	ES	NE	S
401	So	1	1.5	8	i		441	TSh	4	1.5	4	e
402	So	1	1.5	16	i		442	TSh	8	1.5	4	e
403	So	1	3.0	8	i		443	TSh	2	1.5	8	e
404	So	1	3.0	16	i		444	TSh	4	1.5	8	e
405	So	1	6.0	8	i		445	TSh	8	1.5	8	e
406	So	1	6.0	16	i		446	TSh	2	1.5	16	e
407	So	1	1.5	8	e		447	TSh	4	1.5	16	e
408	So	1	1.5	16	e		448	TSh	8	1.5	16	e
409	So	1	3.0	8	e		449	TSh	2	3.0	4	e
410	So	1	3.0	16	e		450	TSh	4	3.0	4	e
411	So	1	6.0	8	e		451	TSh	8	3.0	4	e
412	So	1	6.0	16	e		452	TSh	2	3.0	8	e
413	TSh	2	1.5	4	i		453	TSh	4	3.0	8	e
414	TSh	4	1.5	4	i		454	TSh	8	3.0	8	e
415	TSh	8	1.5	4	i		455	TSh	2	3.0	16	e
416	TSh	2	1.5	8	i		456	TSh	4	3.0	16	e
417	TSh	4	1.5	8	i		457	TSh	8	3.0	16	e
418	TSh	8	1.5	8	i		458	TSh	2	6.0	4	e
419	TSh	2	1.5	16	i		459	TSh	4	6.0	4	e
420	TSh	4	1.5	16	i		460	TSh	8	6.0	4	e
421	TSh	8	1.5	16	i		461	TSh	2	6.0	8	e
422	TSh	2	3.0	4	i		462	TSh	4	6.0	8	e
423	TSh	4	3.0	4	i		463	TSh	8	6.0	8	e
424	TSh	8	3.0	4	i		464	TSh	2	6.0	16	e
425	TSh	2	3.0	8	i		465	TSh	4	6.0	16	e
426	TSh	4	3.0	8	i		466	TSh	8	6.0	16	e
427	TSh	8	3.0	8	i							
428	TSh	2	3.0	16	i							
429	TSh	4	3.0	16	i							
430	TSh	8	3.0	16	i							
431	TSh	2	6.0	4	i							
432	TSh	4	6.0	4	i							
433	TSh	8	6.0	4	i							
434	TSh	2	6.0	8	i							
435	TSh	4	6.0	8	i							
436	TSh	8	6.0	8	i							
437	TSh	2	6.0	16	i							
438	TSh	4	6.0	16	i							
439	TSh	8	6.0	16	i							
440	TSh	2	1.5	4	e							

Table A.4: Configurations Inter-Layer Model

CN	ET	IP	ES	NE	ILM	LC
501	So	1	1.5	8	cc	impact
502	So	1	1.5	8	ce	impact
503	So	1	3.0	8	cc	impact
504	So	1	3.0	8	ce	impact
505	So	1	6.0	8	cc	impact
506	So	1	6.0	8	ce	impact
507	So	1	3.0	16	cc	impact
508	So	1	3.0	16	ce	impact
509	TSh	2	3.0	4	cc	impact
510	TSh	2	3.0	4	ce	impact
511	TSh	4	3.0	8	cc	impact
512	TSh	4	3.0	8	ce	impact
513	TSh	2	3.0	8	cc	impact
514	TSh	2	3.0	8	ce	impact
515	TSh	4	1.5	8	cc	impact
516	TSh	4	1.5	8	ce	impact
517	TSh	4	3.0	8	cc	impact
518	TSh	4	3.0	8	ce	impact
519	TSh	4	6.0	8	cc	impact
520	TSh	4	6.0	8	ce	impact
521	So	1	1.5	8	cc	load + impact
522	So	1	1.5	8	ce	load + impact
523	So	1	1.5	8	cc	gas + impact
524	So	1	1.5	8	ce	gas + impact
525	TSh	4	1.5	8	cc	load + impact
526	TSh	4	1.5	8	ce	load + impact
527	TSh	4	1.5	8	cc	gas + impact
528	TSh	4	1.5	8	ce	gas + impact

B Simulation Workflow

The next page shows the workflow from the creation of the mesh from the input files and the model parameters to the finished diagram. The square boxes represent Python scripts and the ellipses input and output files. The input files are highlighted in light grey and the output files in blue.

The script for mesh generation (model_generation.py) is written in such a way that it can be used for all analyses. In contrast, the evaluation scripts (postprocessing.py and data_analysis.py) are adapted to the data to be analysed. The LS-run.py script contains the model parameters (interaction with mesh generation script) and automatically starts the LS-DYNA simulation after the mesh generation.

The input files for the mesh generation contain information about the geometry and the physical layer structure. The input file for the simulation (main.key) contains or references all the information required for the simulation.

The generally usable file types .csv and .json are used for the result data files. They allow the data to be used with as many different programmes as possible.

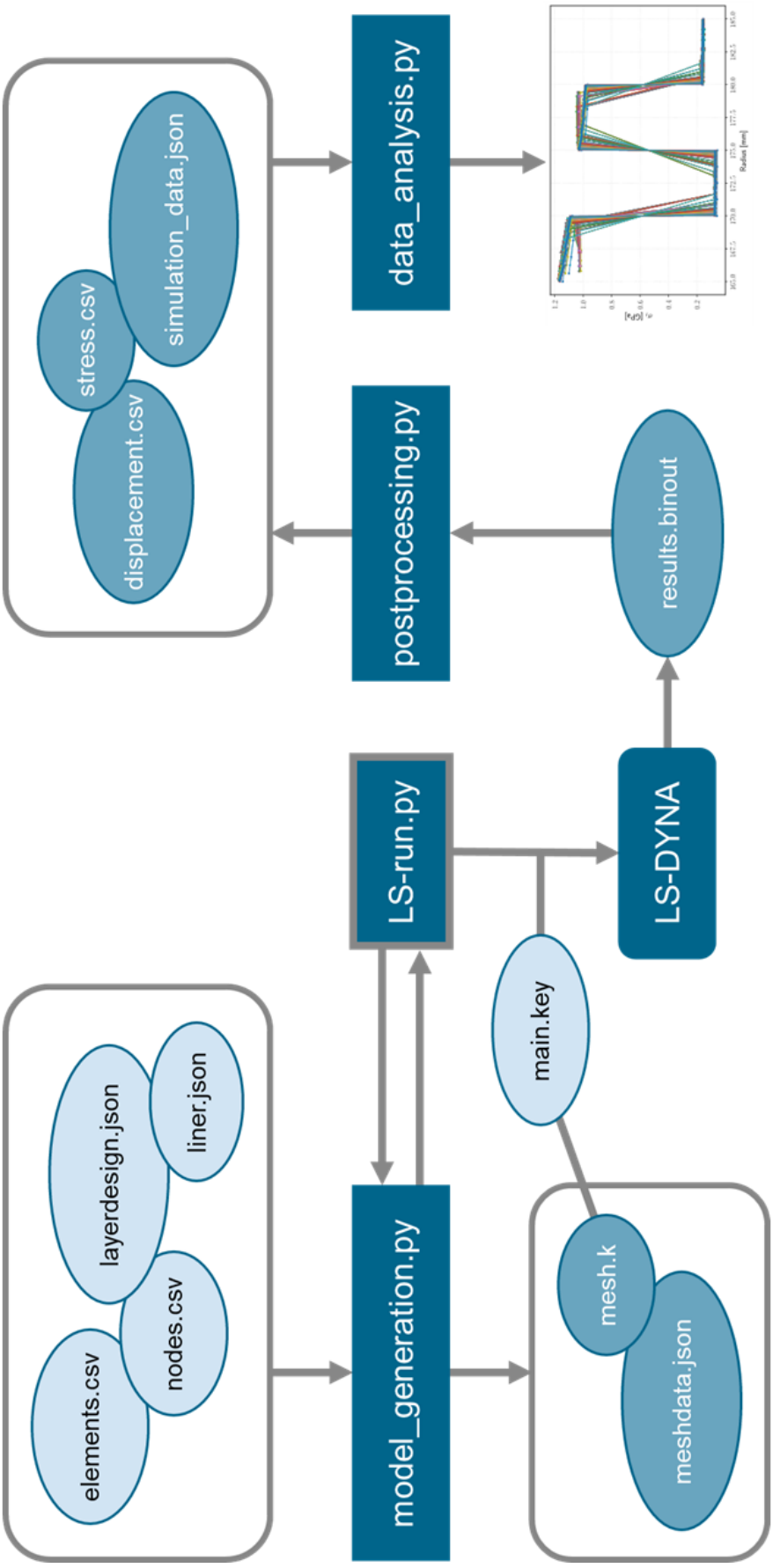

Figure B.1: Workflow diagram from input files to data diagram

C Basic Investigation Diagrams

Supplementary diagrams for the basic investigation are shown below. The individual red curve represents the reference values. The model parameters used are indicated in the image description and, where applicable, in the legend. Due to the number of simulations and the fact that the results all match each other, no legend is provided.

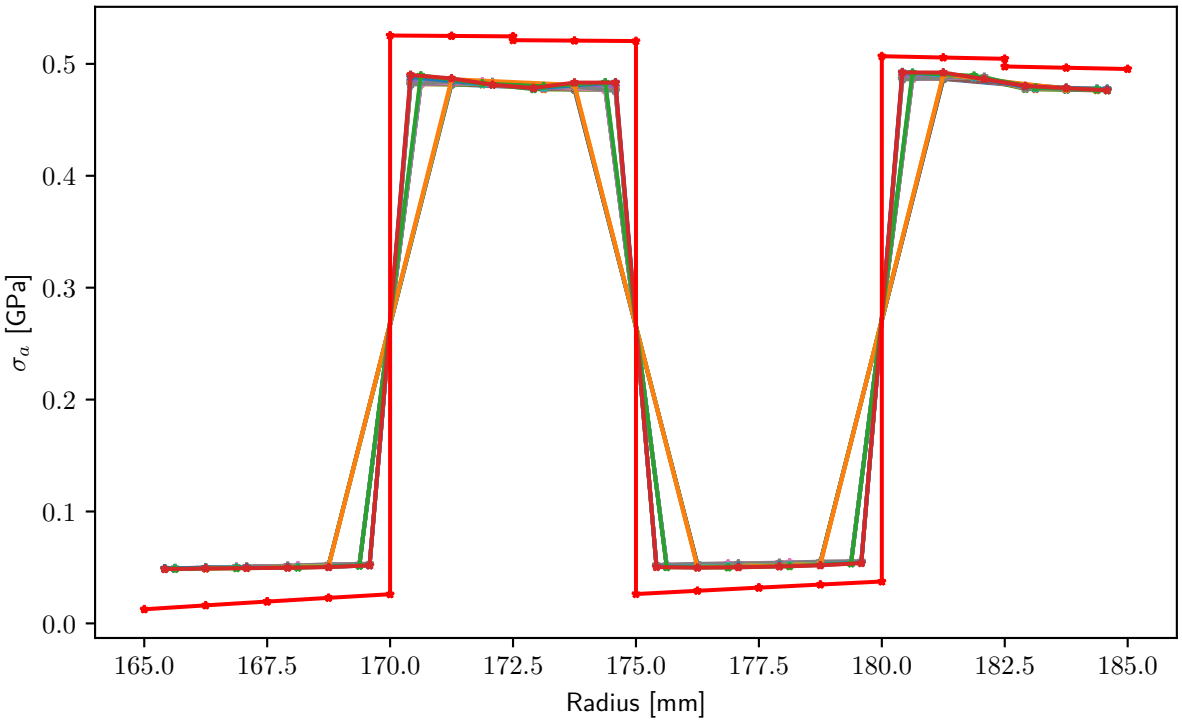

Figure C.1: Axial stress over the radius (element type: solid, solver: implicit)

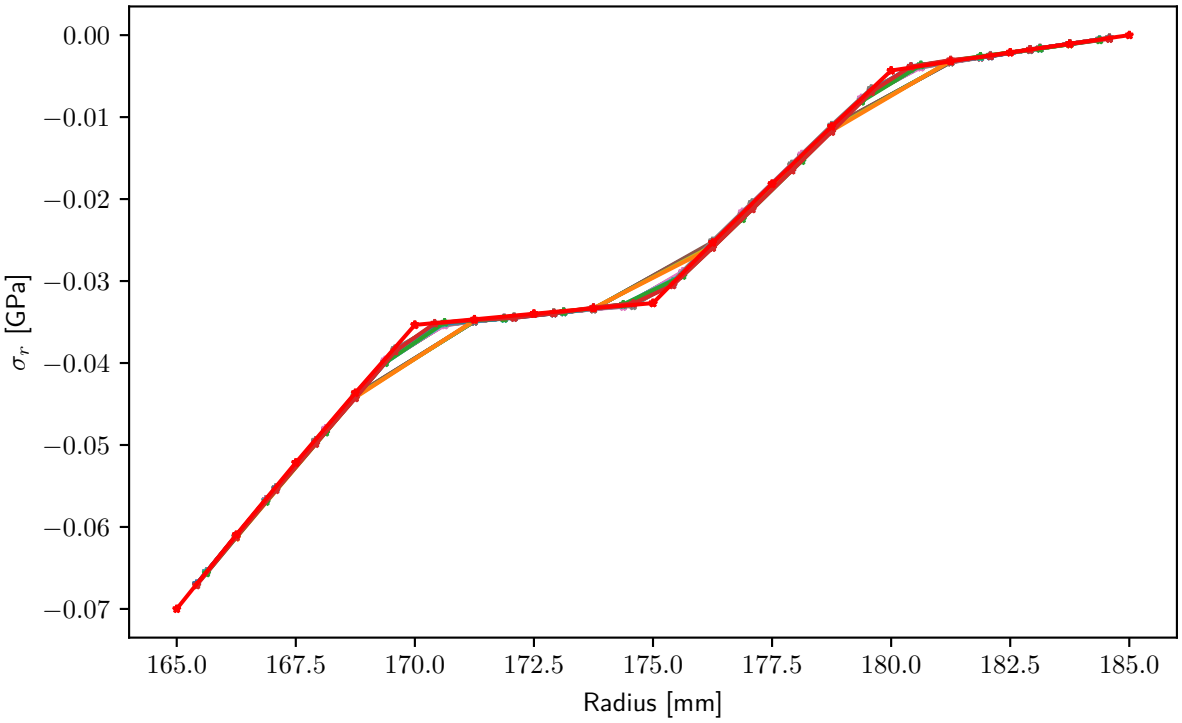

Figure C.2: Radial stress over the radius (element type: solid, solver: implicit)

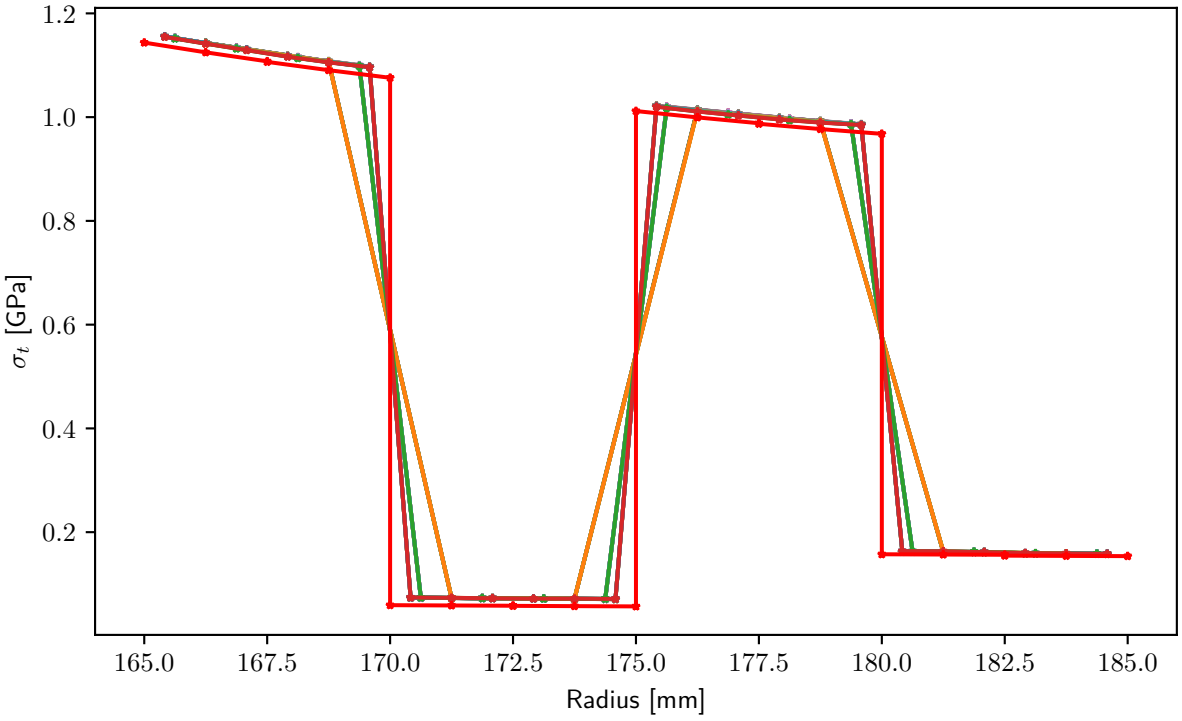

Figure C.3: Tangential stress over the radius (element type: solid, solver: implicit)

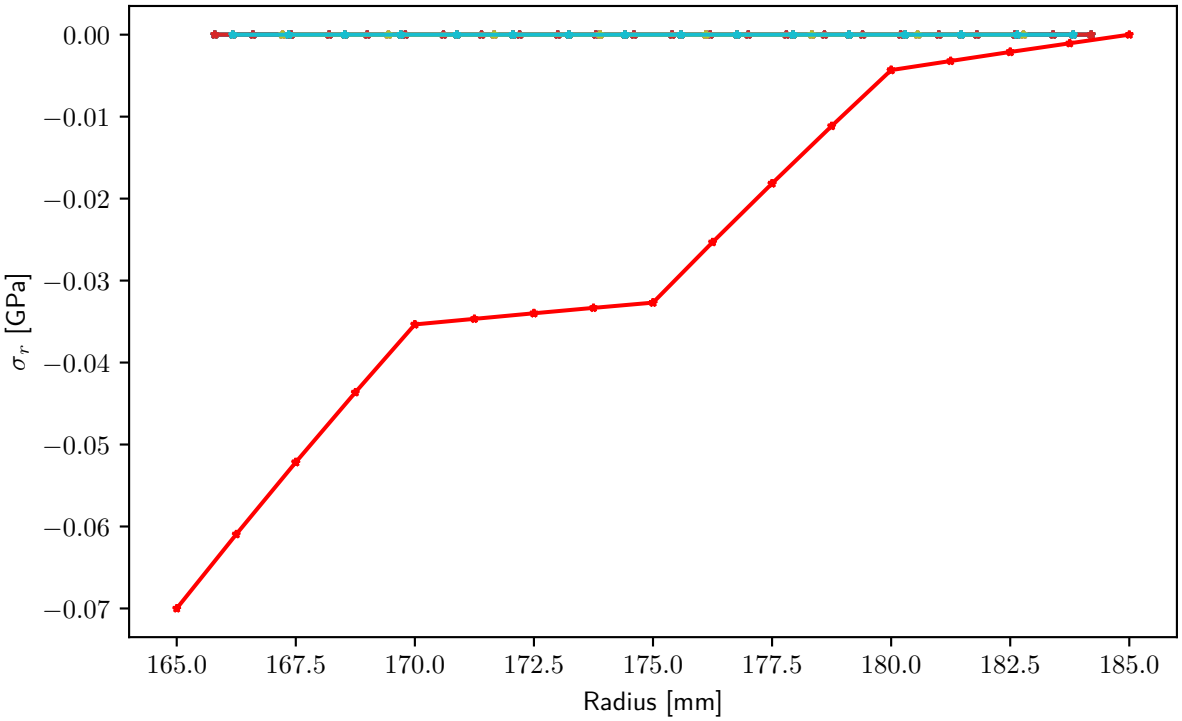

Figure C.4: Radial stress over the radius (element type: shell)

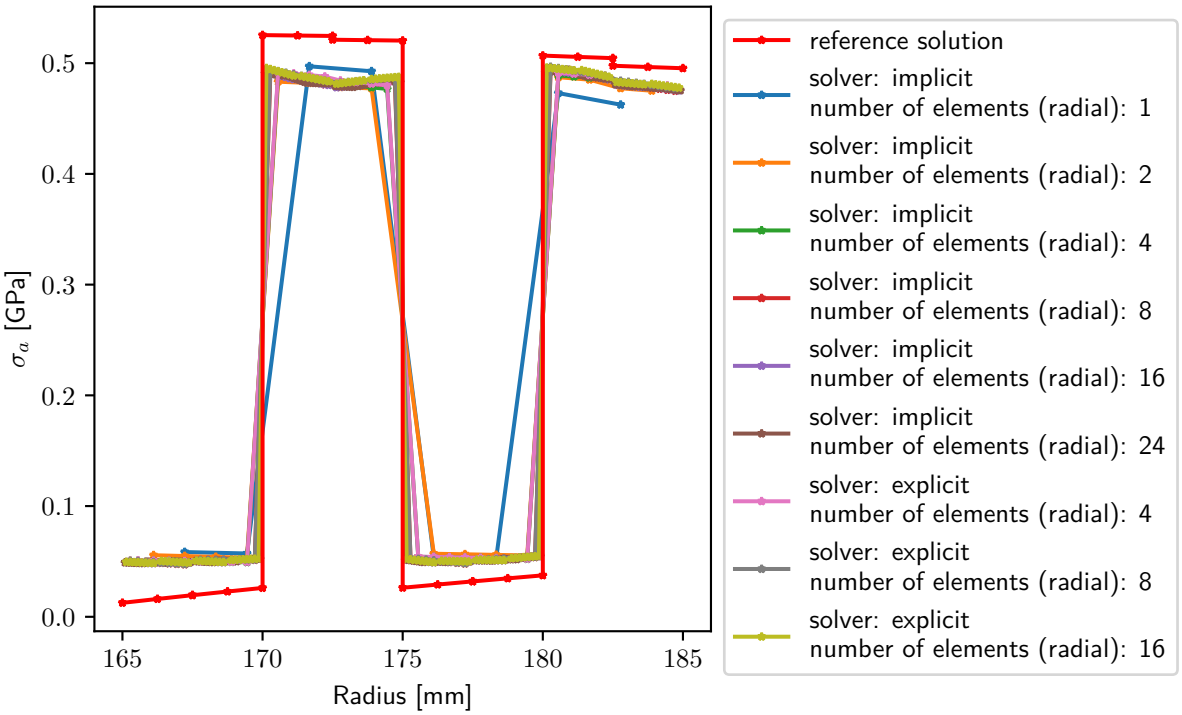

Figure C.5: Axial stress over the radius (element type: tshell, element size: 6.0, number of integration points: 8)

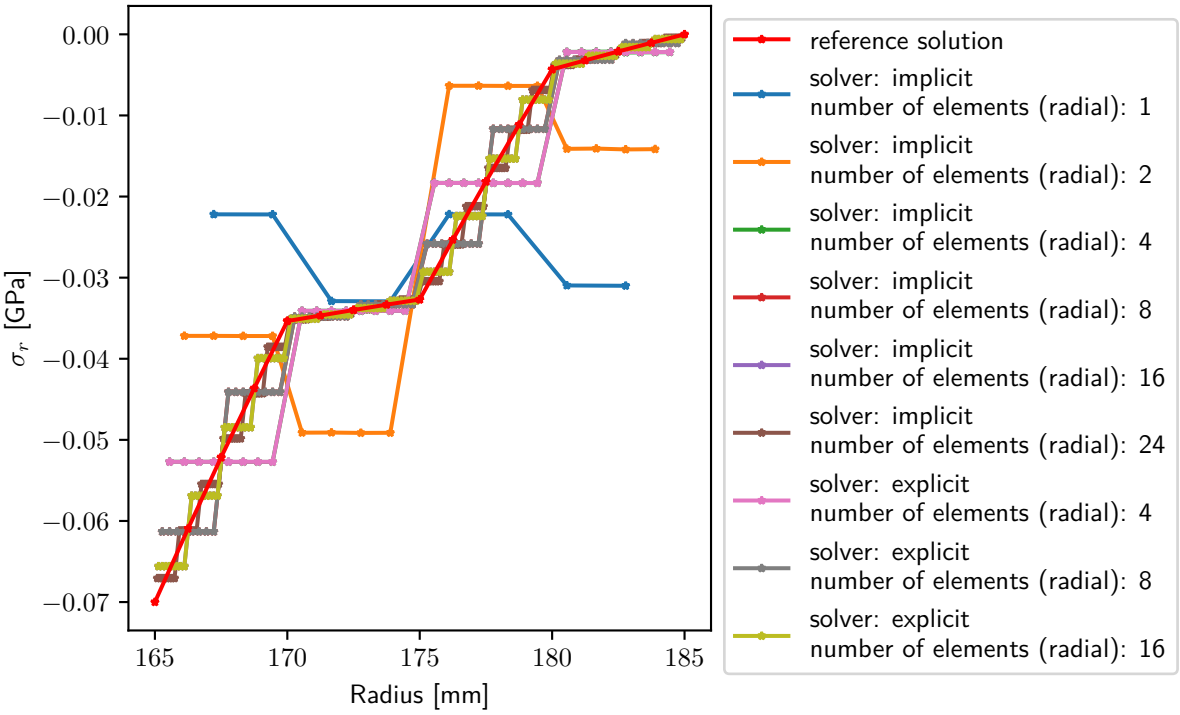

Figure C.6: Radial stress over the radius (element type: tshell, element size: 6.0, number of integration points: 8)

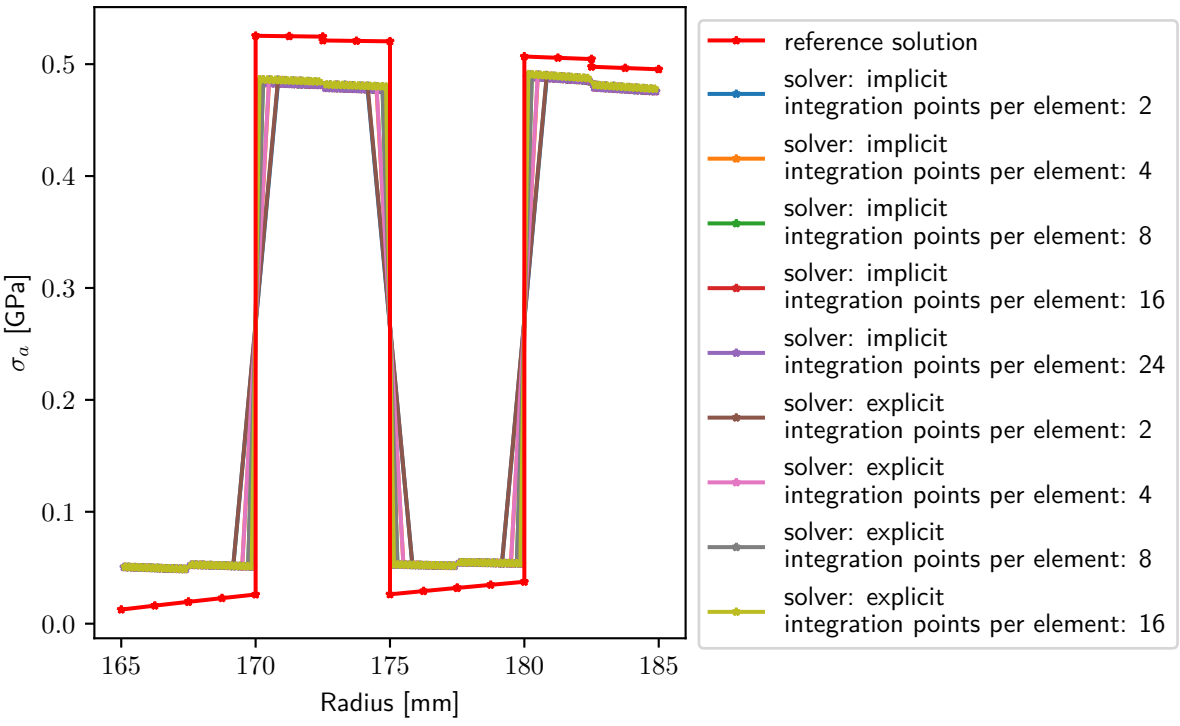

Figure C.7: Axial stress over the radius (element type: tshell, element size: 2.0, number of radial elements: 8)

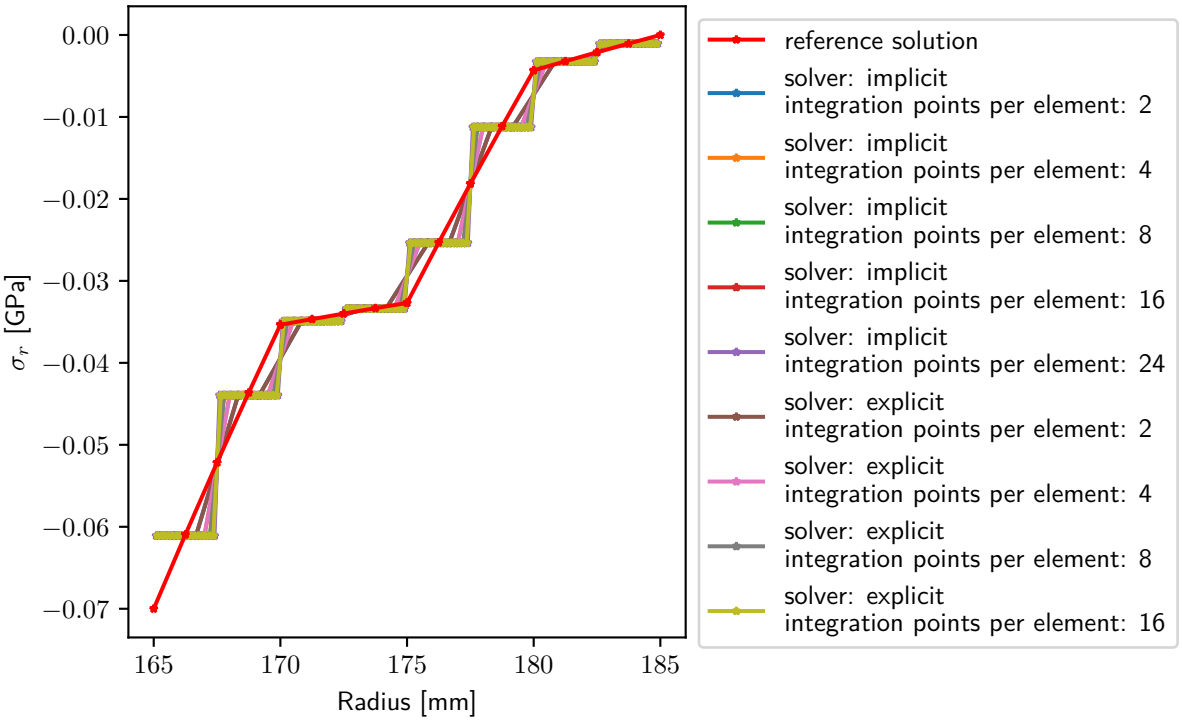

Figure C.8: Radial stress over the radius (element type: tshell, element size: 2.0, number of radial elements: 8)

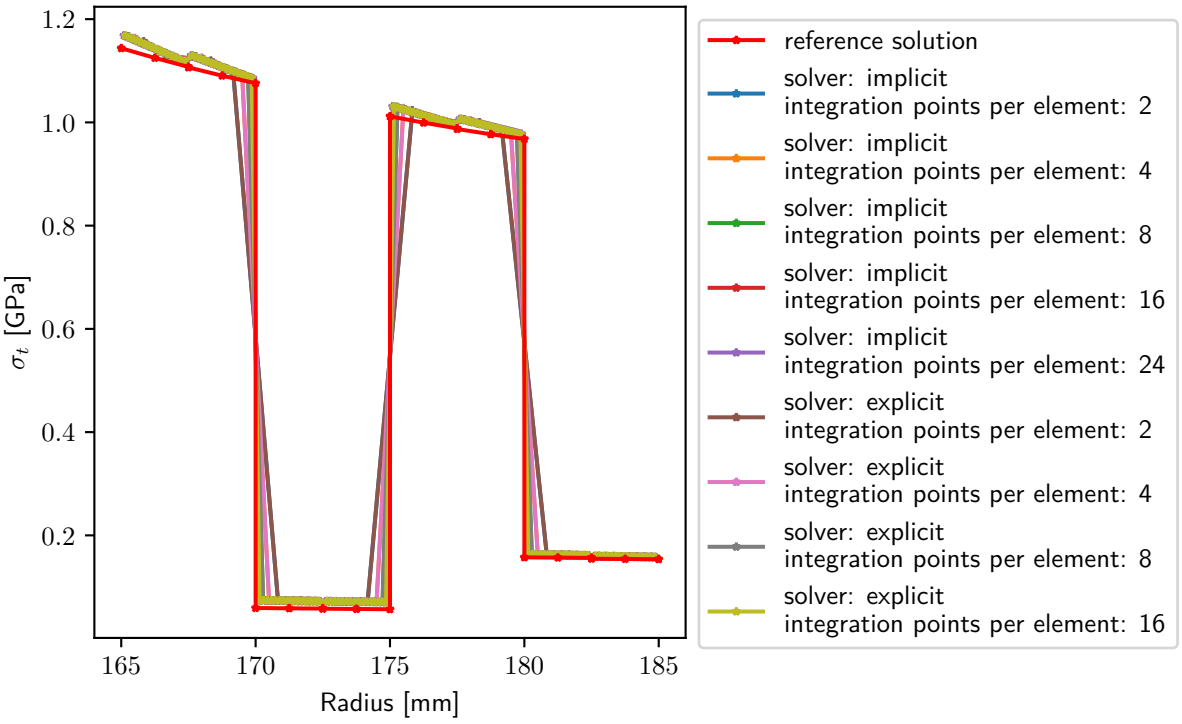

Figure C.9: Tangential stress over the radius (element type: tshell, element size: 2.0, number of radial elements: 8)

D Gas Model Diagrams

In the diagrams in this section, the reference values from the software tool are shown with the blue line. The red line represents the results of configuration 75. Configuration 75 is taken as the value, which represents the results from the basic investigation best. The simulation results of the models which model the internal pressure as a gas are shown as dots. Due to the number of simulations and the fact that the results all match each other, no legend is provided.

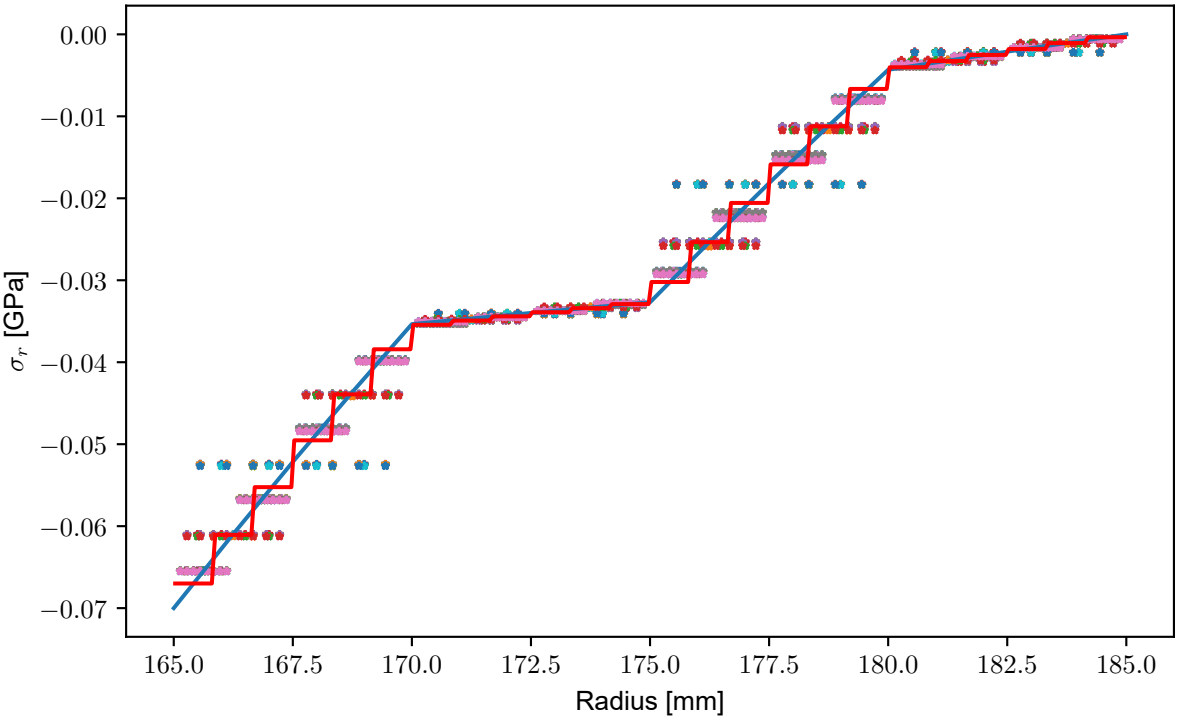

Figure D.1: Radial stress over the radius (all simulations of gas model investigation)

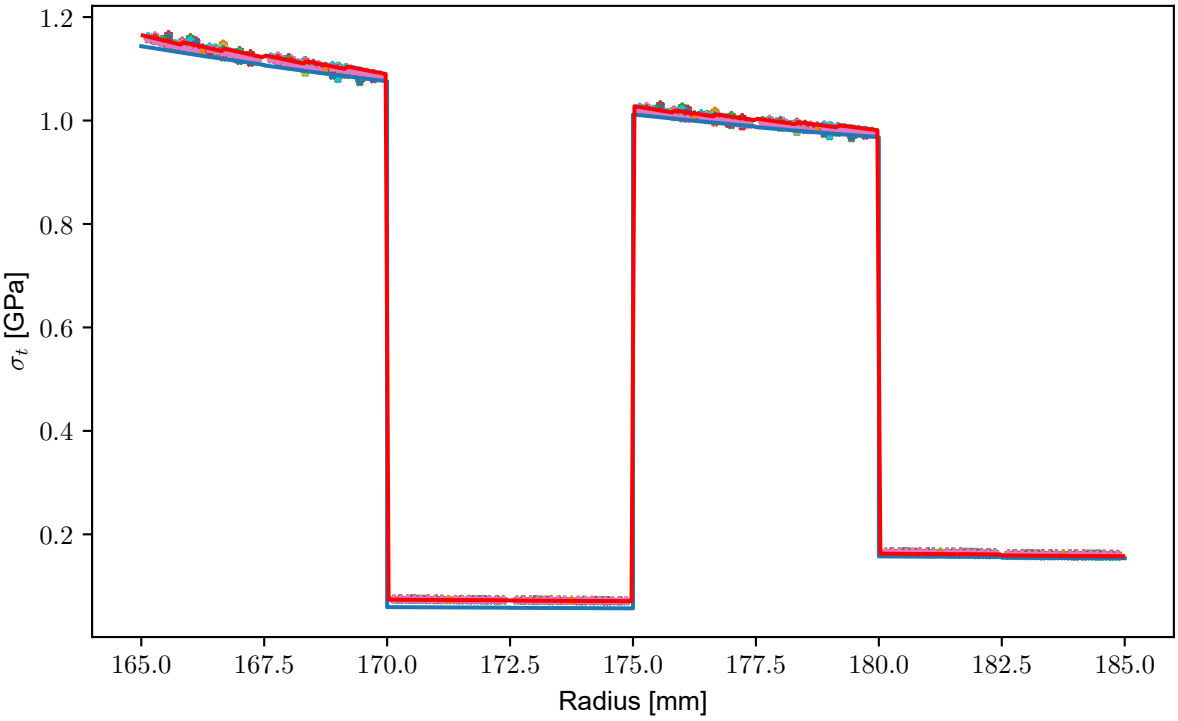

Figure D.2: Tangential stress over the radius (all simulations of gas model investigation)

E Inter-Layer Model Diagrams

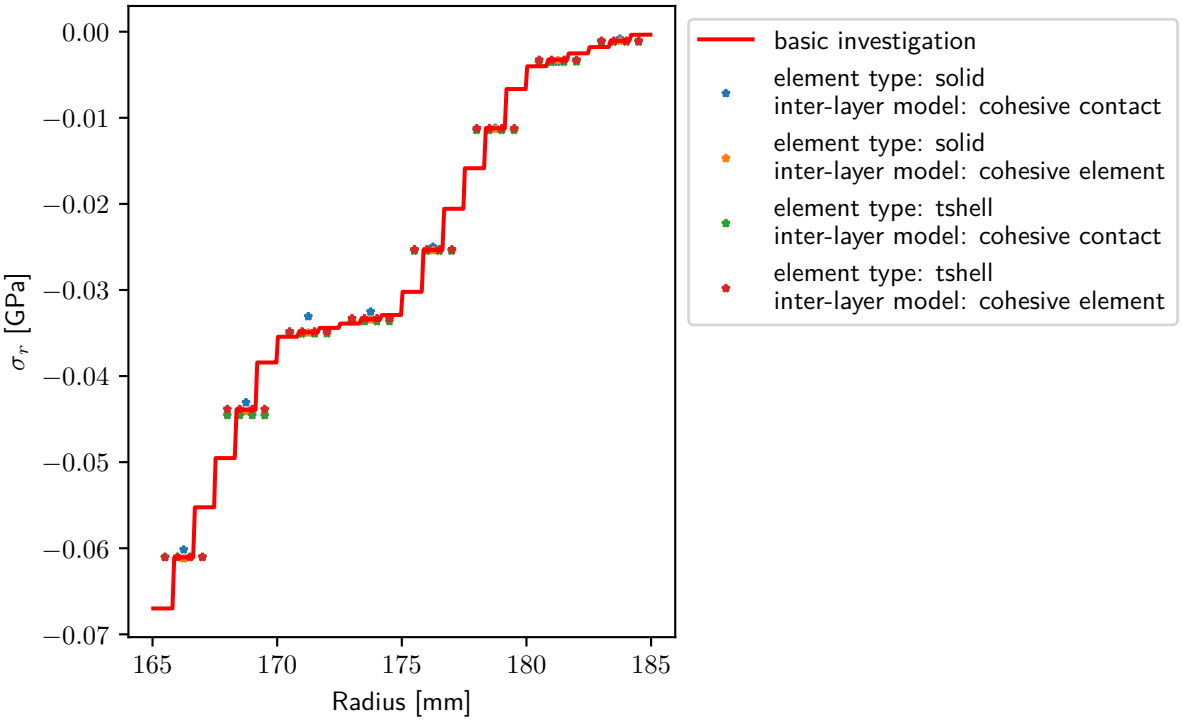

Figure E.1: Radial stress comparison (with legend)

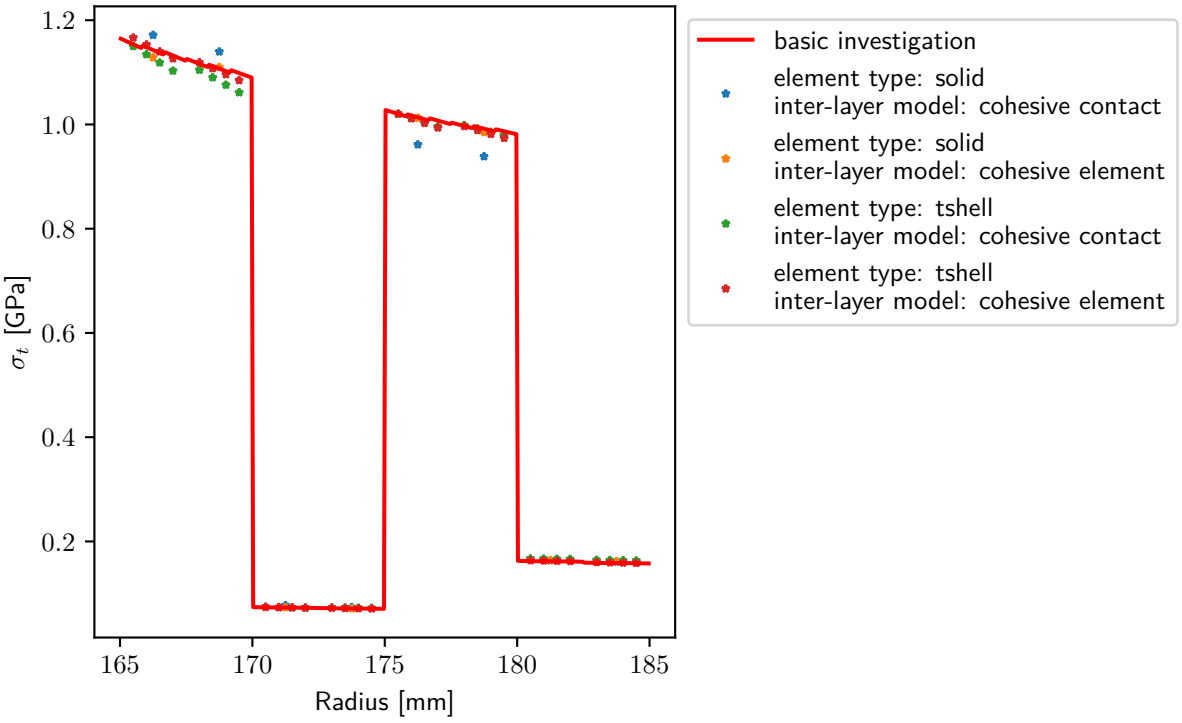

Figure E.2: Tangential stress comparison

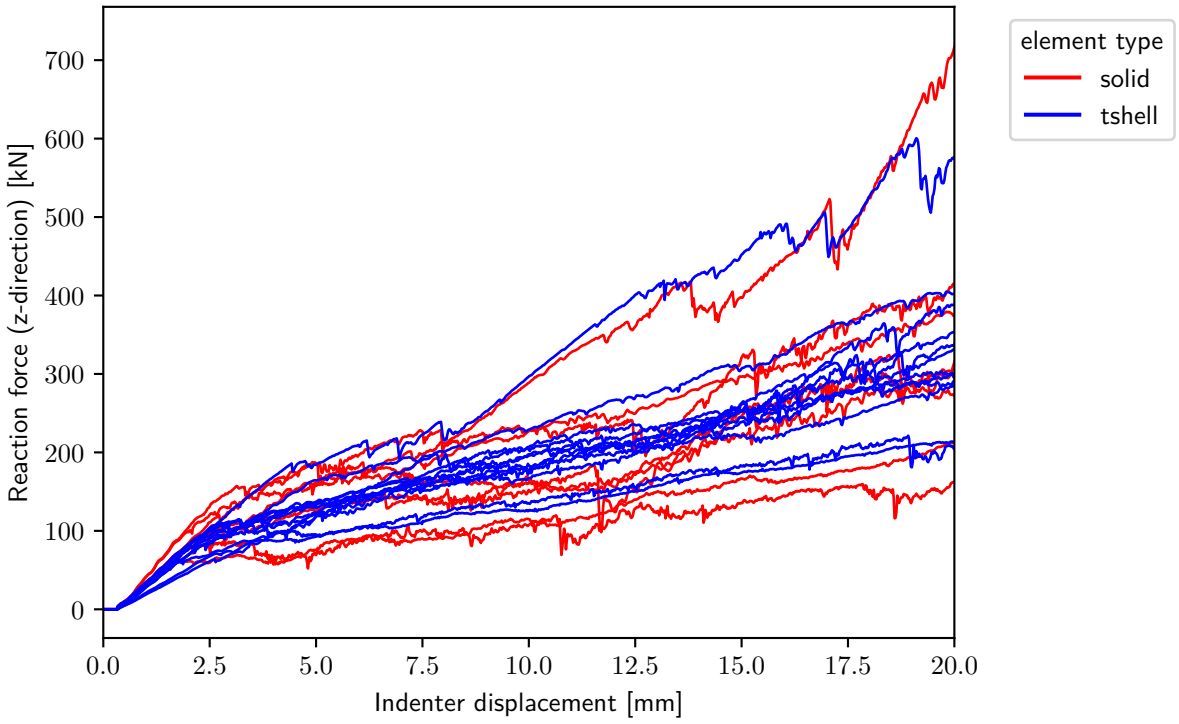

Figure E.3: Reaction force on indenter (coloured by element type)

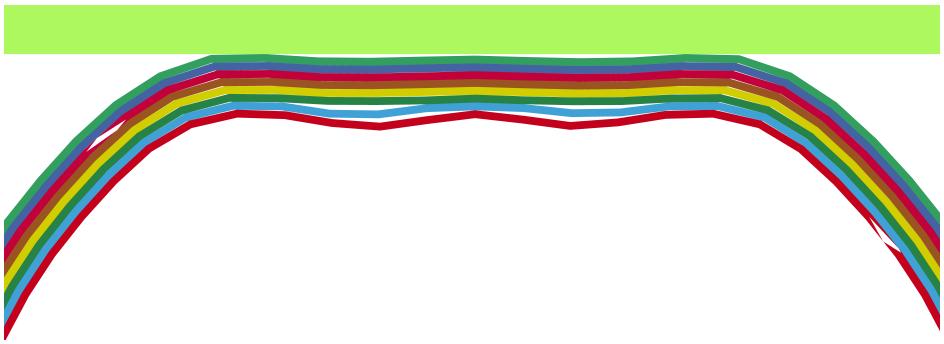

Figure E.4: Cross section deformation (element type: solid; element size: 1.5; ILM: cohesive contact)

F Tank Model Diagrams

Table F.1: Stacking sequence tank (cylindrical part)

Ply number	Fibre angle		Ply number	Fibre angle		Ply number	Fibre angle
1	9.101091		31	19.480609		61	39.967927
2	89.2991823		32	20.378664		62	49.091504
3	9.213804		33	89.33057731		63	50.366017
4	89.30129638		34	21.394901		64	89.35928009
5	9.400049		35	21.595428		65	51.26681
6	9.868699		36	89.33346691		66	89.36104759
7	10.00004		37	89.33442457		67	54.543435
8	89.30548651		38	21.704259		68	55.114809
9	10.073649		39	22.155054		69	55.941368
10	89.30756278		40	89.33728112		70	56.794901
11	10.103021		41	23.525946		71	89.36542398
12	10.24334		42	25.792814		72	58.272145
13	89.31065402		43	26.472679		73	89.36715779
14	10.801294		44	89.34105192		74	58.722925
15	10.898565		45	27.465909		75	61.391799
16	13.756965		46	27.778305		76	64.344556
17	13.873304		47	28.379009		77	89.37059715
18	89.3157452		48	29.649209		78	89.37145116
19	14.792049		49	89.34570551		79	65.781019
20	89.31776068		50	30.625169		80	89.37315224
21	14.938583		51	89.34754859		81	66.449079
22	16.53946		52	30.864638		82	89.37484414
23	89.32076173		53	89.34938132		83	66.637571
24	16.667766		54	31.274038		84	67.156184
25	16.771798		55	31.478535		85	69.849666
26	17.864089		56	89.35211119		86	70
27	89.3247223		57	32.580781		87	70
28	18.074152		58	33.204857			
29	18.451329		59	34.185268			
30	89.32766256		60	89.35571558			

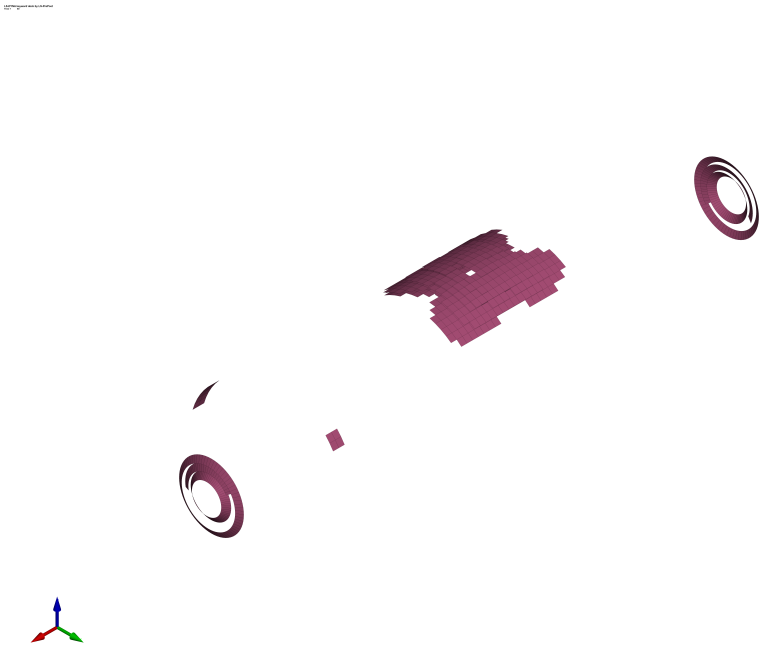

Figure F.1: Deleted elements (element type: tshell; combined layers: 4)

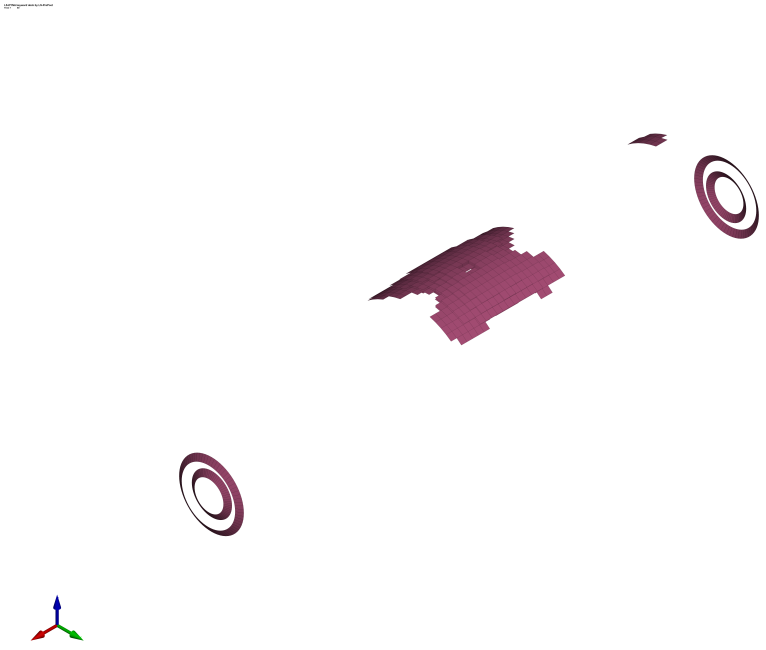

Figure F.2: Deleted elements (element type: tshell; combined layers: 8)

Figure F.3: Deleted elements (element type: tshell; combined layers: 16)

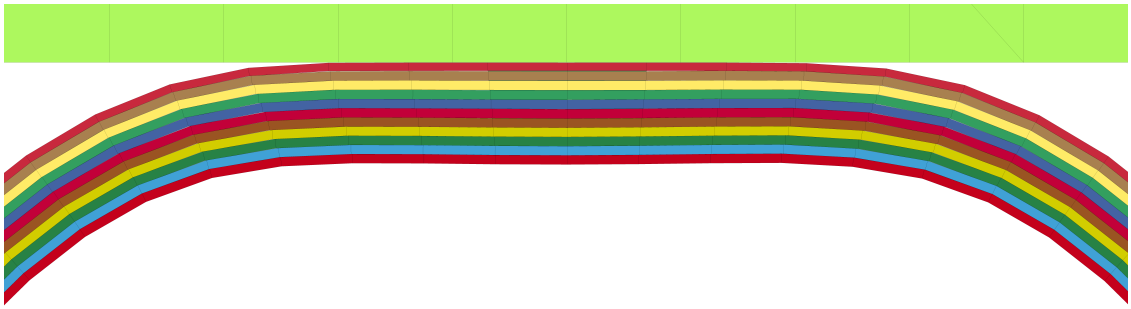

Figure F.4: Cross section deformation (element type: tshell; combined layers: 8)

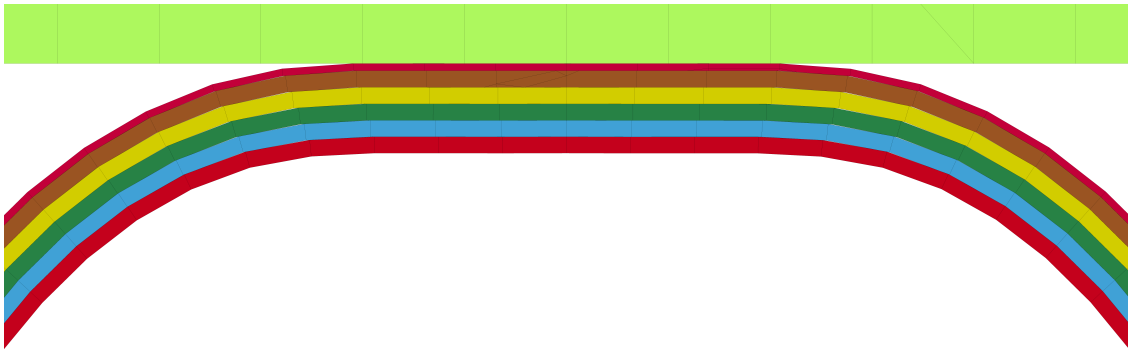

Figure F.5: Cross section deformation (element type: tshell; combined layers: 16)

Erklärung zur selbständigen Bearbeitung einer Abschlussarbeit

Gemäß der Allgemeinen Prüfungs- und Studienordnung ist zusammen mit der Abschlussarbeit eine schriftliche Erklärung abzugeben, in der der Studierende bestätigt, dass die Abschlussarbeit „–- bei einer Gruppenarbeit die entsprechend gekennzeichneten Teile der Arbeit [(§ 18 Abs. 1 APSO-TI-BM bzw. § 21 Abs. 1 APSO-INGI)] –- ohne fremde Hilfe selbständig verfasst und nur die angegebenen Quellen und Hilfsmittel benutzt wurden. Wörtlich oder dem Sinn nach aus anderen Werken entnommene Stellen sind unter Angabe der Quellen kenntlich zu machen."

Quelle: § 16 Abs. 5 APSO-TI-BM bzw. § 15 Abs. 6 APSO-INGI

Dieses Blatt, mit der folgenden Erklärung, ist nach Fertigstellung der Abschlussarbeit durch den Studierenden auszufüllen und jeweils mit Originalunterschrift als letztes Blatt in das Prüfungsexemplar der Abschlussarbeit einzubinden.
Eine unrichtig abgegebene Erklärung kann -auch nachträglich- zur Ungültigkeit des Studienabschlusses führen.

Erklärung zur selbständigen Bearbeitung der Arbeit

Hiermit versichere ich,

Name: _____

Vorname: _____

dass ich die vorliegende Masterarbeit – bzw. bei einer Gruppenarbeit die entsprechend gekennzeichneten Teile der Arbeit – mit dem Thema:

Entwicklung einer Finite-Element Simulationsmethodik für die Berechnung von dickwandigen Wasserstofftanks

ohne fremde Hilfe selbständig verfasst und nur die angegebenen Quellen und Hilfsmittel benutzt habe. Wörtlich oder dem Sinn nach aus anderen Werken entnommene Stellen sind unter Angabe der Quellen kenntlich gemacht.

- die folgende Aussage ist bei Gruppenarbeiten auszufüllen und entfällt bei Einzelarbeiten -

Die Kennzeichnung der von mir erstellten und verantworteten Teile der Masterarbeit ist erfolgt durch:

_____	_____	_____
Ort	Datum	Unterschrift im Original